POLITECNICO DI MILANO
Dipartimento di Elettronica, Informazione e Bioingegneria

and

TECHNISCHE UNIVERSITÄT MÜNCHEN
Department of Electrical and Computer Engineering

Master's Thesis

Setup of a Kerr microscope for the investigation and characterization of magnetic specimens

---

Academic Year:	2019/2020
Author:	Morshed Mohammed
Student ID:	892341
Italian Supervisor:	Prof. Giorgio Ferrari
German Supervisor:	Prof. Dr.-Ing. habil. Markus Becherer
Assistant Supervisor:	Valentin Ahrens

Acknowledgments

I would like to express my sincere appreciation to those people who contributed to this thesis and supported me during this amazing journey. Without them this project would not have been possible.

First and foremost, I would like to thank my thesis supervisors, Prof. Giorgio Ferrari and Prof. Dr.-Ing. habil. Markus Becherer, for supporting me from the very start of the project, for allowing me to write my thesis on a topic that is of great interest to me and for meeting my wish to work in the European context, providing me the opportunity to collaborate with the Technical University of Munich.

I would like to express my gratitude also to the assistant-supervisor Valentin Ahrens, as well as to Simon Mendisch and Luca Gnoli whose help, comments, advices and encouragement played a very determinant role for the success of this project.

Finally, a sincere thanks is addressed to all people who have been walking with me through this journey. Despite all my efforts, I could not have reached this result without the support of my family and friends. I am particularly grateful to Esther and to my friends Angelo, Beppe, Marco, Luca and Renato.

A very special thanks is reserved to my family for always supporting my studies and believing in me.

Abstract

Magnetic domain imaging of magnetic materials and nanostructures plays a fundamental role in the study of micromagnetic phenomena. Among the different instruments for the study of magnetic domains, the magneto-optical Kerr microscope presents the advantage of allowing the study of thin-film multilayer structures addressing the different magnetic layers. The magneto-optical Kerr microscope is an extension of a polarization contrast microscope and is based on the magneto-optical Kerr effect (MOKE). There are two different types of magneto-optical Kerr microscopes: wide-field MOKE microscope and laser-scanning MOKE microscope. The wide-field MOKE microscope illuminates the specimen evenly allowing the visualization of a large area. Whereas, the laser-scanning MOKE microscope employs a pulsed laser beam allowing to study the characteristics of the specimen locally. This master thesis consists in the design, implementation and characterization of a wide-field MOKE microscope. Moreover, the outcome of the project will represent a basis for the future implementation of a laser-scanning MOKE microscope. The following steps were undertaken during the process: first, a Zeiss-AXIOMAT was set up as a wide-field MOKE microscope through the improvement of the light source and the addition of a CCD camera. Second, better objectives control was obtained through a positioning system with graphical user interface. For achieving this purpose, the DC motor was substituted with a stepper motor and a driver, a magnetic encoder and a touch screen were added. Third, the improvement of the microscope performance and magnetic domains imaging were verified through the comparison of the initial magnetic domain images obtained by the Zeiss-AXIOMAT prior the configuration and the magnetic domain images obtained after the configuration as wide-field MOKE microscope. The images obtained after the configuration presented magnetic domains with a better defined shape and better contrast in comparison with the initial images. Alongside the activities conducted in each phase of the project, the laser-scanning MOKE microscope as well as its future implementation were also considered.

Sommario

La visualizzazione dei domini magnetici ha un ruolo fondamentale nello studio dei fenomeni micromagnetici. Tra i diversi strumenti per lo studio di questi fenomeni, il microscopio Kerr presenta il vantaggio di permettere la visualizzazione di strutture multistrato focalizzandosi sui diversi strati magnetici. Il microscopio Kerr è un'estensione del microscopio in luce polarizzazata e si basa sull'effetto Kerr magneto-ottico (MOKE). Ci sono due diversi tipi di microscopi Kerr: microscopio MOKE a campo largo e a scansione laser. Il microscopio MOKE a campo largo illumina i campioni in modo omogeneo permettendo la visualizzazione di una vasta area. Invece, il microscopio MOKE a scansione laser impiega un raggio laser che permette di studiare le caratteristiche del campione localmente. Questa tesi riguarda la progettazione, implementazione e caratterizzazione di un microscopio MOKE a campo largo. Inoltre, i risultati del progetto permetteranno anche la futura implementazione di un microscopio MOKE a scansione laser. La tesi si è svolta come segue. In primo luogo, un microscopio Zeiss-AXIOMAT è stato configurato come microscopio MOKE a campo largo migliorando la sorgente luminosa e aggiungendo una CCD camera. In secondo luogo, un migliore controllo degli obiettivi è stato ottenuto attraverso un sistema di posizionamento con interfaccia grafica. Per raggiungere questo scopo, il motore DC è stato sostituito con un motore passo a passo e il suo controllore. Quindi, sono stati aggiunti un codificatore magnetico e uno schermo touch. Infine, è stato verificato il miglioramento delle prestazioni del microscopio e la visualizzazione dei domini magnetici attraverso il confronto delle immagini iniziali dei domini magnetici, ottenute dallo Zeiss-AXIOMAT prima della configurazione, e delle immagini finali, ottenute dopo la sua configurazione come microscopio MOKE a campo largo. Le immagini finali hanno presentato dei domini magnetici con una forma ben definita e un miglior contrasto rispetto alle immagini iniziali. Durante le attività condotte in ciascuna fase del progetto, è stato considerato anche il microscopio MOKE a scansione laser e la sua futura implementazione.

Contents

Acknowledgments **ii**

Abstract **iii**

Sommario **iv**

List of Figures **vii**

1 Introduction **1**

2 Theoretical background **4**

2.1 Basic Concepts in Microscopy 4

2.1.1 Lenses and geometrical optics 6

2.1.2 Objectives and resolution 14

2.1.3 Köhler illumination 17

2.2 Magneto-optical Microscopy 23

2.2.1 Polarization state of light 24

2.2.2 Magneto-optical Kerr effect (MOKE) 27

3 Design, Implementation and Characterization **31**

3.1 Magneto-optical Kerr Microscope 31

3.2 Kerr Microscope Development 34

3.2.1 Improvement of the light source 34

3.2.2 Addition of a camera system to visualize domain images 49

3.2.3 Adjustment of optical system 53

3.2.4 Obtainment of better objectives control through a positioning system . 60

3.3 Key Support Activities 97

4 Progress Evaluation after Wide-field MOKE Microscope Setup **102**

5 Conclusion and Final Considerations **110**

Appendix **113**

Bibliography **118**

List of Figures

1.1 New parts added to Zeiss-AXIOMAT for its setup as Kerr microscope 2

2.1 Generic scheme of a reflected light microscope 5
2.2 Simple lenses 7
2.3 Thick lens and primary lenses geometry 9
2.4 Image formation - thin lens 11
2.5 Ray diagram for different positions of object 12
2.6 Oblique parallel rays converging in a point on the focal plane 12
2.7 Optical aberrations 13
2.8 Rayleigh Criterion for the resolution of a diffraction limited system 15
2.9 Numerical aperture and depth of field of a lens 16
2.10 Representation of images of a non-point like object 17
2.11 The optics of a microscope divided into two groups 18
2.12 Even and uneven illumination of the specimen 19
2.13 Two sets of conjugate focal planes 20
2.14 Conjugate image and illumination planes 21
2.15 Optical Path of a reflected light microscope 22
2.16 Different types of polarization 25
2.17 Three geometries of the magneto-optical Kerr effect 28
2.18 Polar magneto-optical Kerr effect 29
2.19 Superposition of two circularly polarized waves 30

3.1 Representation of a Kerr microscope 32
3.2 Representation of a laser-scanning MOKE microscope 33
3.3 Substitution of the halogen lamp 35
3.4 Optical paths inside the observation module 36
3.5 Substitution of the lamp house 39

3.6 Trade-off between light size and light intensity . . . 41
3.7 Source magnification caused by two lenses . . . 42
3.8 Lens configuration 2 . . . 43
3.9 Lens configuration 3 . . . 43
3.10 Lens configuration 4 . . . 44
3.11 New lens system to focus a light image at the aperture plane . . . 45
3.12 Efficiency of light projection is dependent on the LEDs etendue . . . 47
3.13 An illustration of the basic optical invariant . . . 47
3.14 MOS capacitor . . . 49
3.15 Quantum efficiency curves of the pco.pixelfly . . . 50
3.16 Zeiss-AXIOMAT after addition of a CCD camera . . . 52
3.17 Reflection of a s polarized wave . . . 54
3.18 Analyzer at a small angle from extinction . . . 55
3.19 Change of Kerr intensity . . . 57
3.20 Representation of the cross-shaped extinction pattern . . . 58
3.21 Adjustment of optical components of Zeiss-AXIOMAT . . . 59
3.22 Zeiss-AXIOMAT with positioning system and graphical user interface (GUI) . 61
3.23 Graphical user interface (GUI) of the positioning system . . . 62
3.24 Arduino Mega connection with the display shield . . . 63
3.25 Display shield pin modification . . . 64
3.26 Representation of a brushed DC motor . . . 66
3.27 DC motor torque-speed curve . . . 68
3.28 Bidirection BDC motor Drive (H-bridge) circuit . . . 68
3.29 Different types of stepper motors . . . 70
3.30 Different type of windings . . . 71
3.31 Torque vs. speed characteristics of a stepper motor . . . 71
3.32 Stepper motor and driver added to the system . . . 75
3.33 SY28STH45-0674A Pull-out torque curve . . . 77
3.34 Signal period when the motor is rotating at maximum speed . . . 80
3.35 Limit switches inside the microscope . . . 83
3.36 Limit switches connection . . . 83
3.37 Addition of the encoder . . . 84
3.38 Encoder fixed on the metal piece . . . 85

3.39 RLM2SJ - SSI - Timing diagram . . . 86
3.40 Simple SSI block diagram . . . 87
3.41 SSI timing diagram . . . 88
3.42 Simple SPI block diagram . . . 88
3.43 Bytes read by Arduino . . . 90
3.44 SPI as SSI - Timing diagram . . . 91
3.45 Encoder timeout verification . . . 92
3.46 Encoder timeout verification with Arduino . . . 93
3.47 Encoder position inside microscope and its displacement . . . 93
3.48 Photodiode amplifier . . . 98
3.49 Typical photodiode transfer function. . . . 99
3.50 Transimpedence amplifier output . . . 100

4.1 Domain image 1 with 25x . . . 103
4.2 Domain image 2 with 25x . . . 104
4.3 Domain Image 3 with 25x and Image 4 with 50x . . . 105
4.4 Domain image 5 with 25x . . . 106
4.5 Domain image 6 and image 7 with zoom OPTOVAR with 25x . . . 107
4.6 Domain image 8 with 25x and image 9 with 50x . . . 108
4.7 Domain image 10 with 25x and image 11 with 50x . . . 108
4.8 Pixel size in the image . . . 109

A.1 Arduino display shield . . . 113
A.2 Photodetector . . . 113
A.3 Illuminating system . . . 114
A.4 Encoder housing and left limit switch . . . 114
A.5 Stepper motor . . . 115
A.6 Components inside the housing . . . 115
A.7 Touch screen inside the component housing . . . 116
A.8 Components housing - Front side and and external buttons . . . 116
A.9 Components housing - Lateral side . . . 117
A.10 CCD camera . . . 117

1 Introduction

Magnetic domain imaging is a well acknowledged technique for the study of magnetic materials and nanostructures [1]. The investigation of magnetic domains, which represent uniformly magnetized regions of ferromagnetic materials [2], is fundamental to understand the physical properties of thin-film multilayer structures. Several instruments have been developed for this purpose. Among those, the magneto-optical Kerr microscope is an extension of a polarization contrast microscope and has become an important measuring instrument in the field of magnetism and spintronics. In particular, it is based on the magneto-optical Kerr effect (MOKE) and employed to study the magnetic micro and nanostructures of ferromagnetic specimens through magnetic domains imaging. There are two different types of magneto-optical microscopes based on the magneto-optical Kerr effect (MOKE): The laser-scanning MOKE microscope (LMOKE) and wide-field MOKE microscope (WMOKE). The wide-field Kerr microscope employs a LED to illuminate a wide area of the specimen and a camera for domain image recording. Whereas, The laser-scanning Kerr microscope employs a pulsed laser beam to scan the specimen surface to form an image or to focus on a tiny spot on the specimen allowing the hysteresis measurement by sweeping the magnetic field and looking at the intensity in the region of interest.

This master thesis was conducted at the chair of Nano and Quantum Sensors (Technical University of Munich) and consists in the design, implementation and characterization of a magneto-optical Kerr microscope, which will be used for the inspection of magnetic domains of thin-film multilayer structures for the development of magnetic storage devices. The final aim of this project is to adapt a Zeiss-AXIOMAT as both wide-field MOKE and Laser-scanning MOKE. The main activities conducted are reported below (Fig. 1.1):

Improvement of the light source: For the wide-field MOKE, the original halogen lamp was substituted with a high-power 100 W LED matrix as a light source. After that, Köhler illumination was employed to collimate the light coming from the light source to evenly

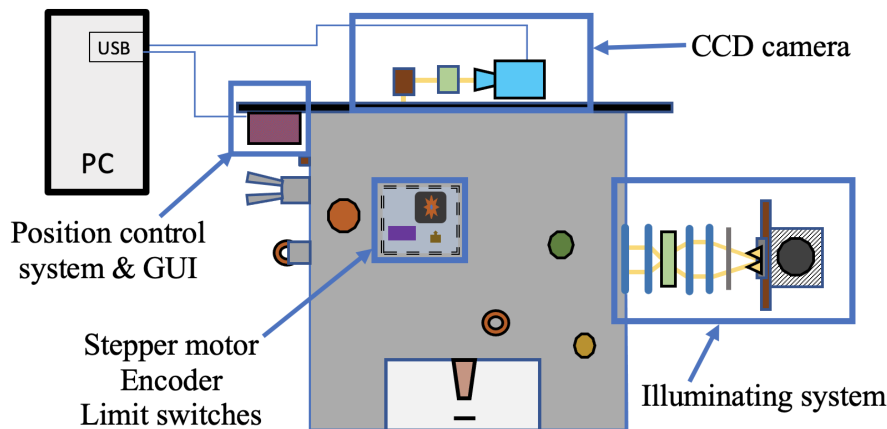

Figure 1.1: New parts added to Zeiss-AXIOMAT for its setup as Kerr microscope: illuminating system, position control system and graphical user interface (GUI) and CCD camera.

illuminate the specimen. Köhler illumination is a method to align the optics in such a way that the light source is fully defocused onto the specimen providing an optimum illumination and magneto-optical contrast across the whole viewing field [2, 3].

Obtainment of better objectives control through a positioning system: the DC motor in the Zeiss-AXIOMAT was substituted with a stepper motor and a driver. This solution allowed to move the objectives accurately. The movement of the objectives was controlled via a graphical user interface thanks to the employment of a touchscreen. A magnetic encoder was also added to the microscope to track precisely the position of the objectives. Moreover, a microcontroller was employed to control all these electronic components during the implementation of the positioning system.

Addition of a CCD camera for the wide-field MOKE: a CCD camera to study the magnetic microstructures of ferromagnetic specimens through magnetic domain imaging was added. The imaging was performed with MATLAB and the software provided by the CCD camera manufacturer.

Beside these main activities, some key support activities were conducted. Among those: the design and print of a housing to host all the electronic components needed to control the system; and the optimization of a photodiode amplifier to measure the light intensity of the LED matrix.

Finally, the initial domain images obtained by the Zeiss-AXIOMAT were compared with the domain images obtained after its configuration as wide-field MOKE to assess the improvement

of the performance of the microscope. The images obtained after the configuration presented domains with a well-defined shape and better contrast in comparison with the initial images.

Given the limited duration of this project, only the wide-field MOKE was set up. But all studies have been performed taking into account also the Laser MOKE. Therefore, the outcomes of this master thesis will allow its future implementation as well.

In the next sections, all the above-mentioned activities will be explained in greater detail. First, an overview of the basic concepts in optical microscopy will be provided. Second, Köhler illumination and magneto-optical Kerr effect will be introduced. Third, the design, implementation and characterization of the magneto-optical Kerr microscope will be bescribed as well as the development of the hardware and software for the objectives positioning system. Finally, the results obtained after the setup of the Zeiss-AXIOMAT as a Kerr microscope will be provided.

2 Theoretical background

2.1 Basic Concepts in Microscopy

Light microscopy is employed for studying microstructures though different instruments. For example, the transmitted light microscope employs transmitted illumination and is common in the micro-structural imaging of polymers. Whereas, the reflected light microscope employs vertical illumination and is generally used in the imaging of metallic specimens. Many microscope manufacturers provide models allowing to alternate inspections using vertical and transmitted illumination.

The final aim of this thesis is to design, implement and characterize a magneto-optical Kerr microscope. The basic operations of a Kerr microscope is equivalent to those of an ordinary reflected light microscope. Therefore, this section introduces the main principles of reflected light microscopy as well as reflected light microscopes, providing an overview of lenses and geometrical optics, objectives and resolution as well as Köhler illumination. These concepts will be useful for the understanding of the setup of a Zeiss-AXIOMAT as a wide-field Kerr microscope.

Reflected light microscopy

Reflected light microscopy is the preferred method for imaging opaque specimens, even when ground to a thickness of 30 μm. It allows the study of many types of specimens, including most metals, ceramics, many polymers, semiconductors, and various specialized materials [4]. Since the light can not pass through these specimens, in reflected microscopy the specimen is illuminated from above through the objective and the light is returned back to the microscope objective by specular or diffused reflection (Fig. 2.1). This type of illumination is often referred to as epi-illumination or vertical illumination compared to transmitted illumination where light passes through the specimen.

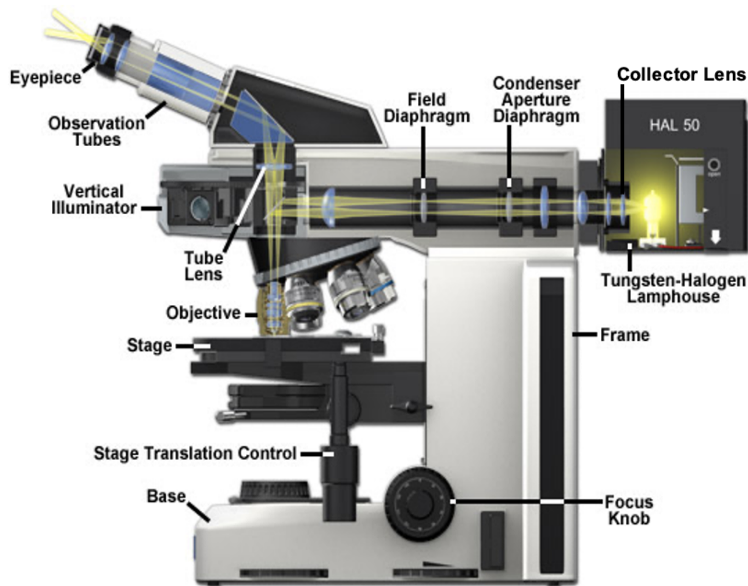

Figure 2.1: Generic scheme of a reflected light microscope (adapted from [3]).

A reflected light microscope is an instrument designed to produce a magnified image of a specimen by passing light from the illuminator through a series of lenses and then focusing this light either into the eyepieces or onto a digital image sensor. The magnification is achieved by the optical train, which typically consists in light source, collector lens, condenser aperture diaphragm, field diaphragm, objective, specimen and detector. In a reflected light microscope, the optical pathway starts with illuminating light originating in the lamp house. This light passes through the collector lens and then into the vertical illuminator where it is controlled by the aperture and field diaphragms. The light is then reflected by a beamsplitter through the objective to illuminate the specimen. The light reflected from the specimen surface re-enters the objective, then goes into the binocular head where it is directed either to the eyepieces or to a digital camera [4]. Additionally, a reflected light microscope could include light condition devices along the light path, such as a polarizer and an analyzer, whose purpose is to change the type of image contrast. The image contrast is function of spatial frequency, phase, polarization, absorption, fluorescence, and/or other properties of the specimen and the illumination technique.

2.1.1 Lenses and geometrical optics

The main optical components in a reflected light microscope are diaphragms and lenses. Through the aperture and closure of the diaphragms, it is possible to ponderate the quantity of light that pass through the optical system. Whereas, the lenses are used to form images by focusing the light coming from the diaphragms. Usually, the lenses have a circular shape with two primary surfaces producing either light convergence or divergence. These two primary surfaces can be either convex or concave [5] and determine the type of light propagation. Light propagation can be studied through geometrical optics, which is a branch of optics dealing with phenomena such as reflection, refraction, polarization, etc. and describing light in terms of rays. A ray of light gives the direction of propagation of light. In the absence of obstacles, a light ray propagates in a straight line without changing its direction. Whereas, when it encounters the lens surface, the light rays bend and reflection and refraction occur. In the following, the behavior of light rays with thin and thick lenses will be introduced.

Thin lens

A lens is characterized by two diopters, which are the surfaces through which the transmission of light from one medium to another takes place. These surfaces can be plane, spherical, convergent or divergent. Given two diopters with radius of curvatures R_1 and R_2 and having the same optical axis[1], three distinct regions with their own refraction index can be defined (Fig. 2.2a) [6]. The Light coming from left side propagates inside the first medium with refractive index n_1, it is then transmitted inside the second medium with refractive index n_2 and then it continues propagating inside the third medium having refractive index n_3. The block of transparent material having n_2 and bounded by the two diopters, with radii of curvature R_1 and R_2, is called a simple lens. If the distance d along the optical axis between the two diopters of the lens is negligible compared to their radii of curvature R_1 and R_2 (i.e., $d \ll |R_1|$ and d $\ll |R_2|$ (Fig. 2.2a)) then this simple lens is called thin lens.

Assuming $n_1 = n_3$ and $d = 0$ (i.e., the vertices of the surfaces coincide with each other and with the center of the lens), under the paraxial approximation[2], the thin lens equation is

[1] The optical axis is an imaginary straight line which passes through the geometrical center of the lens and joins the two centers of curvature of its surfaces.

[2] In the paraxial approximation, it is assumed that all rays, throughout the lens, make small angle ($\sin\theta \approx \theta$) to the optical axis and lie also close to it.

obtained [6]:

$$\frac{1}{p} + \frac{1}{q} = \frac{1}{f} \tag{2.1}$$

where f is the focal length:

$$f = \frac{n_1}{n_2 - n_1} \frac{R_1 R_2}{R_2 - R_1} \tag{2.2}$$

and p and q are distances of the object and of its image from the center of the lens. Moreover, the following arbitrary sign conventions are used:

1. R_1 is positive since the first surface is convex (it is negative if the first surface is concave). The signs are opposite for the back surface of the lens, i.e. R_2 is positive if the surface is concave, and is negative if it is convex.
2. Given an object, its distance p from the vertex of a surface is positive if the object is on the left side of the vertex, otherwise it is negative.
3. Given an image, its distance q from the vertex of a surface is positive if the image is on the right side of the vertex, otherwise it is negative.
4. Heights above the optic axis are positive.

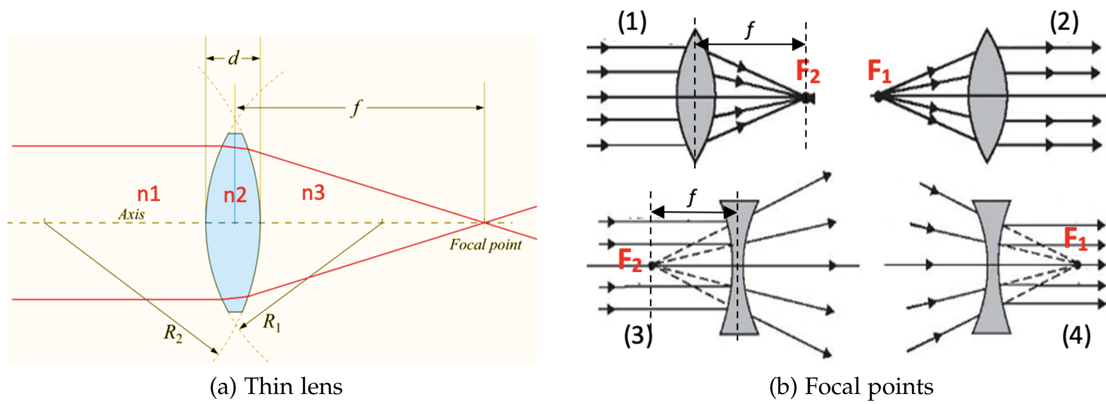

(a) Thin lens (b) Focal points

Figure 2.2: Simple lenses (Adapted from [7][8]).

The planes perpendicular to the optical axis at p and q are called object plane and image plane respectively. If an object is at infinity ($p = \infty$), then its image is formed at the point F_2, at a distance f_1 from the lens center (q = f_1) (Fig. 2.2b.1), while if the object is at the point F_1, at a distance f_2, then its image is formed at infinity (Fig. 2.2b.2).

The distances f_1 and f_2 from the center of the lens where rays of light coming from infinity converged is called focal distance. The points F_1 and F_2 are at the same distance from the

center of the lens and they are the two focal lengths ($f_1 = f_2 = f$) of the thin lens [6]. Depending on the sign and the value of the R_1 and R_2 and on the sign of the refractive indices, $\frac{1}{f}$ can be positive or negative.

If $\frac{1}{f}$ is positive, then the lens is called converging lens or positive lens (Fig. 2.2b.1 and Fig. 2.2b.2) otherwise it is called diverging lens or negative lens (Fig. 2.2b.3 and Fig. 2.2b.4). Positive lenses have one or two convex surfaces and are thicker in the center than at the edges. Negative lenses have at least one concave surface and are thinner in the center than at the edges. Positive lenses converge incident light rays that are parallel to the optical axis and focus them at the focal point to form a real image. Negative lenses diverge parallel incident light rays and form a virtual image by extending traces of the light rays passing through the lens to a focal point behind the lens (Fig. 2.2b).

Normally, images are defined by the regions where light rays (and their extensions) converge as the result of refraction by a lens. In cases where the light rays intersect at a focal point, the image is real and it can be projected on a screen or onto the surface of a sensor such as a CCD or CMOS placed in the image plane. When the light rays diverge, but project imaginary extensions that converge to a focal point, the image is virtual and can not be viewed on a screen (Fig. 2.4b) [9].

The primary lens geometries depend on the shape of the lens [6]. There are positive lens elements i.e., bi-convex (Fig. 2.3b.a), plano-convex (Fig. 2.3bb), convex-meniscus (Fig. 2.3bc) and negative lens elements i.e., bi-concave (Fig. 2.3bd), plano-concave (Fig. 2.3be) and concave-meniscus(Fig. 2.3bf). The lenses in the microscope mostly behave like simple convex lenses [9].

Thick Lens

The simple lens in Figure 2.2a is called thick lens when the distance d between the two diopters is not negligible compare to their radii of curvature R_1 and R_2. For this type of lens the two focal distances (f_1 and f_2) are defined from two particular points P_1 and P_2 (Fig. 2.3a).

Given an object at infinity, its image is formed at a point F_2, at a distance of q_0 from the second diopter. When the object is in F_1, at a distance p_0 from the first diopter, then its image is formed at infinity (Fig. 2.3a). In the case of the thick lens the values p_0 and q_0 are different. However, they are same if $d = 0$ or the lens is symmetric i.e., $R_2 = -R_1$. The distance $f = f_1 = f_2 = \overline{P_1F_1} = \overline{P_2F_2}$, is called focal length of the thick lens [6].

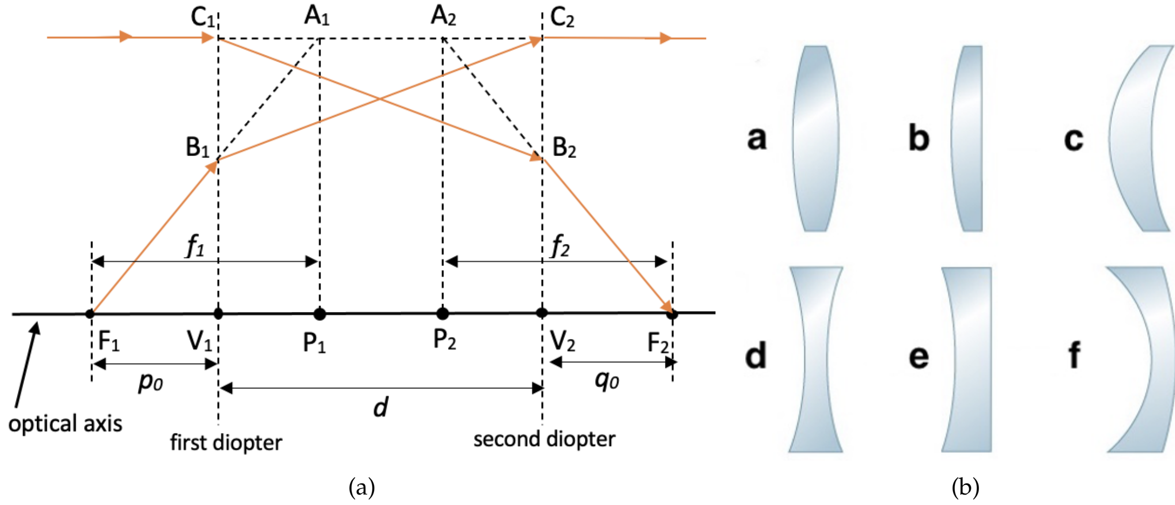

Figure 2.3: (a) Thick lens representation (adapted from [6]). (b)Primary lens lens geometries (adapted from [10]).

P_1 and P_2 are called principle points and they are founds by the intersection of the optical axis and the principal planes. The principal planes are two hypothetical planes at which all the refraction can be considered to occur and not on the diopters [6].

In Figure 2.3a, the ray coming from the left before ending in the focal point F_2 is subjected to two refractions in two points: C_1 and B_2. C_1 is contained in the plane perpendicular to the optical axis and tangent to the vertex V_1 of the first diopter. B_2 is contained in the plane perpendicular to the optical axis and tangent to the second diopter vertex V_2. Instead of the ray with two refractions, it is possible to consider an another fictitious ray refracted only once at the principal plane: the ray passing through the points C_1, A_2 and B_2 before ending in F_2. A_1 and A_2 belongs to the first and second principal planes of the lens respectively. The principal planes may be located in any order and not necessarily inside the lens itself.

The focal points (f_1, f_2) of the thick lens do not have the same distance from the vertex. Nevertheless, the distance would be equal if the focal points were considered from the principal planes. The equation for the thick lens is (under the paraxial aproximation) [6]:

$$\frac{1}{p} + \frac{1}{q} = \frac{1}{f} \tag{2.3}$$

where

$$f = \frac{n_2 - n_1}{n_1 n_2} \frac{R_1 R_2}{(n_2 - n_1)d + n_2(R_2 - R_1)}, \tag{2.4}$$

p is the distance of the object from the first principal plane and q is the distance of the image

from the second principal plane.

For a thick lens, the focal length f is often called effective focal length (EFL), to distinguish it from other used parameters[11]:

1. Front focal length (FFL) which is the distance p_0 from the vertex V_1 of the first diopter to the front focal point (F_1) (Fig. 2.3a).
2. Back focal length (BFL) which is the distance q_0 from the vertex V_2 of the second diopter to the rear focal point (F_2) (Fig. 2.3a).

In a thin lens, the two principal planes coincide between them and with the plane where the lens is placed.

Geometrical construction of the ray diagrams

To determine size and location of images formed by a lens, it is possible to trace the paths taken by the light rays coming from an object. The size and location of the images formed depend on the type of lens, in particular converging or diverging. In the following,the rules for a converging and a diverging lens will be introduced considering a thin lens and an object of height h_1 placed in a position p_0 on the optical axis. An ideal thin lens is used and the refractions is considered to happen on the plane where the lens is situated. Moreover, the image represents only one point of the object.

Converging lens (Fig. 2.4a):

1. First, we consider an incident ray (Ray 1) parallel to the optical axis entering the converging lens and then passing through the focal point F_2.
2. Second, a ray (Ray 2) passing through the center of the lens without being refracted.
3. Third, a ray (Ray 3) that passes through the focal point F1 and exits the lens parallel to the optical axis.

Diverging lens (Fig. 2.4b):

1. We consider an incident ray (Ray 1) entering the lens parallel to the optical axis and exiting as if it came from the focal point F_1.
2. A ray which passes through the center of the lens without being deviated (Ray 2).
3. Third, we consider a ray which is directed toward the focal point F_2 but it exists the lens parallel to the optical axis (Ray 3).

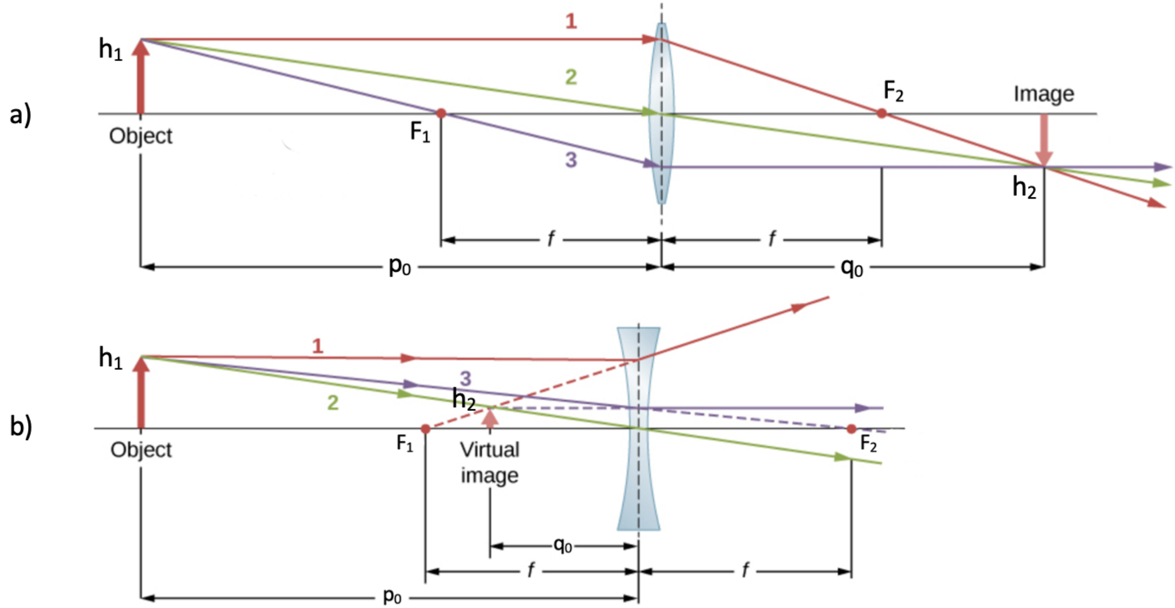

Figure 2.4: (a) Convergence lens, (b) Divergence lens (adapted from [10]).

These three rays in converging lens (Fig. 2.4a) and diverging lens (Fig. 2.4b)cross at a single point and the image of the tip of the arrow is located at that point. All other rays coming from the same point of the arrow enter the lens and cross at the same point after the refraction. Doing the same with every point of the object we can build the the rest of the image.

The basic concepts derived from geometrical optics and the ray diagrams above allow an understanding of the magnification process [5]. There are two type of magnification between the object and the image: transverse magnification (M_T) and longitudinal magnification (M_L). M_T is the ratio of the image size to the object size and M_L is the ratio of the distances between two image points along the optic axis to their corresponding conjugate points in the object [6]:

$$M_T = \frac{h_2}{h_1} = \frac{q_0}{p_0} \tag{2.5}$$

$$M_L = \frac{q_2 - q_1}{p_2 - p_1} = M_{T1} M_{T2} \tag{2.6}$$

M_{T1} and M_{T2} are the transverse magnification for two points inside the object: p_1 and p_2 respectively. In general, the magnitude of the longitudinal magnification is determined by the square of the transverse magnification for small distances within the image plane since for small distance $M_{T1} \approx M_{T2}$ [6]. When all these features are calculated mathematically, it is

important to pay attention to the sign convention adopted. Figure 2.5 shows different ray

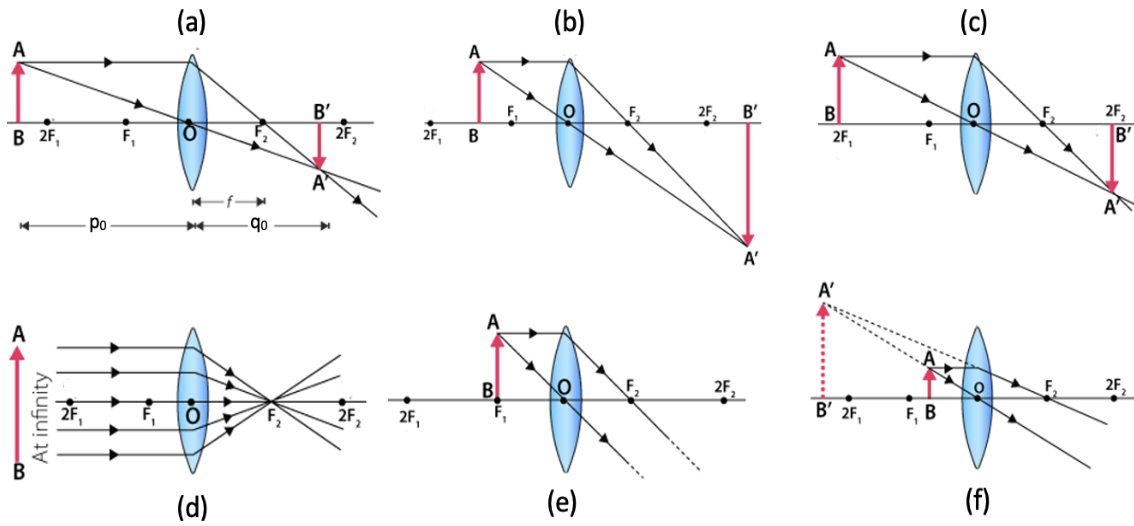

Figure 2.5: Ray diagram for different positions of object (adapted from [12]).

diagram for different positions of object given a thin convex lens. The construction of the image in a thick lens follows almost the same process. The only difference is that the rays coming from left and right are refracted in two distinct planes: the two principal planes of the lens (see Section 2.1.1). The distance between them depends on the thickness of the lens.

As reported above, the rays coming from the left parallel to the optical axis end up in the focal point F_2 of the converging lens. Whereas, for the diverging lens these rays propagate from the lens in a direction such that they appear to be coming from the focal point F_1 (Fig. 2.4). In the case these parallel rays are not parallel to the optical axis, then they end up in

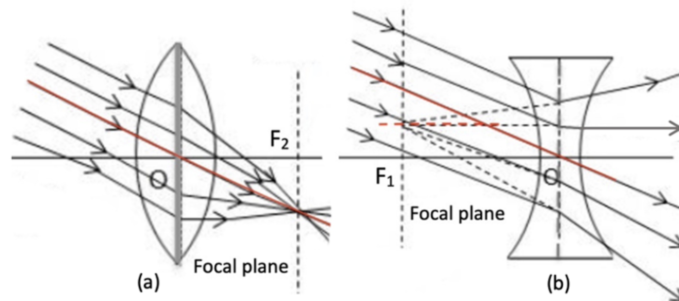

Figure 2.6: Oblique parallel rays converge in a point different from the focal point of the lens (adapted from [13]).

a different point and not in the same point as before. For the converging and diverging lens, the image is formed in a point in the plane called the focal plane. The focal plane contains

the focal point and it is perpendicular to the optical axis. As shown in Figure 2.6, the image is formed in the point where the parallel ray through the center of the lens crosses the focal plane.

Optical aberrations

As stated before, the equations 2.1 and 2.4 of the lenses are valid only in a paraxial approximation i.e., $\sin\theta$ can be approximated with its argument θ. This approximation is assumed to be valid also when the images of an object are built through the lens in Figure 2.4. Nevertheless, when the rays make a big angle to the optical axis or are far from the axis (no matter their angle), or when the light source is non-monochromatic (even if the paraxial approximation is valid), the images obtained differ from the ones found with the paraxial theory.

Therefore, only in an ideal case it is possible to find images via mathematical calculations or to use the technique of Figure 2.4. Real images differ from ideal images because of a phenomenon called aberration [6]. There are two type of aberrations: monochromatic and chromatic.

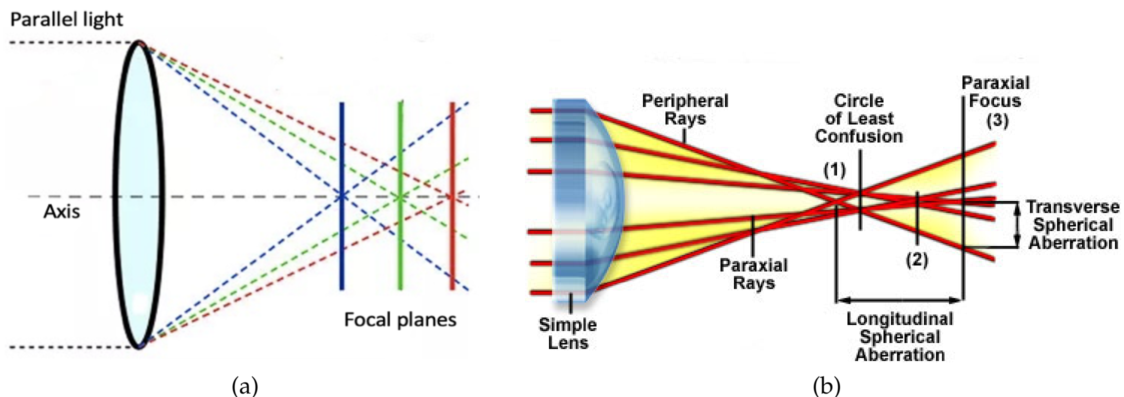

Figure 2.7: (a) Longitudinal chromatic aberration. (b) Spherical aberration Optical aberrations(adapted from [14, 4]).

Chromatic aberration is related to the wavelength of the light that passes through a lens. The refractive index n, depends on the wavelength and therefore the lens characteristics that depend on n also vary i.e., the focal length, the image distance and the image magnification [6].

When a white light passes through a lens, the colors components are refracted in different directions according to their wavelength. Figure 2.7a shows a longitudinal chromatic aberration (LCA), which occurs when the light components focus at different points along the optical axis due to their different wavelengths.

Monochromatic aberrations are caused by the geometry of the lens. There are more types of monochromatic aberrations than chromatic aberrations. Among the various monochromatic aberrations, spherical aberration is due to the spherical shape of the lens surfaces. Light rays passing through the off-centre of a spherical surface are refracted differently than the rays passing through the center of the lens. This effect occurs both horizontally and vertically. Parallel light passing through the lens will be focused in different points, producing a variety of different focal points along the optical axis. This is known as longitudinal spherical aberration and it is the distance between the focus points of the peripheral ray (focal point (1) in the figure 2.7b) and the paraxial plane. The paraxial plane is perpendicular to the optical axis and contains the focus point given by the paraxial rays (Focal point (3) in the figure 2.7b). When the intersections of the rays with a plane perpendicular to the optical axis are considered, these intersections will be in a circular zone having a diameter that changes depending on where the plane is considered. There is a position along the optical axis where this circle has the minimum diameter and is therefore called circle of least confusion [6]. In this position, the best image of the object is formed.

There is also a transverse spherical aberration, defined as the distance from the optical axis at which the off-center ray intersect the plane of paraxial focus. These peripheral rays undergo greater refraction than central rays (see focal points (1), (2) and (3) in Figure 2.7b).

2.1.2 Objectives and resolution

Above, differnt typologies of lenses and geometrical optics have been introduced. In this section, some further basic concepts in microscopy will be presented. In particular, the objectives are the most important part of a reflected light microscope because they gather light from the specimen to provide magnified and real images. The objectives are complex multi-element assemblies playing a central role in determining image quality produced by the microscope. We can find objectives with magnifications ranging from 2X to 200X. In the reflected light system, the objectives serve a dual function: on the way down as a matching well-corrected condenser properly aligned and on the way up as an image-forming objective by projecting the image-carrying rays toward the eyepiece [15].

When light passes through the objectives, it interferes with itself, forming a circular diffraction pattern (called the Airy pattern (Fig. 2.8)), which means that each point in the specimen is displayed in the image as a small pattern instead of a point. The Airy disc

represents the final resolution achievable from an optical system, free from all the other non-ideal sources.

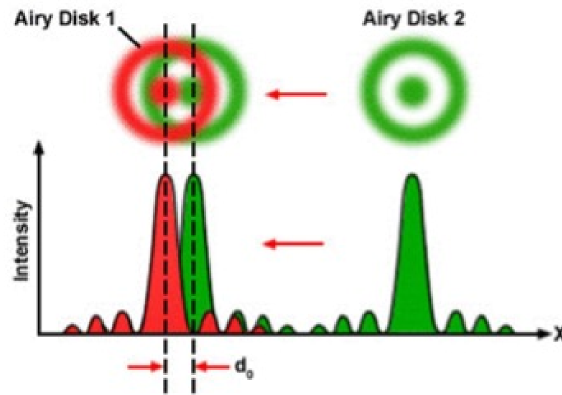

Figure 2.8: Rayleigh Criterion for the resolution of a diffraction limited system [16]. This limitation is the point where the two Airy patterns are no longer distinguishable from each other i.e., when Airy disk 2 is superimposed to Airy disk 1.

Each objective has an upper limit of performance specified by the laws of physics and the Airy disk, known as the diffraction limit. This limit is the theoretical maximum resolving power of the objective. This limitation is the point where the two Airy patterns are no longer distinguishable from each other (Airy disk 2 superimposed to Airy disk 1 as shown in Fig. 2.8). An ideal objective that is not limited by design will still be limited by diffraction.

Given the optical parameters and the average illumination light wavelength of the system, it is possible to derive a theoretically quantitative expression of the resolution from the size of the Airy pattern. The distance between the central peak and the first minimum of the Airy pattern can be calculated from [17]:

$$d = 0.61 \frac{\lambda}{NA} = \text{Resolution}. \tag{2.7}$$

Where λ is the average wavelength of the illumination light and NA is the numerical aperture of the objective lens. The numerical aperture NA is given by the product $n \cdot \sin(\theta)$, where n is the refractive index of the medium between the objective and the specimen (a value that ranges from 1.00 for air to 1.51 for specialized immersion oils) and θ is one-half angular aperture of the objective. The numerical aperture of the objective represents the angle of acceptance of the cone light of the objective. It is a measure of its ability to gather light and resolve fine specimen details at a fixed object distance.

The light rays forming the image reflected from the specimen enter the objective in an inverted cone shape. A longitudinal section of this light cone shows the angular aperture (A) as shown in Fig. 2.9a, which is determined by the focal length of the objective lens.

The higher the numerical aperture, the larger the angular aperture, which means that the number of oblique rays entering the front lens of the objective lens from a point on the surface is greater. Higher NA values make smaller structures more clearly visible.

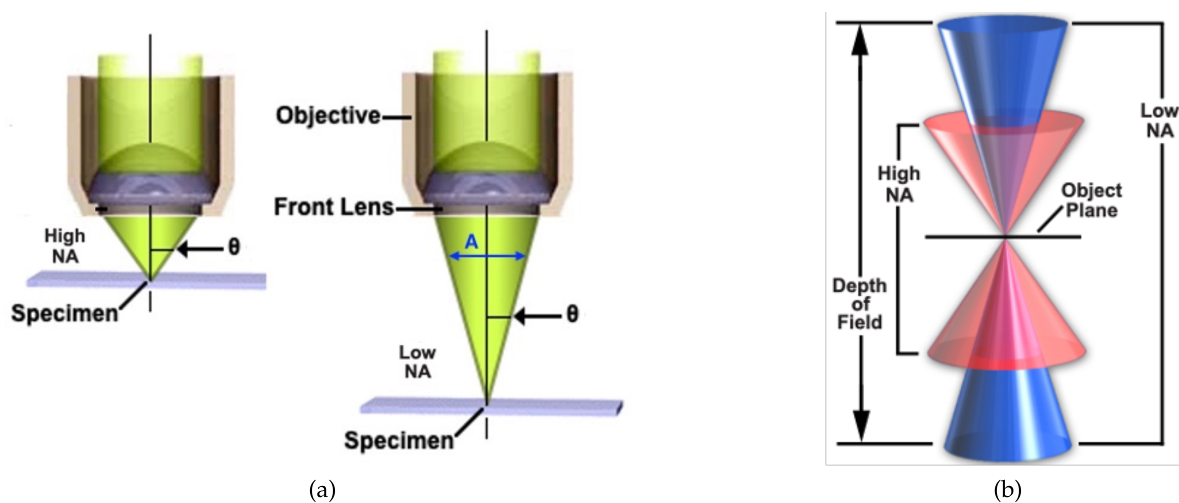

Figure 2.9: Numerical aperture light cones and depth of field ranges of a objective [18, 19].

In addition to this point-to-point lateral resolution in a plane perpendicular to the optical axis, it is important to consider also: depth of field and depth of focus. They define the axial (or longitudinal) resolving power of the objective lens and are measured parallel to the optical axis. Depth of field is the axial depth of the space on both sides of the object plane, in which the object can be moved without losing image clarity (Fig. 2.9b). It represents the ability of the objective lens to maintain the required image quality without refocusing (i.e., the position of the image plane is maintained), if the object position is moved from the plane of best focus. Depth of focus is the image-space complement of depth of field and is related to the change in the focus quality on the sensor side of the lens as the sensor is moved, while the object remains in the same position. In short, the depth of field is related to the image quality of the fixed lens when repositioning the object, while the depth of focus is related to the fixed object and the ability of the sensor to maintain the focus for different sensor positions (including tilting). High-magnification objectives (due to their larger aperture) have a very limited depth of field, but a relatively large depth of focus. Whereas low-magnification objectives (because

of their small aperture) have considerable depth of field, but low depth of focus [20].

2.1.3 Köhler illumination

Reflected light microscopes apply special illumination techniques to unveil details of microstructures such as dark-field illumination, polarized light microscopy, phase contrast microscopy. These techniques employ the principles of Köhler illumination, which was first introduced in 1893 by August Köhler as a method for providing the optimum specimen illumination. In microscopy, the illumination of the specimen plays an important role in achieving high-quality images. Köhler illumination is a method of aligning the optics in such a way that the light source is fully defocused onto the specimen providing an optimum illumination and a constant magneto-optical contrast across the whole viewing field [17, 15]. Aligning the optics means positioning optics elements relative to one another and relative to the specimen. In the following, it is explained how optics elements are employed in Köhler illumination. Most of the figures employed for the explanation of Köhler illumination are taken from [21].

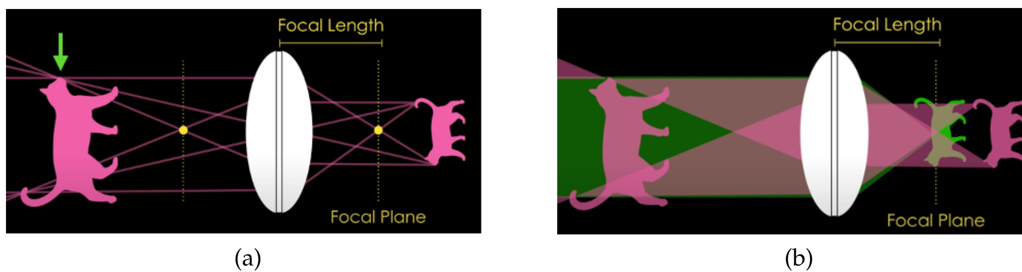

(a) (b)

Figure 2.10: Representation of images of a non-point like object placed in different positions [21].

The lenses in the microscope mostly behave like simple convex lenses. As seen in Section 2.1.1, with this type of lenses a collimated beam will be focused into its focal plane. While, a point-like source placed at the focal plane of the lens will be defocused by the lens, generating parallel rays (Fig. 2.6a). The same type of lens can also be used to form an image of a larger object by placing it outside the focal plane. This way, the lens will collect light from every point on the object and produce an image of each point (Fig. 2.10a). Instead, by placing the object at the focal plane, the lens produces defocused parallel beams and only the rays originating from the focal point give a beam parallel to the optical axis. While, other points give oblique parallel beam as in the Fig. 2.6a. For reasons of simplicity, only one of these

points of the object will be considered i.e., the point coinciding with focal point of the lens. A lens can be used either to generate a collimated beam of light from an object or to form an image of the object, depending on where the object is placed in relation to the focal plane. Therefore, it is possible to put an object outside the focal plane of a lens and get an image of that object and then put another object in the focal plane of the same lens and generate a defocused beam of light (pink and green objects in the Fig. 2.10b). This is what happens inside the microscope i.e., optics collect light from a light source, illuminate the specimen, and then form the image of the specimen on the observer´s retina or on a camera sensor.

The optics of a microscope can be divided into two groups (Fig. 2.11). The purpose of the first group is to illuminate the specimen and this group includes the collector lens, the field diaphragm, the condenser aperture diaphragm and the condenser lens. The purpose of the second group is to form an image of the specimen and this group includes the objective lens, the tube lens and the eyepieces. These optics follow are aligned differently in a transmitted light microscope and in a reflected light microscope. For reasons of simplicity, below the alignment of optical components in a transmitted light are introduced first, followed by the alignment of optical components in a reflected light microscope.

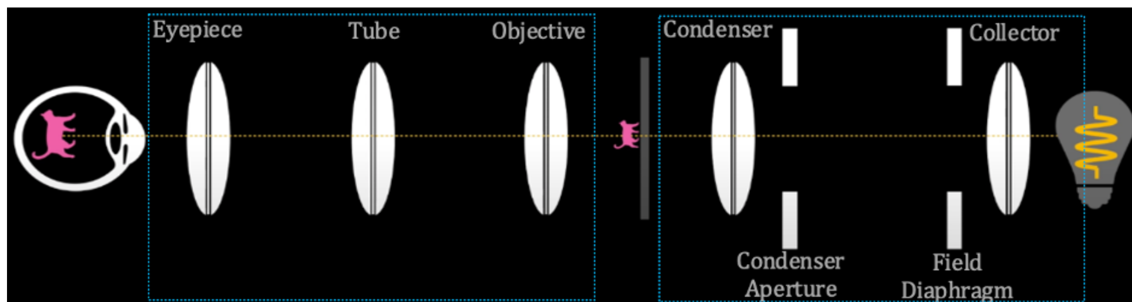

Figure 2.11: The optics of a microscope divided into two groups [21].

Alignment of optical components

Fig. 2.11 shows how the optics are organised and divided in group in a transmitted light microscope. Often light source, collector lens, tube lens and eyepiece are already fixed in an appropriate position. While, condenser lens (with its aperture diaphragm) and objective lens can be moved and the field diaphragm can be opened or closed. All these latter components must be aligned relative to one another to achieve Köhler illumination [15, 21].

The light source employed in a microscope such as a tungsten filament or an array of LEDs

has structure. Therefore, it does not produce an even field of illumination on its own. To evenly illuminate the specimen across the field of view, the optics must be aligned in such a way that an image of light source is in the focal plane of the objective. This way, the objective will produce a defocused light to evenly illuminate the specimen (Fig. 2.12a.1 and 2.12b.1). If the light source is outside the focal plane, then the lens will form an image of the filament and if the image of the filament is focused on or near the specimen the field of view will be unevenly illuminated (Fig. 2.12a.2 and Fig. 2.12b.2).

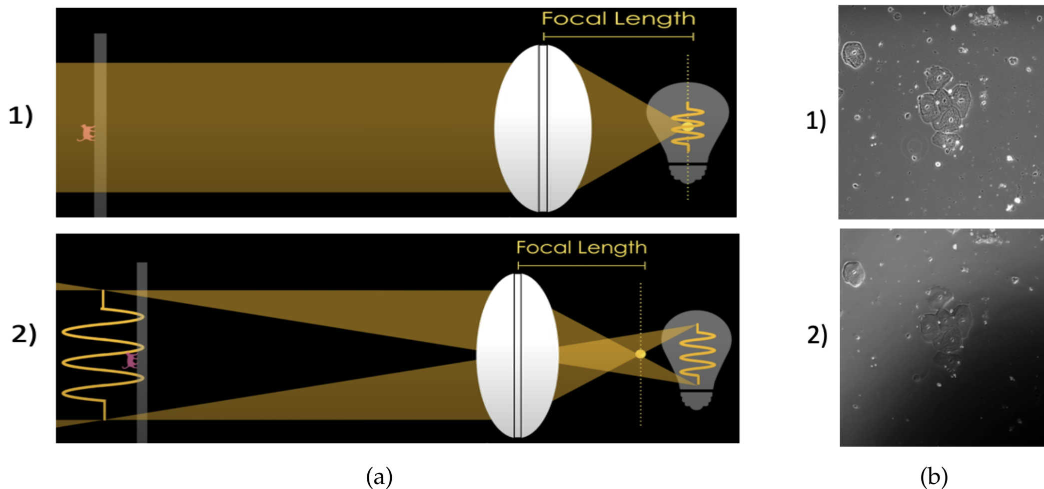

Figure 2.12: Light source at (a.1) and outside (a.2) the focal plane of the lens. The corresponding even (b.1) and uneven (b.2) illumination of the specimen [21].

In a microscope with the two groups of lens of the (Fig. 2.11), two distinct sets of conjugate focal planes can be generated. The concept of the conjugate focal planes is critical in achieving proper Köhler illumination. For the description of the two set of conjugate planes, Fig. 2.13 will be used.

Fig. 2.13 shows a series of lenses lined up one after the other. Placing an object outside (at point A) the focal plane (plane in F_1) of the lens 1, an image of the object will be formed at point B and then the next lens in the series will form an image of that image and so on (points C and D). In this series of lenses, the planes where the images of the object are in focus are called the conjugate focal planes i.e., planes containing the points A, B C, D and perpendicular to the optical axis. With the same set of lenses placing an object at a different point (e.g., point S) a different set of conjugate focal planes is obtained i.e., planes containing the points S, T, U, V and perpendicular to the optical axis. Now putting a second object in

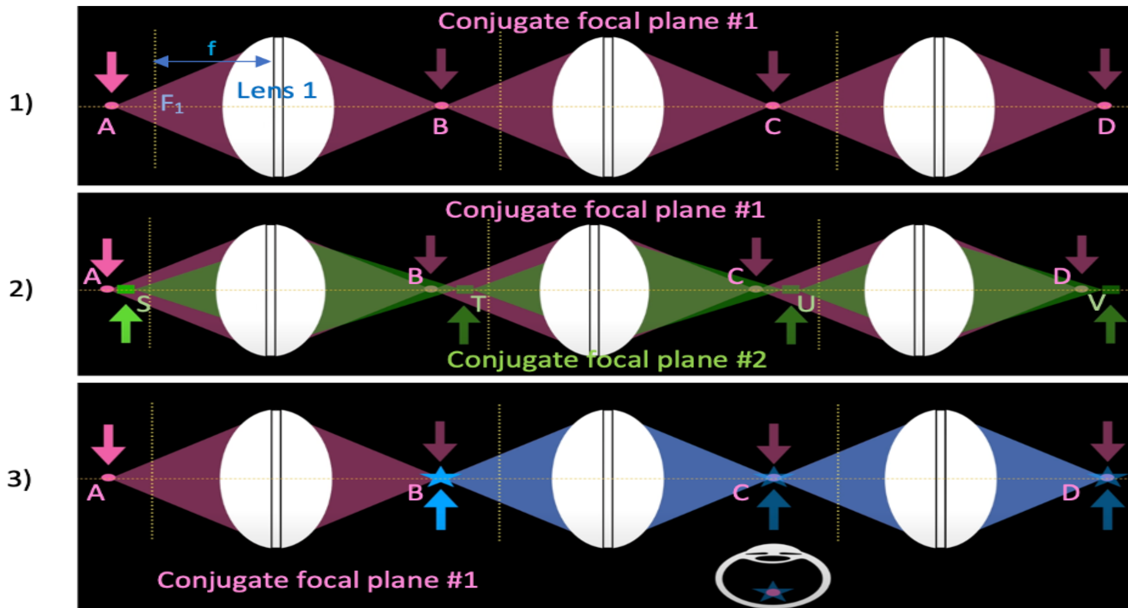

Figure 2.13: Two sets of conjugate focal planes. Position of the objects and their images and the focal plane of the lenses are shown. (1) With a series of lenses lined up one after the other a set of conjugate focal planes can be obtained. (2) Using two objects two sets of conjugate focal planes are generated. (3) The images of the two objects are overlaid in each subsequent conjugate focal plane [21].)

one of the plane of the first conjugate focal planes (point B Fig. 2.13.3) the images of the two objects will be overlaid in each subsequent conjugate focal plane. Looking at one of these conjugate focal planes (e.g., point C Fig. 2.13.3) an overlaid image of both objects will be seen as if the two objects exist in the same plane.

The two distinct sets of conjugate focal planes of a properly aligned microscope are called illumination plane and image plane. As shown in Fig. 2.13.1, if an object is in focus at one plane of a given set of conjugate planes, then it will be in focus also in other planes of the same set of conjugate planes [15]. The comprehension of the last sentence stated is the key point for understanding Köhler illumination method. When a microscope is properly aligned for the Köhler illumination, every optic element is in its proper position. Therefore, to obtain Köhler illumination the optics must be positioned in the focus points of the set of the conjugate planes to which they belong. The set of image planes includes the conjugate focal planes in which the images of the specimen are in focus i.e., the specimen plane, a plane inside the eyepiece tube called the intermediate image plane, retina or the camera and the field diaphragm plane (Fig. 2.14.1). Among the optics to form the image, only the objective needs to be aligned. This can be achieved positioning it in the focal plane to which it belongs.

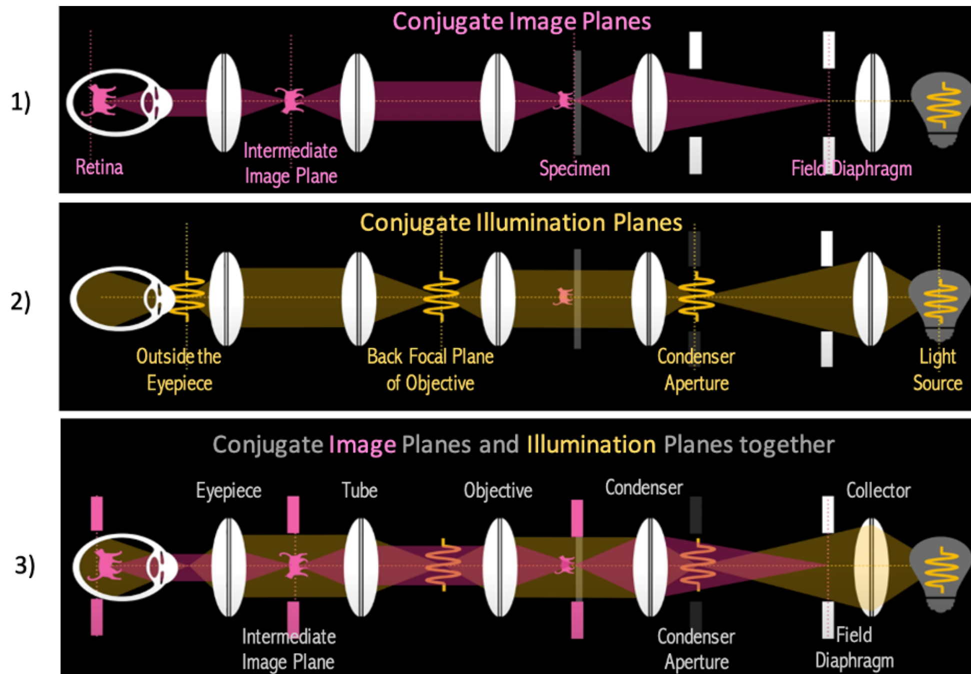

Figure 2.14: Conjugate image and illumination planes (adapted from [21].)

In other terms, the objective can be aligned by focusing on the specimen and obtaining its image on the retina or the camera sensor. The set of illumination planes consists in the back focal plane of the objective, a plane just outside of the eyepiece, and the planes where the light source and the condenser aperture diaphragm are placed (Fig. 2.14.2).

When the optics are aligned in the correct way for Köhler illumination, the light source and its images will be focused in the illumination planes (Fig. 2.14.2). The image of the light source focused on the focal plane of the condenser lens will be collected by it to uniformly illuminate the specimen with defocused light. It is important to make sure that the image of the light source is in the focal plane of the condenser to get an even illumination of the specimen. Since in most modern microscopes the collector lens is fixed in place, it is only possible to move the condenser lens to bring an image of the light source into its the focal plane.

In short terms, if the optics are aligned correctly, the images of the light source and the specimen are focused in their conjugate focal planes (Fig. 2.14.1 and Fig. 2.14.2). Therefore, when the microscope is aligned, the image of the field diaphragm will be superimposed over the image of the specimen since the position of fields diaphragm belongs to the same set of the conjugate image planes (Fig. 2.14.3). The image of the field diaphragm on the specimen is

formed by the the condenser lens. Therefore, the image of the field diaphragm can be used as a reporter whether or not the condenser is in the appropriate position because as stated before, a properly aligned condenser forms an image of the field diaphragm at the specimen while the condenser is illuminating the specimen with defocused light [15].

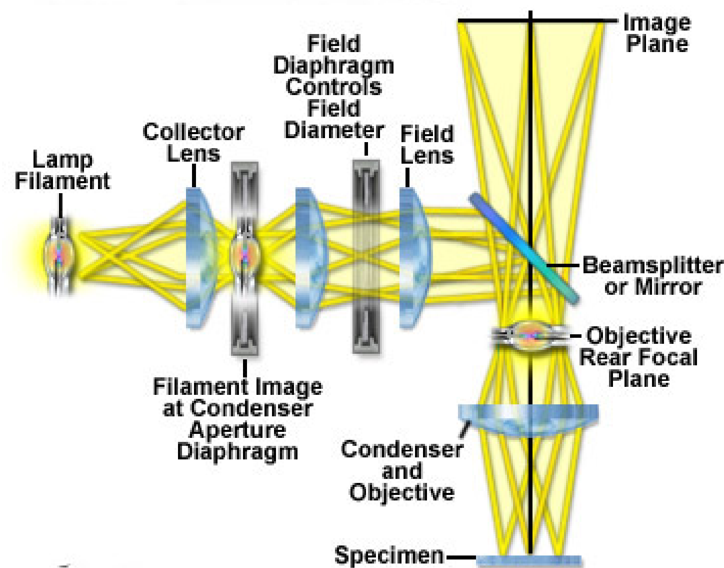

Figure 2.15: Optical components alignment for a Köhler illumination in a reflected light microscope. An image of the lamp filament is focused at the back focal plane of the objective and thus the specimen is evenly illuminated [3].

After having introduced the alignment of optical components for achieving Köhler Illumination in a transmitted light microscope, the alignment of optical components for achieving Köhler Illumination in a reflected light microscope will now be presented. In a reflected light microscope, almost the same optics with the same purpose seen above for a transmitted light microscope can be found. The main difference is their illumination system. There could be a difference in the relative position of the aperture and field diaphragm. However, the aperture diaphragm is always in a focal plane of the set of conjugate illumination planes and the field diaphragm is in a focal plane of the image planes (Fig. 2.15 and Fig. 2.14). In a transmitted light system, the objective and the condenser exist as two different optic parts and they need to be adjusted to have the same numerical aperture. However, as said in Section 2.1.2, in a reflected light microscope the objective serves as a well-corrected condenser on transmission path and as a objective itself on reflection path. Therefore, to achieve Köhler illumination in a reflected light microscope, the system is arranged so that the image of the filament of the

lamp is brought into focus at the plane of the aperture diaphragm. Consequently, there is an image also in focus at the back focal plane of the objective because the two planes belong to the same set of conjugate illumination planes. While the field diaphragm is imaged in the same plane of the specimen and in other conjugate image planes. When everything is in the proper position, the objective collects light from the image of the lamp and illuminates the specimen with defocused light (Fig. 2.15).

The two iris-type diaphragm (aperture and field diaphragm) have an important role in the setup for the Köhler illumination. The aperture diaphragm, conjugate with light source, allows to adjust the angles of the light rays hitting the specimen, crucial in Kerr microscopy. While the field diaphragm, conjugate with the specimen, controls the size of the illuminating field imaged.

2.2 Magneto-optical Microscopy

The previous section (2.1) has presented the basic concepts of light microscopy, which can be used to study microstructures. In particular, reflected light microscopy is often used to image the surface of metallic specimens.

This section introduces magneto-optical microscopy as sub-branch of optical microscopy. Magneto-optical microscopy provides several advantages that are crucial for studying thin-film multilayer structures addressing the different magnetic layers. It is fast (in terms of image acquisition time), contactless (no specimen disturbance), and provides imaging with high lateral resolution (from 1 µm to 100 µm) [22]. In order to exploit these benefits, in this master thesis a reflected light microscope was adapted to work as two different magneto-optical Kerr microscopes (wide-field MOKE and laser-scanning MOKE). A Kerr microscope uses the magneto-optical Kerr effect (MOKE) to visualize magnetic domains down to sub-micrometer scale resolution. The magneto-optical Kerr effect describes the rotation of the polarization axis of light when it is reflected from a magnetized surface of the specimen [17]. Using an analyzer, the rotated part of the light can be detected and thus used to visualize the magnetic domains on the specimen surface. Therefore, in a Kerr microscope the manipulation of the polarization of the light source (used to illuminate the specimen) is crucial to reveal the magnetic domains present on the specimen. In order to better understand the principles of magneto-optical microscopy, in the following section an overview of the polarization state of

light will be provided. Thus, the magneto-optical Kerr effect will be introduced.

2.2.1 Polarization state of light

Light is seen as an electromagnetic wave propagating in space. As electromagnetic wave, light is characterized by a certain polarization describing the direction of the oscillation of the electric field of the wave [23]. An electromagnetic plane wave $\vec{E}_x(z,t)$ with its electric field oriented along x axis (polarization axis) and propagating in the z-direction, has the following expression

$$\vec{E_x}(z,t) = E_{0x} \cos\left(\omega t - kz + \theta_1\right) \vec{a_x} \tag{2.8}$$

where E_{0x} is the amplitude, θ_1 is the phase, ω is the angular frequency and k is the wave number. For simplicity, the phase θ_1 is assumed to be 0, thus the wave (Eq. 2.8) becomes

$$\vec{E_x}(z,t) = E_{0x} \cos\left(\omega t - kz\right) \vec{a_x} \tag{2.9}$$

An another electromagnetic plane wave $\vec{E}_y(z,t)$ propagating always in the same z-direction but with its electric field oriented along y axis (polarization axis), has the following expression

$$\vec{E_y}(z,t) = E_{0y} \cos\left(\omega t - kz + \theta_2\right) \vec{a_y} \tag{2.10}$$

where E_{0y} is the amplitude, ω and k are the same angular frequency and the wave number, respectively.

Due to the validity of the superposition law for electric fields, every wave can also be seen as a superposition of two or more individual waves [23]. Therefore, the two waves (Eq. 2.8 and Eq. 2.10) can be combined to obtain the most general homogeneous plane wave propagating in z direction

$$\vec{E}(z,t) = E_{0x} \cos\left(\omega t - kz)\right) \vec{a_x} + E_{0y} \cos\left(\omega t - kz + \theta_2\right) \vec{a_y}. \tag{2.11}$$

Eq. 2.11 shows that the direction of the electric field $\vec{E}(z,t)$ changes with time, and the tip of the electric field vector describes a geometric locus that differs according to the values assumed by E_{0x}, E_{0y} and θ_2. Thus, the two amplitudes as well as the phases determine three different possible types of polarization: linear, circular and elliptical. Before introducing the three types of polarization, it is worth choosing a fixed point in space to study the wave represented by Eq. 2.11 and for the sake of simplicity z = 0 is chosen. Thus, the Eq. 2.11

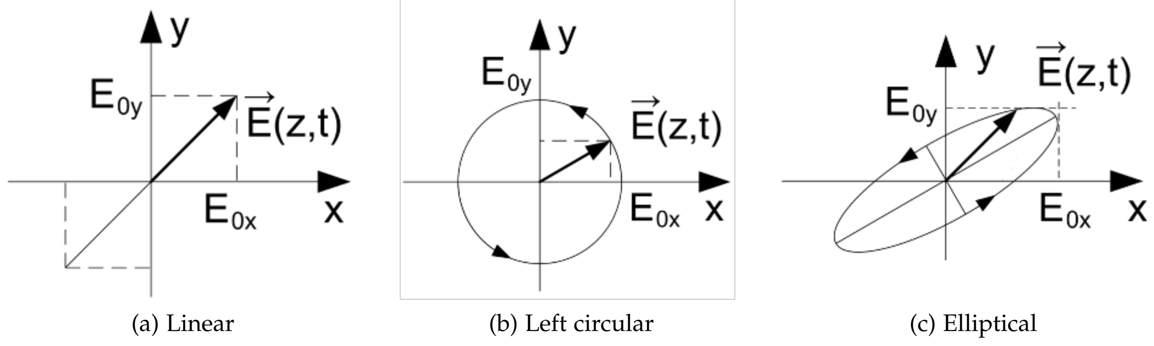

(a) Linear (b) Left circular (c) Elliptical

Figure 2.16: Different types of polarization (adapted from [24]).

becomes

$$\vec{E}(z,t) = E_{0x}\cos(\omega t))\ \vec{a_x} + E_{0y}\cos(\omega t + \theta_2)\ \vec{a_y}. \tag{2.12}$$

Linear polarization: a light beam is linearly polarized if the electric field vector of the wave $\vec{E}(z,t))$, propagating in the z-direction, oscillates only on a straight line perpendicular to the direction of propagation (Fig. 2.16a).
If the amplitudes E_{0x}, E_{0y} of the two waves in Eq. 2.12 are equal (i.e., $E_{0x} = E_{0y} = E_0$) and the phase $\theta_2 = 0$, then the Eq. 2.12 becomes

$$\vec{E}(z,t) = E_0(\vec{a_x} + \vec{a_y})\cos(\omega t). \tag{2.13}$$

In this case, the tip of the electric vector describes at the variation of time t, a segment oriented at $\pi/4$ with respect to the x-axis and the polarization of the wave (Eq. 2.13) is called linear.
If the amplitudes E_{0x}, E_{0y} are different (i.e., $E_{0x} \neq E_{0y}$) and $\theta_2 = 0$, then the Eq. 2.12 becomes

$$\vec{E}(z,t) = (E_{0x}\ \vec{a_x} + E_{0y}\ \vec{a_y})\cos(\omega t). \tag{2.14}$$

In this second case, the tip of the electric vector describes at the variation of time t, a segment oriented by an angle $\phi = \arctan(E_{0y}/E_{0x})$ with respect to the x-axis and the polarization of the wave (Eq. 2.14) is still called linear.

Circular polarization: if the amplitudes E_{0x} and E_{0y} of the two waves in Eq. 2.12 are equal (i.e., $E_{0x} = E_{0y} = E_0$) and $\theta_2 = \frac{\pi}{2}$, then wave in Eq. 2.12 becomes

$$\begin{aligned}\vec{E}(z,t) &= E_0(\cos(\omega t)\ \vec{a_x} + \cos(\omega t + \frac{\pi}{2})\ \vec{a_y}) \\ &= E_0(\cos(\omega t)\ \vec{a_x} - \sin(\omega t)\ \vec{a_y})\ .\end{aligned} \tag{2.15}$$

In this case, the electric field vector has constant amplitude E_0 and the angle formed with the x-axis is

$$\phi = \arctan\left(\frac{-\sin\omega t}{\cos\omega t}\right) = -\omega t \ . \tag{2.16}$$

The tip of the electric field vector of Eq. 2.15 sweeps around in a circle at a radial frequency ω, in a plane around the direction of propagation z. The rotation of the electric field vector of Eq. 2.15 is counterclockwise, as shown in Fig. 2.16b. This wave is called left circularly polarized (LCP) wave [23].

If the phase θ_2 is $-\frac{\pi}{2}$, then the wave in Eq. 2.12 becomes

$$\begin{aligned}\vec{E}(z,t) &= E_0(\cos(\omega t)\ \vec{a_x} + \cos(\omega t - \frac{\pi}{2})\ \vec{a_y}) \\ &= E_0(\cos(\omega t)\ \vec{a_x} + \sin(\omega t)\ \vec{a_y})\ .\end{aligned} \tag{2.17}$$

In this case, the electric field vector has still a constant amplitude E_0 and the angle formed with the x-axis is

$$\phi = \arctan\left(\frac{\sin\omega t}{\cos\omega t}\right) = \omega t \ . \tag{2.18}$$

The rotation of the electric field vector of Eq. 2.17 is clockwise and this wave is called right circularly polarized (RCP) wave [23].

Elliptical polarization: if the amplitudes E_{0x} and E_{0y} of the two waves in Eq. 2.12 are different and $\theta_2 = \pm\frac{\pi}{2}$, then tip of the electric field vector of the Eq. 2.12 describes an ellipse while propagating along z-axis (Fig. 2.16c). As with circular polarization, also a elliptical polarization can be defined as left- or right-handed elliptical polarization depending on the phase ϕ_2 value. Elliptically polarised light is a general polarization state, linear and circular polarisation are merely special cases of elliptical polarization.

Linearly polarized light can also be described as a superposition of a left-circular (LCP) and a right-circular (RCP) wave because of the superposition law [25]. As seen before, the waves described by Eq. 2.9 and Eq. 2.10 represent two linearly polarized waves which polarization axes correspond to the x- and y-axis, respectively . If a left-circular wave with amplitude $E_{LCP} = \frac{E_{0x}}{2}$ and a right-circular wave with same amplitude $E_{RCP} = \frac{E_{0x}}{2}$ are taken and superpositioned, then the linearly polarized light described by Eq. 2.19 will be obtained.

In the following, for simplicity, the waves in $z = 0$ will be considered

$$\begin{aligned}\vec{E}_x(z,t) &= \frac{E_{0x}}{2}(\cos(\omega t)\ \vec{a_x} + \cos(\omega t + \frac{\pi}{2}))\ \vec{a_y} + \cos(\omega t)\ \vec{a_x} + \cos(\omega t - \frac{\pi}{2})\ \vec{a_y}) \\ &= \frac{E_{0x}}{2}(\cos(\omega t)\ \vec{a_x} - \sin(\omega t)\ \vec{a_y}) + \cos(\omega t)\ \vec{a_x} + \sin(\omega t)\ \vec{a_y}) \\ &= E_{0x}\cos(\omega t))\ \vec{a_x}\ .\end{aligned} \tag{2.19}$$

Which is the same linear polarized wave of Eq. 2.9 in $z = 0$. Taking another two left- and right-circular waves with same amplitudes ($E_{LCP2} = \frac{E_{0y}}{2}$ and $E_{RCP2} = \frac{E_{0y}}{2}$) and superpositioning them, the expression of the following wave is obtained (Eq. 2.20)

$$\begin{aligned}\vec{E}_y(z,t) &= \frac{E_{0y}}{2}(\cos(\omega t - \frac{\pi}{2})\ \vec{a_x} + \cos(\omega t))\ \vec{a_y} + \cos(\omega t + \frac{\pi}{2})\ \vec{a_x} + \cos(\omega t)\ \vec{a_y}) \\ &= \frac{E_{0y}}{2}(\sin(\omega t)\ \vec{a_x} + \cos(\omega t)\ \vec{a_y}) - \sin(\omega t)\ \vec{a_x} + \cos(\omega t)\ \vec{a_y}) \\ &= E_{0y}\cos(\omega t))\ \vec{a_y}\ .\end{aligned} \tag{2.20}$$

Which is the same linear polarized wave of the Eq. 2.10 in $z = 0$. Now, if the waves of Eq. 2.19 and Eq. 2.20 are superimposed, the linearly polarization wave of the Eq. 2.14 will be obtained.

2.2.2 Magneto-optical Kerr effect (MOKE)

After having introduced the polarization state of light and more specifically the different types of polarization, this section will explain how the polarization state of light is related to the magneto-optic Kerr effect.

The interaction of light with matter is affected by the magnetic state of the medium and involves its electronic structure. Such interaction between the electromagnetic wave and the magnetically polarized materials results in magneto-optical effects [26]. In 1845, Michael Faraday discovered that the polarization of a linearly polarized light is rotated when it propagates through an external magnetic field. This effect is called Faraday effect. Inspired by the discovery of the Faraday effect, in 1876, John Kerr then found that the polarization axis of a linearly polarized light also rotates when it is reflected from a magnetized surface. This effect is called magneto-optical Kerr effect (MOKE).

The magneto optical Kerr effect is based on the rotation of the polarization axis of light during reflection from a magnetized and reflective specimen. The rotation of the polarization axis is referred to as Kerr rotation and depends on the magnetization of the reflecting surface

[17].

Modes of Polarization Rotation by Reflection at magnetized surfaces

Depending on the plane of incidence of the polarized incident light and the direction of magnetization vector **M** on the specimen, the magneto-optical Kerr effect (MOKE) is classified into three different modes [22] (Fig. 2.17). The plane of incidence is the plane containing the propagation vector $\mathbf{k}^{(i)}$ of the incident light and $\mathbf{k}^{(r)}$ of the reflected light as well as the normal **n** to the specimen surface.

- In the *polar* Moke (Fig. 2.17a) the magnetization **M** is perpendicular to the specimen surface i.e., $\mathbf{M} \parallel \mathbf{n}$, where **n** is the surface normal.
- For the *longitudinal* MOKE (Fig. 2.17b) the magnetization **M** lies in-plane ($\mathbf{M} \perp \mathbf{n}$) and **M** is parallel to the plane of incidence.
- At the *transverse* MOKE (Fig. 2.17c) the magnetization **M** is still in-plane ($\mathbf{M} \perp \mathbf{n}$), but **M** is perpendicular to the plane of incidence.

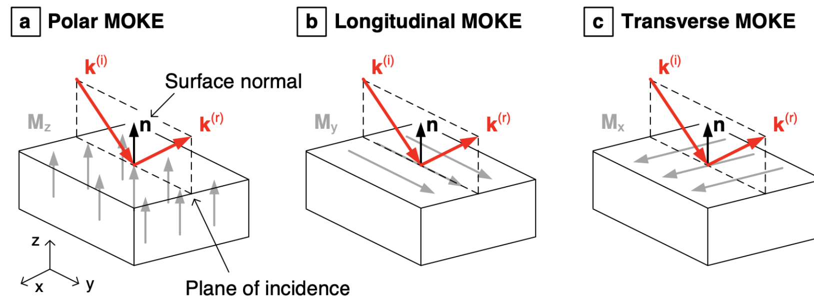

Figure 2.17: Various geometries of the magneto-optical Kerr effect [22]. $\mathbf{k}^{(i)}$, $\mathbf{k}^{(r)}$ are the propagation direction of the incident and reflected wave respectively, **M** is the direction of the specimen magnetization and **n** is the surface normal.

Generally, the observed effect is a superposition of these modes. However, in the following only the polar MOKE is treated since this master thesis focuses only on imaging of magnetic domains of specimens magnetized perpendicular to the the surface.

Polar magneto-optical Kerr effect Fig. 2.18 represents the geometry (a) and the corresponding polarization axis rotation (b) for a normal incident, linear polarized wave which is reflected at the surface of a perpendicular magnetized medium. As a result of the polar MOKE, when

the normal incident wave $\mathbf{k}^{(i)}$ is reflected at the surface, the polarization of the reflected wave $\mathbf{k}^{(r)}$ is rotated by the Kerr angle θ_k. Moreover, the polarization of the reflected wave after the reflection becomes slightly elliptical [17]. The sign of the polarization rotation by the Kerr angle θ_k depends on the direction of the magnetization $\mathbf{M}$ of the specimen. Therefore, the magnetization $\mathbf{M}$ of the magnetic medium can be determined using optical microscopy by analyzing the change of the polarization from the incident to the reflected wave [22].

In the following, a normal incident light ($\mathbf{k}^{(i)} \| \mathbf{n}$) is considered to discuss the polar MOKE ($\mathbf{M}_z \| \mathbf{n}$) because the Kerr intensity is higher in the polar MOKE for a normal incident light [17].

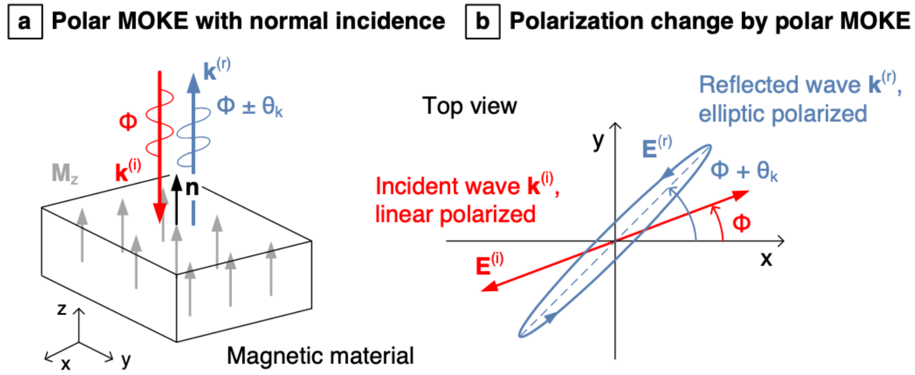

Figure 2.18: The incident wave $\mathbf{k}^{(i)}$ parallel to $\mathbf{n}$ is reflected at the surface of the perpendicular magnetized material (a). The polarization of the reflected wave $\mathbf{k}^{(r)}$ is rotated by Kerr angle θ_k and transformed to elliptic polarization (b) [22].

A linearly polarized wave can be express as a superposition of two circularly polarized waves with equal amplitude. This has already been verified in Section 2.2.1 by obtaining a linear polarized wave from the sum of a left- and right-circularly polarized waves. According to Fig. 2.19a, the incident linear polarized wave ($\vec{E}^{(i)}{}_{\mathrm{LP}}$) is expressed by the sum of a right circularly polarized ($\vec{E}^{(i)}{}_{\mathrm{RCP}}$) wave and a left circularly polarized ($\vec{E}^{(i)}{}_{\mathrm{LCP}}$) wave:

$$\vec{E}^{(i)}{}_{\mathrm{LP}} = \vec{E}^{(i)}{}_{\mathrm{RCP}} + \vec{E}^{(i)}{}_{\mathrm{LCP}}. \tag{2.21}$$

When a linearly polarized incident light wave as Eq. 2.21 (Fig. 2.19a) is reflected from a magnetized surface, each circular polarized wave of the incident light sees a different refractive indice.

At the magnetic surface, the magnetization $\mathbf{M}$ in the medium, due to quantum mechanical spin-orbit interactions produces anisotropic properties, which lead to different refractive indices for left- and right-circularly incident polarized light [24]. Thus, their propagation

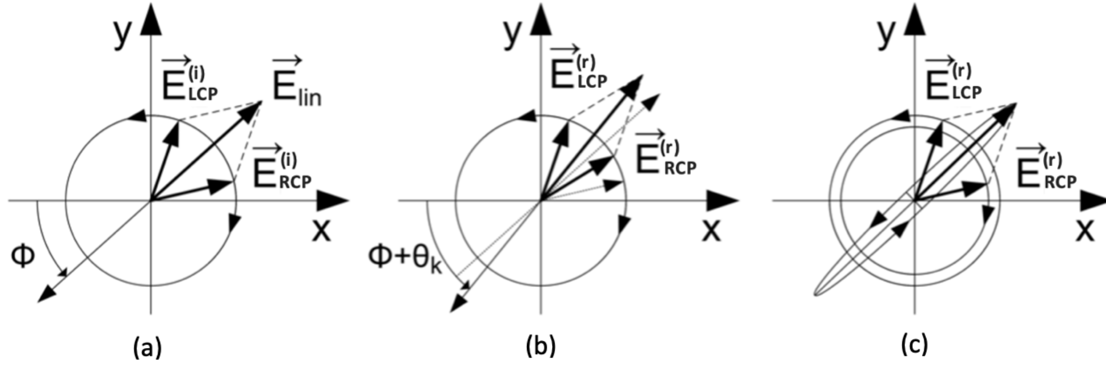

Figure 2.19: Superposition of two circularly polarized waves to form a linearly polarized wave (adapted from [24]). The linear polarized incident wave $\mathbf{k}^{(i)}$ is seen as superposition of two contrary circularly[3] polarized waves (a). Due to a phase shift (b) and an amplitude change (c) between $\mathbf{E}^{(r)}{}_{LCP}$ and $\mathbf{E}^{(r)}{}_{RCP}$ waves, the resulting polarization of the reflected wave $\mathbf{k}^{(r)}$ is elliptic and rotated by the Kerr angle θ_k.

speeds are also different, which means that one circular wave is delayed compared to the other. As a result, the polarization axis of the reflected wave, resulting from superposition of the reflected circularly polarized waves, is rotated by the Kerr angle θ_k (Fig. 2.19b).

Furthermore, there is an absorption of the wave in the magnetized medium which is different for left and right circular waves [24]. As a result, the amplitude of one circular wave is attenuated compared to the other and thus, the linear polarized incident wave becomes slightly elliptical (Fig. 2.19c).

After having discussed the basic concepts of magneto-optical microscopy, the Kerr effect and the modes of light polarization rotation, the next section will draw on this to explain how the design, implementation and characterization of the wide-field MOKE microscope have been conducted during this project. In particular, an in-depth discussion relating how the Kerr effect was measured and the polarization of light was considered during the microscope implementation are reported in Section 3.2.3.

3 Design, Implementation and Characterization

Section 2 has introduced some basic concepts in microscopy, including lenses and geometrical optics, objectives and resolution, Köhler illumination. Moreover, Section 2 gave us an overview of magneto-optical microscopy, including the polarization state of light and the magneto-optical Kerr effect. This section will draw on those concepts and employ them to give an overview of the adaptation of a Zeiss-AXIOMAT as a Kerr microscope for observing magnetic domains exploiting the magneto-optical Kerr effect. First, the basic design of a Kerr microscope and its optical components are introduced. Thus, the Zeiss-AXIOMAT is described as well as the adaptation, improvement or substitution of each component.

3.1 Magneto-optical Kerr Microscope

As stated above, the Kerr microscope allows the observation of magnetic domains exploiting the magneto-optical Kerr effect. The basic operation of a Kerr microscope is equivalent to the one of an ordinary reflected light microscope, whose optical path is shown in Fig. 2.15. However, the Kerr microscope (Fig. 3.1) exploits a polarization-based contrast technique and relies on the rotation of the polarization axis of incident light caused by the reflection on materials with different magnetic properties. In order to detect the magneto-optical Kerr effect, specific components capable of measuring the polarization change of light are needed, i.e. polarizer and analyzer. A polarizer placed in the incident path provides linearly polarized light. The analyzer, which is also a polarizer in itself, is placed in the exit path and allows the measurement of the polarization change by observing the intensity change detected by the camera sensor. The sliders used to set their value is shown in Fig. 3.1. In addition to the polarizer and analyzer, a phase shifter/retardation plate is needed to correct the polarization of the reflected light, which becomes slightly elliptic due to the magneto-optical Kerr effect

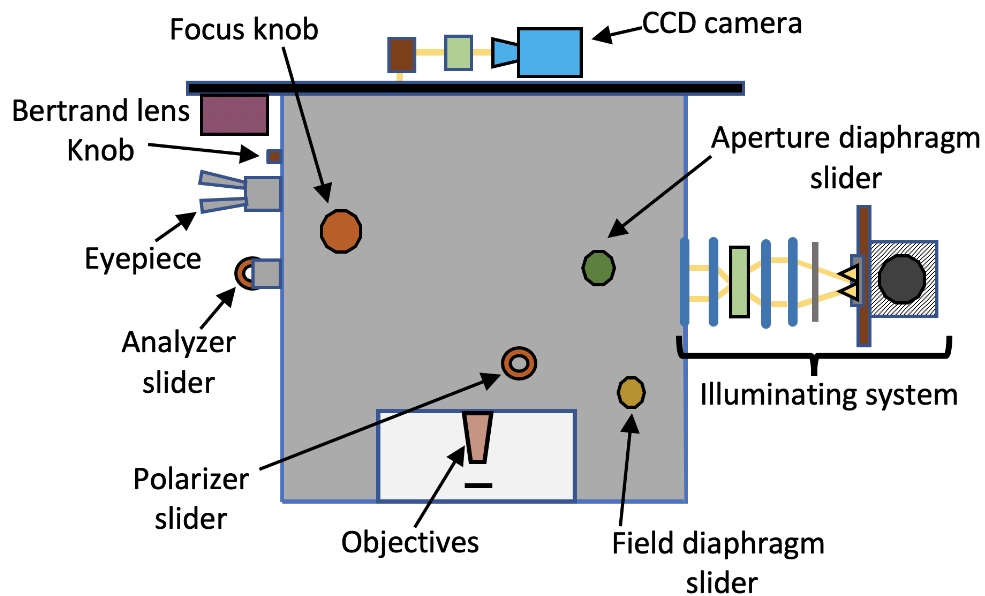

Figure 3.1: Representation of the wide-field MOKE microscope based on a common reflected light microscope enhanced by a polarizer, an analyzer and a Bertrand lens.

(see Section 2.2.2). With this phase shifter, it is possible to convert linear, circular and elliptical polarization into each other (one polarization direction of a light beam is delayed in relation to the other [17]. Finally, a Bertrand lens is employed to select which magneto-optical Kerr effect (i.e., longitudinal, transverse or polar) has to be measured. A Bertrand lens projects an interference pattern formed at the objective back focal plane into focus at the microscope image plane. Fig. 3.1 shows the knob, on Zeiss-AXIOMAT, used to swing the Bertrand lens in or out.

There are two different magneto-optical microscopes based on the magneto-optical Kerr effect (MOKE): The laser-scanning MOKE microscope (LMOKE) and wide-feld MOKE microscope (WMOKE). Their characteristics and differences are briefly described below.

Laser-scanning MOKE microscope (LMOKE)

In the laser-scanning MOKE microscope, a pulsed laser beam is focused on a tiny spot on the specimen in order to measure the magnetic switching behavior by hysteresis measurement. The polarization of the incident beam, due to the magneto-optical Kerr effect, is rotated according to the local magnetization. Hence, it is possible to measure the behavior of the magnetic switch at every point by scanning the region of interest on the specimen surface. The

position of the polarizer and the analyzer along the optical path is shown in Fig. 3.2 and the sliders used to set their value are shown in Fig. 3.1. Beside the optical components needed for a Kerr microscope (which have been introduced above), the laser-scanning MOKE microscope needs some additional components such as a laser, polarizing beam splitter and photodiodes (Fig. 3.2). The laser-scanning MOKE microscope allows to image the specimen surface by scanning with a focused laser beam. Nevertheless, if the users are not only interested in the magnetic behavior of a tiny spot, but of a wider area, then the laser-scanning MOKE microscope becomes inadequate. In this case, the wide-field MOKE microscope is preferred.

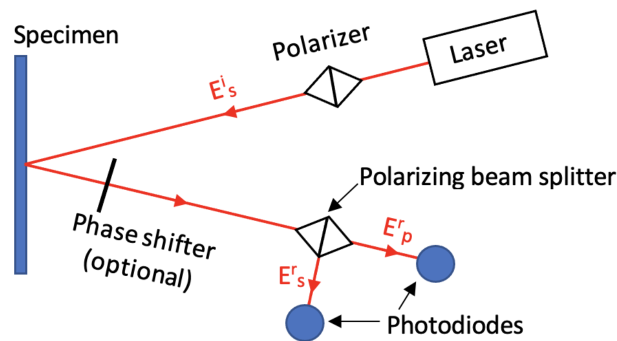

Figure 3.2: Representation of the optical path of a laser-scanning MOKE microscope. The pulsed laser light is S polarized and focused on the specimen, where the polarization is rotated by the magneto-optical Kerr effect. The reflected light is guided to the polarizing beam splitter, which separates the polarization into its S and P components. Then these components are captured by two photodiodes.

Wide-field MOKE microscope (WMOKE)

The wide-field MOKE microscope is essentially different from the laser-scanning MOKE microscope. The laser-scanning MOKE microscope employs a pulsed laser beam to scan a tiny spot of the specimen and generates domain images through multiple sequential scans. This process is relatively slow. Whereas, the advantage of the wide-field MOKE microscope is that it employs a LED instead of the laser beam to illuminate a wide area of the specimen and a camera to detect the reflected light coming from the specimen, which allows fast imaging of magnetic domains. For the wide-field MOKE microscope the components needed are the same as the ones in the Kerr microscope described above in Fig. 3.1, which represents the Zeiss-AXIOMAT after its adaption as a wide-field MOKE microscope.

3.2 Kerr Microscope Development

The section above provided a general understanding of the basic design of a Kerr microscope and its optical components as well as of the main similarities and differences between a laser-scanning and wide-field MOKE microscope. Now, the Zeiss-AXIOMAT is introduced as well as the adaptation, improvement or substitution of its components with the final aim of adapting it as wide-field and laser-scanning MOKE. More specifically, the following steps are presented: improvement of the light source, visualization improvement of magnetic domains through addition of a camera system, adjustment of the optical system and obtainment of better objectives control through a positioning system with graphical user interface (GUI).

Given the limited duration of this project, only the setup of a wide-field MOKE microscope was conducted. Nevertheless, all studies and designs have been done taking into account the laser-scanning MOKE microscope and the outcomes of this master thesis will allow its future implementation.

3.2.1 Improvement of the light source

The initial Zeiss-AXIOMAT microscope presented a 100 W tungsten-halogen lamp, which had several limitations compared to a LED matrix. Current LED illuminators can achieve collimated output power of several watts. Moreover, the LEDs have high durability and low noise [17]. This makes the illumination source have high efficiency and high brightness. It is also possible to implement DC and pulsed operation modes, which allow an easy adaption of the imaging schemes for time-resolved microscopy applications [17].

For the wide-field MOKE microscope, the halogen lamp already present in the microscope was substituted with a high-power LED matrix. The use of high-power LED matrix as light source would allow more light power in the system than the halogen lamp. As new light source, a 100 W blue LED matrix ($\lambda = 470\,\text{nm}$ and dimension of $20\,\text{mm} \times 20\,\text{mm}$) was positioned inside the lamp house of the microscope (Fig. 3.3). In particular, the 100 W blue LED matrix was selected because the quantum efficiency of the CCD camera used in this project is higher for the wavelength of the blue light (see Section 3.2.2). Before fixing the LEDs plate, some thermal paste for an efficient transfer of heat generated from the plate was used. To drive the LEDs, a LED driver designed by another student was employed [27]. This driver allows two different modes of use of the light source: maximum power mode or dimming

mode.

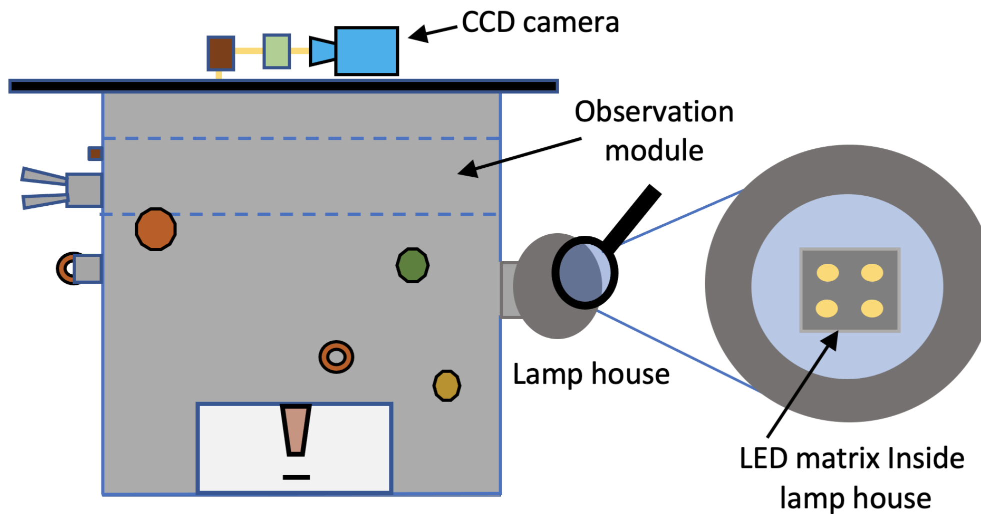

Figure 3.3: Substitution of the halogen lamp with a LED matrix. The LED matrix is placed inside the lamp house. The observation module contains the light paths used to guide the light towards the eyepiece or the camera.

Zeiss-AXIOMAT offers several light paths though the observation module (Fig. 3.3). To understand which of them allowed a better illumination of the specimen through more light, an optical power meter [28] was used together with a photodiode sensor to measure the light intensity along the optical paths. During the measurement, electrical coupling problems between the sensor and the LEDs driver were encountered. This was related to a bad isolation of the sensor. Therefore, this instrument was substituted by a smaller portable photodetector built specifically for this purpose (see Section 3.3). This allowed a better measurement of the amount of light along the optical paths.

The photodetector was also employed together with an oscilloscope [29] to find the PWM frequency of the LEDs driver, which was missing and yet required for the employment of the LED driver for future improvement of the wide-field MOKE microscope. It was found that the PWM signal had a duty cycle of 50% and a period of 17 µs (i.e., a frequency of 58.8 kHz).

Before proceeding with the description of the adaptation of the Zeiss-AXIOMAT as a wide-field MOKE microscope, the next paragraph briefly introduces the light paths that were selected and employed for the domain imaging.

Light paths The microscope Zeiss-AXIOMAT through the observation module (Fig. 3.3) provides different optical paths which can be chosen according to the preferred use. For this

project, as shown in Fig. 3.1, the binocular tube 1 for the eyepiece and the opening on the objective module for the CCD camera were employed (as shown in Fig. 3.4, e.g. Number 21.2). To guide the light to the eyepiece or to the camera the 5 optical paths in Fig. 3.4 were used. In the following, the 5 optical paths are described to understand how they can be employed.

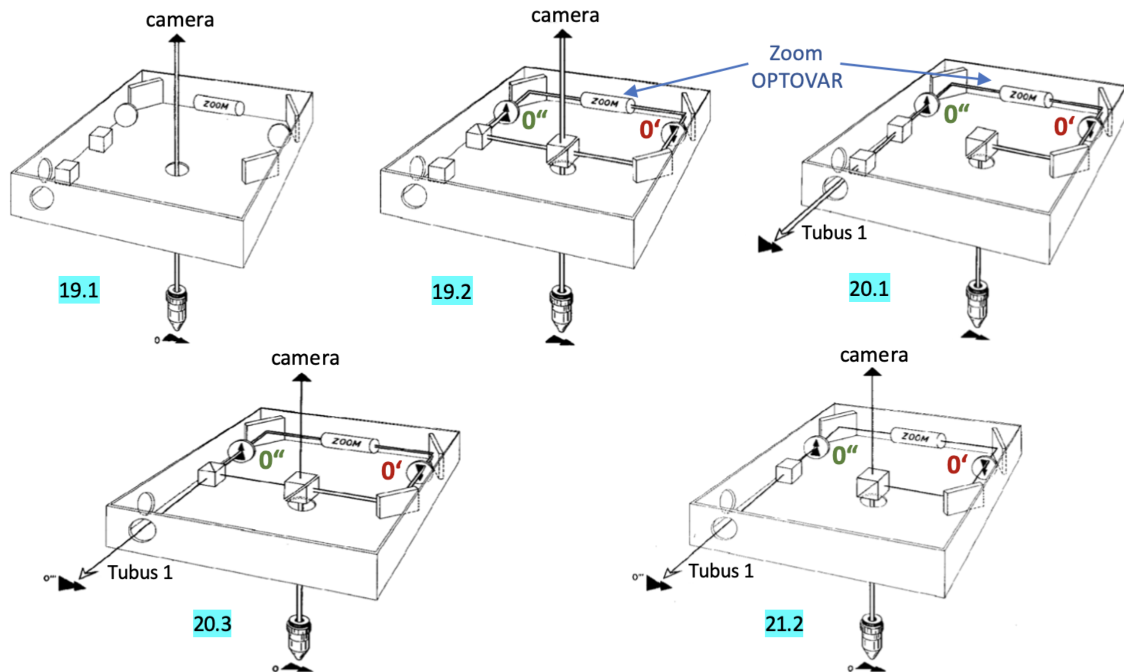

Figure 3.4: Optical paths inside the observation module of Zeiss-AXIOMAT. These 5 optical paths can be used to direct the light reflected from the specimen toward the camera or the eyepiece. The optical path numbers in the figure are equal to the numbers used in [30].

Optical path 19.1 produces an image of the specimen in the camera. This optical path is best suited when only the camera is employed to obtain domain images, in fact the light transmitted to the camera is greater as there are few optical elements along the path.

Optical path 19.2 produces an image of the specimen in the camera via intermediate image 0′, zoom OPTOVAR and intermediate image 0″. In the observation module, the real intermediate image 0′ of the specimen is formed at the objective magnification, e.g. magnification of 25x with a 25x objective. The zoom OPTOVER from the image 0′ produces the image 0″ which is magnified by a factor between 0.8x and 3.2x (e.g, final magnification between 20x and 80x with the objective 25x). This light path is best suited when the camera and the zoom OPTOVAR are employed.

Optical path 20.1 produces an image of the specimen into the tube 1 via zoom OPTOVAR.

Optical path 20.3 produces an image of the specimen into the tube 1 and the camera via zoom OPTOVAR. This light path is employed to bring both camera and eyepiece into focus.

Optical path 21.2 produces two different images: the first image is the 0′, which goes directly into the camera, and the second is 0″, which goes inside the tube 1 via zoom OPTOVAR. The two images coincide only when the zoom OPTOVAR is set to 1.

All these optical paths are created through three beam splitters incorporated within the observation module. To select the optical path, it is necessary to switch them as described in the datasheet (from page 19 to 21 in [30]) from outside with the knurled knobs.

The observation module contains also the Bertrand lens to observe the objective back focal plane. The observation of the back focal plane is important to improve the Kerr sensitivity which allows a higher contrast in the final image taken by the CCD camera (see also *Achievement of higher levels of Kerr sensitivity* in Section 3.2.3). The knob that allows the use of the Bertrand lens is shown in Fig. 3.1.

After the selection of the light paths, the next step was the installation of the CCD camera (see Section 3.2.2) in order to acquire the domain images. For this project, the specimen "Co/Ir/Pt-NM021-2017", the LEDs at maximum power and primarily the 25x and the 50x objectives were used. The first images showed some domains, but the results were not satisfactory. The best image presented bad contrast as well as some parts brighter than others (this issue is addressed in Section 2.1.3, see Fig 2.12). This image had an exposure time of 500 ms, meaning that high noise was present since the integration time of the light on the sensors was high. After accurate examination, it emerged that the output power of the LEDs was changing over time (meaning that there was LEDs degradation), Köhler illumination was not respected, ambient light was filtering into the box where the camera was placed, and dust along the optic paths was creating disturbance. In the following, the steps undertaken to address these problems will be described.

LEDs degradation

To verify the LEDs degradation, a MATLAB script provided by the manufacturer of the CCD camera was adapted [31]. This modified version of the script takes an image every 30 minutes, gets the pixel values of the camera and calculates an average of these values. The script ran for 6 hours. Analyzing the data obtained through this script, no degradation of the LEDs was encountered. Moreover, it emerged that some of the camera pixels did not give a significant

value. The 0.16% of the pixels were dead, but since this number was so low, it did not cause any visual problems in the final image and did not represent a problem.

The analysis through the MATLAB script revealed that there was no apparent LEDs degradation. Nevertheless, few months later more than half of the LEDs of the LED matrix were not working anymore. This malfunction could be related to low product quality and inefficient heat dissipation. Prolonged heat can significantly reduce the useful life of a LED matrix. To overcome this, a new white light LED matrix (same model of the blue LED matrix) was employed as well as a new heat sink with a fan for better heat dissipation. Afterwards, no further LEDs degradation was encountered during the development of the wide-field MOKE microscope.

Köhler illumination setup

As seen above, beside LEDs degradation, Köhler illumination had also an important role on the quality of the domain images. In particular, the LED matrix plate fixed inside the lamp house was further away from its appropriate position for the achievement of Köhler illumination (Fig. 3.3), i.e. it was not in a focus point belonging to the set of illumination planes (see Section 2.1.3, Fig. 2.15) of the microscope. Therefore, the specimen was not evenly illuminated since there was no image of the light source at the back focal plane of the objectives. In particular, the Bertrand lens was used to verify if the LEDs image was in focus at the back focal plane of the objectives. The back focal plane and the aperture plane belong to the same set of conjugate illumination plane. Therefore, to achieve Köhler illumination an image of the light source needed to be focused at the aperture plane (Fig. 3.5.b) so that it could be also in focus at the back focal plane of the objectives.

The achievement of Köhler illumination required to modify a part of the Zeiss-AXIOMAT illuminating system. The main modifications, which allowed us to take domain images with good and satisfactory contrast are presented below.

Substitution of the lamp house and collector lens For bringing an image of the LED matrix to its appropriate position (i.e., aperture plane) and achieve Köhler illumination, the lamp house was substituted with a new part (Fig. 3.5). This new part consisted in a copper plate containing the LED matrix with a heatsink to dissipate the heat and in a new aspherical condenser lens (Fig. 3.5.b). Thanks to the addition of this new part, it was possible

to move the copper plate in one direction: along the illumination path but not vertically. Nevertheless, the vertical movement would have been important to center the LED matrix for the Köhler illumination. Given that no vertical movement was possible, an alternative solution to circumvent this problem was adopted: the LED matrix was centered before fixing it on the copper plate. As stated above, to achieve Köhler illumination a new part consisting in a

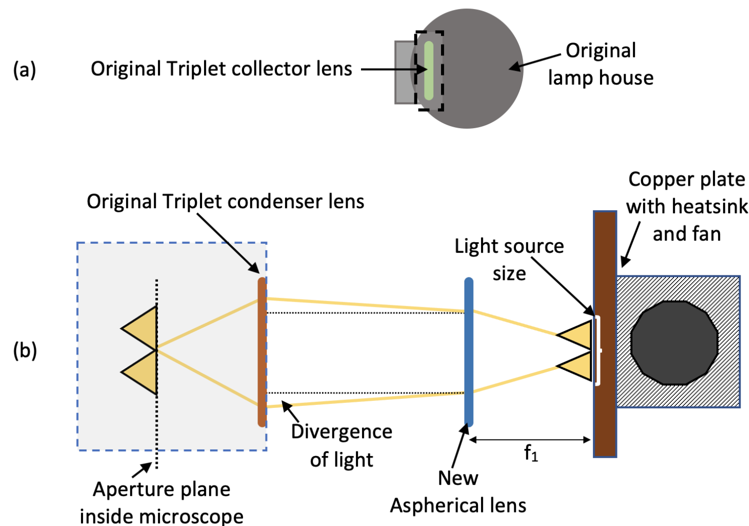

Figure 3.5: (a) Original lamp house with its Triplet collector lens. (b) Substitution of the lamp house with a copper plate, a heatsink and a fan to dissipate the heat. It is only possible to move the copper plate left or right. A new aspherical lens is added to collimate the light. While, the original Triplet condenser lens is still used.

copper plate containing the LED matrix with a heatsink and in a new aspherical condenser lens was added. After having seen the advantages of the new copper plate, the advantages of the new aspherical condenser lens will be explained. The new lens was added because the triplet collector lens (Fig. 3.5.a) inside the lamp house did not fit into the design and an alternative solution to collimate the light from the LED matrix was needed. When selecting the new aspherical lens, several aspects were considered. First, the beam of the LED matrix is usually strongly divergent, therefore a lens with wide numerical aperture was needed. Second, to gather as much light as possible from the LED matrix, a lens with short focal length was required. Third, the diameter of the collimated beam needed to be about 30 mm to fit the dimension of the entrance of the Zeiss-AXIOMAT microscope. In fact, due to the large divergence of the LED matrix output, the collimated beam has generally the same diameter as the lens and thus the diameter of the collimated beam is determined by the diameter of the lens. Fourth, the divergence of the collimated beam was also taken into consideration: to

minimize the divergence of a collimated beam two factors must be balanced, i.e. the focal length of the lens and the size of the light source (Fig. 3.5.b). Regarding the focal length, it needs to be increased in order to achieve ideal collimation (no divergence). Regarding the size of the light source, it must be minimized. However, if the focal length increases, the light source needs to be placed far away from the collector lens to achieve collimation. But this means that the lens will capture less light and the total power of the generated beam will be reduced. Nevertheless, there will be always some degree of divergence when we collimate the light. This divergence exists because as the size of the light source increases, the distance from the light source to the optical axis also increases, and therefore, the angle of the final light beam relative to the optical axis also increases. Taking into account all these factors and also the lens availability on the market, the lens ACL50832U [32] was selected. This lens has a diameter of 50.8 mm, 17 mm back focal length and a numerical aperture of 0.76. Moreover, ACL50832U is an aspheric lens which reduces spherical aberrations (see Section 2.1.1).

After the addition of the aspherical lens, Köhler illumination was achieved, i.e. an image of the LED matrix was in focus at the aperture plane, and thus also at the back focal plane of the objective lens. New domain images were taken to check the improvement of the illuminating system. The domain images taken with the 25x improved but with the 50x, the exposure time still needed to be kept high. The two images still lacked satisfactory contrast for two reasons. First, the camera was not in the same image plane of the eyepiece (meaning that if Köhler illumination was achieved for the eyepiece, it was not achieved for the camera); and second, not all LED points were visible at the back focal plane of the objectives. To solve the first issue, the camera sensor was put in focus in one of the focus planes of the set of the image planes. This was done by aligning the camera so that the image of the specimen was in focus both in the eyepiece and on the monitor i.e., on the camera sensor (see Section 3.2.2). Thus, Köhler illumination was achieved also for the camera thanks to the proper alignment of the two sets of conjugate focal planes: image plane and illumination plane (see Section 2.1.3). To solve the second issue relating the small number of LED points visible at the back focal plane, an image of the whole LED matrix needed to be placed in focus at the back focal plane to gain as much light as possible. However, a trade-off between having the whole LED matrix in focus (Case A in Fig. 3.6) and having a higher light intensity but with only part of the source in focus (Case B in Fig. 3.6) was encountered. A solution in-between was adopted, which was found experimentally and which allowed the obtainment of a good image quality of the

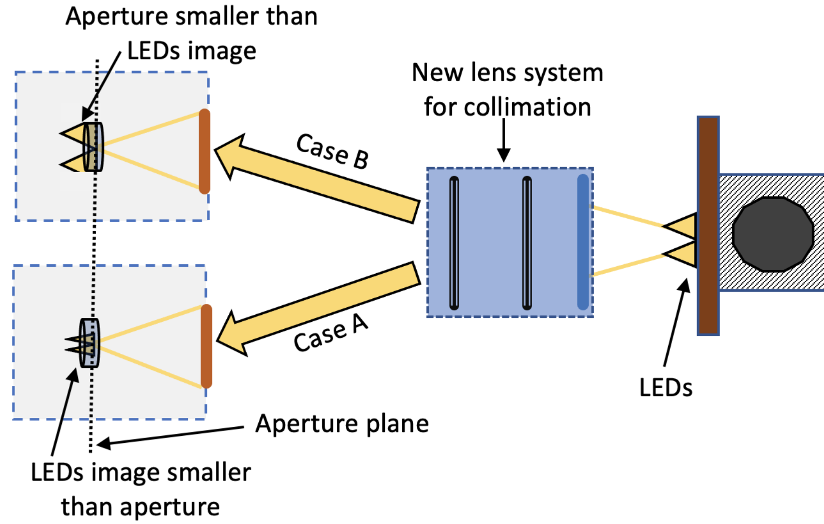

Figure 3.6: Trade-off between light size and light intensity. Case A: the image size of the LEDs is smaller therefore it fits inside the aperture. However, compared to case B, the light intensity obtained is lower. Case B: the image size of the LEDs is bigger and it does not fit inside the aperture. However, the light intensity obtained is higher than case A.

domains. Before adopting this solution, only part of the LED matrix was visible because along the optical path the image of the LED matrix was magnified. Through a rough calculation referring to the configuration 1 depicted in Fig. 3.7a the magnification M_{source} at the aperture plane was derived. For the following calculation, paraxial approximation was assumed i.e., the rays make a small angle with the optical axis:

$$\begin{aligned} Y_1 &= \theta f_1 \\ Y_2 &= \theta f_2 \end{aligned} \quad \rightarrow \quad M_{source} = \frac{Y_2}{Y_1} = \frac{f_2}{f_1} = \frac{60}{17} = 3.53\,. \tag{3.1}$$

In Eq. 3.1, f_1 represent the back focal length of the aspheric condenser lens (back focal length: 17 mm[1]), which was used to collimate the light coming from the LED matrix. Moreover, in Eq. 3.1, f_2 represents the back focal length of a plano convex lens obtained from the triplet condenser lens (Fig. 3.5.b), which was used to focus the collimated light at the aperture plane. The triplet condenser lens (focusing lens) consists in three lenses. From this triplet lens, only the positive lens with plano convex shape (60 mm) was used because the triplet lens gave coupling problems with the laser used for the laser-scanning MOKE microscope. As no information about this lens was available, the focal length was calculated in the following way: a light source was collimated through the aspherical lens (17 mm), then the collimated light

[1]From now on the back focal length will be put in brackets next to each lens to better distinguish between the various lenses.

was focused through the positive lens and the distance from the lens vertex was measured. Thus, the back focal plane of about 60 mm was calculated. In this calculation, to ensure that the light was properly collimated, the collimated light was projected onto the wall (representing a theoretical infinite distance) with the aim of obtaining a clear image of the LED matrix.

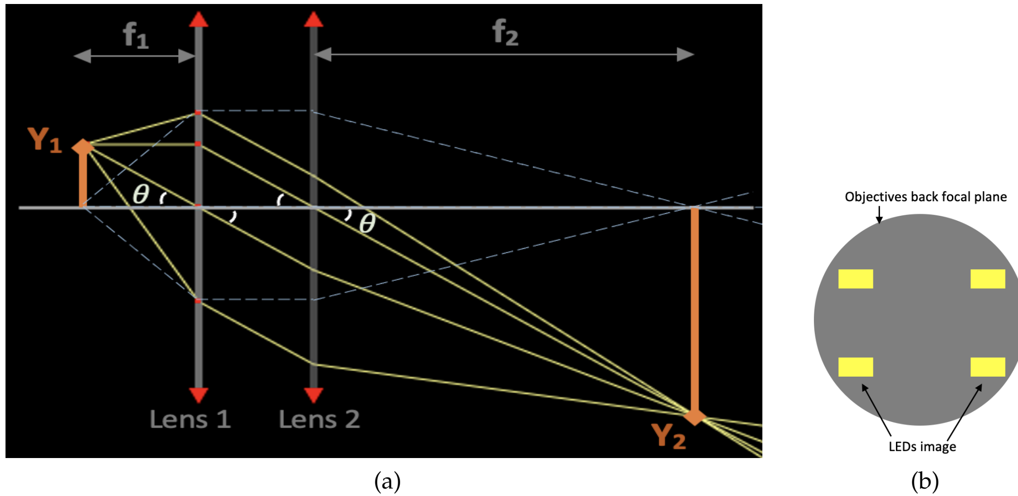

Figure 3.7: Source magnification caused by two lenses. (a) Configuration 1: Lens 1 is the aspheric condenser lens (17 mm) and Lens 2 is the plano convex focusing lens (60 mm). The distances f_1 and f_2 correspond to the back focal lengths of the lenses. The two oblique rays make the same angle θ with the optical axis. (b) LED matrix image at the back focal plane of the objectives in configuration 1. Only 4 out of 60 LEDs are visible.

Coming back to the rough calculation (Eq. 3.1), this was useful to get an approximate idea of the M_{source} in configuration 1 and to design the future illumination paths. Configuration 1 was implemented on the Zeiss-AXIOMAT and only 4 LEDs out 60 were found at the back focal plane of the objective 25x (Fig. 3.7b). Therefore, different configurations with different type of lenses and LEDs to reduce the image size were adopted. The amount of light in each configuration was measured using the photodetector appositely adapted for this project (as described in Section 3.3). These configurations were first tried on paper, then verified on an online simulator [12], then set up on a smaller scale using small lenses and LEDs. These lenses were available beforehand and among them there was a plano convex lens with same diameter (i.e., 50.8 mm) of the starting aspherical lens (17 mm), which was included in the design. The back focal length (40 mm) of the plano convex lens was measured in the same way as for the focusing lens (60 mm). In the following, some of the configurations tried before choosing the most suitable one for this project will be introduced:

Configuration 2: an intermediate smaller image of the LED matrix was focused with Lens

1 at the focal point of Lens 2 in order to use this intermediate image as a smaller light source (Fig. 3.8). Then the light coming from this image was collimated and focused at the aperture plane.

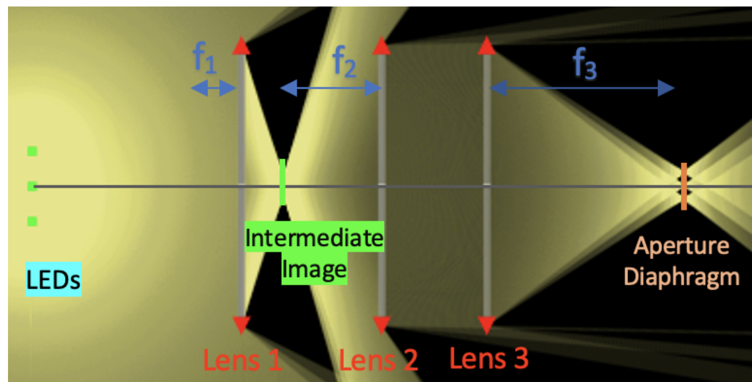

Figure 3.8: Configuration 2: Lens 1 is the aspheric condenser lens (32 mm), Lens 2 is the plano convex lens (40 mm) and Lens 3 is the plano convex focusing lens (60 mm). The distances f_1, f_2 and f_3 correspond to the back focal lengths of the lenses.

Configuration 3: The plano convex lens (40 mm) was employed to collimate the light from the LED matrix and the inner lens (60 mm) to focus the image of the LED matrix (Fig. 3.9). In this case, the magnification M_{source} was smaller compared to the case of configuration 1 but part of light was lost since the LED matrix was more distant from the first lens (40 mm).

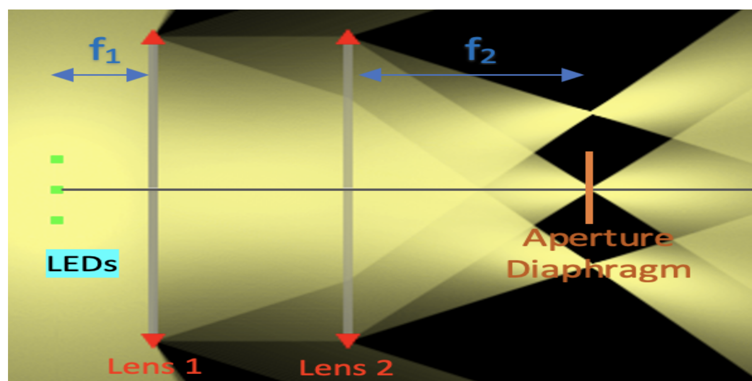

Figure 3.9: Configuration 3: Lens 1 is the plano convex lens (40 mm), Lens 2 is the plano convex focusing lens (60 mm). The distances f_1 and f_2 correspond to the back focal lengths of the lenses. The image size of the light source is larger than the diameter of the aperture diaphragm and therefore only part of the light passes through the aperture.

Only configuration 1 among the above mentioned configurations produced acceptable images of the magnetic domains. Nevertheless, the images captured with the 50x still suffered from lack of contrast. This was due to the fact that in configuration 1, the 4 LEDs were spaced

in such a way that at the center of the image of the back focal plane there was no LEDs image. To solve this issue, configuration 4 was proposed. In this configuration, the original triplet collector lens (with a back focal length of 24 mm) was also included (Fig. 3.5a), but it was used to focus the light instead of collimating it.

Configuration 4: in this configuration, an aspheric lens (17 mm) was used to collimate the light from the LED matrix, then the original triplet collector lens (24 mm) was used to focus an intermediate smaller image of the LED matrix at the back focal plane of the Lens 3 (Fig. 3.10a). Afterwards, a plano convex lens (40 mm) was used to collimate again and an image of the light source was finally focused at the aperture diaphragm with the focusing plano convex lens (60mm).

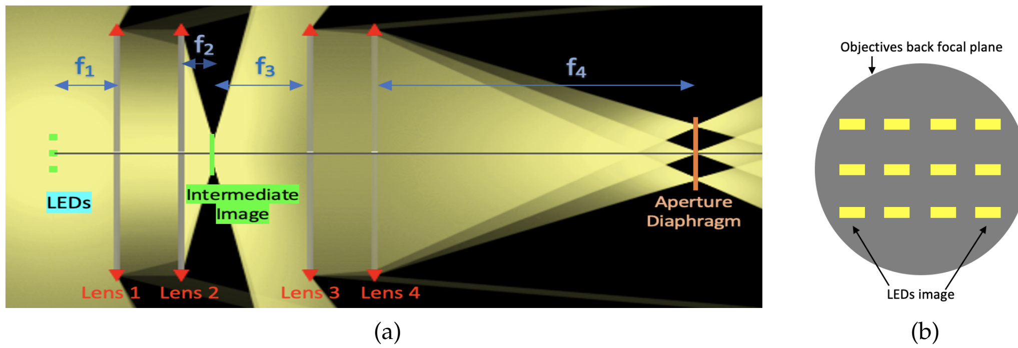

(a) (b)

Figure 3.10: (a) Configuration 4: Lens 1 is the aspheric condenser lens (17 mm), Lens 2 is the triplet collector lens (24 mm), Lens 3 is the plano convex lens (40 mm) and Lens 4 is the plano convex focusing lens (60 mm). The distances f_1, f_2, f_3 and f_4 correspond to the back focal lengths of the lenses. The image size of the light source is larger than the diameter of the aperture diaphragm and therefore only part of the light passes through the aperture. (b) LED matrix image at the back focal plane of the objectives in configuration 4. Only 12 out of 60 LEDs are visible.

The total magnification in this configuration is:

$$M_{source} = \frac{f_4}{f_3}\frac{f_2}{f_1} = \frac{60}{40}\frac{24}{17} = 2.12\ , \tag{3.2}$$

which is smaller than the magnification (Eq. 3.1) of the configuration 1.

The diameter of the triplet lens (24 mm) is about 30 mm, smaller than the other lenses. Therefore, some light was lost also in this configuration due to the smaller size of the lens and due to the addition of more optical elements along the path.

In all configurations presented above, attention was given to the external lenses and not to the internal plano convex lens (60 mm). This is because the internal plano convex lens (60 mm) is inside a proprietary optic holder and no lenses with the same diameter or even with the same focal length were available. Nevertheless, the aspheric lens (17 mm), instead of

the internal lens (60 mm), was purposefully placed close to the aperture diaphragm to focus the light collimated with the planar lens (40 mm) in order to have a magnification of less than 1. A smaller image was obtained, but the illumination was not satisfactory because the aspheric lens (17 mm) was a few mm larger than the space inside the microscope. These few mm were enough for the cover of the observation module of the microscope to touch the lens, causing it to shift away from the optical axis of the illumination system.

Among all the configurations, configurations 2 and 4 were two valid candidates for the setup of the wide-field MOKE microscope. Configuration 4 was selected because the image size of the LED matrix at the aperture diaphragm was smaller compared to the image size of the LED matrix in configuration 2. Moreover, in configuration 4 there were 12 LEDs at the back focal plane of the objectives (Fig. 3.10b) and there was also enough space between lens 2 and 3 for a dichroic mirror to couple the laser for the laser-scanning MOKE.

The new optical part added to the illuminating system, inspired by configuration 4, to focus an image of the light source at the aperture plane is depicted in Fig. 3.11.

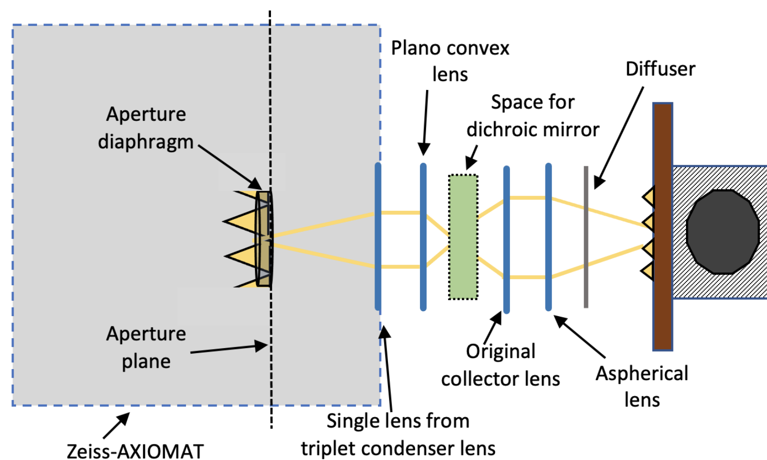

Figure 3.11: New lens system to focus a light image at the aperture plane. The lenses used are the same of the simulated configuration 4: Lens 1 is the aspheric condenser lens (17 mm), Lens 2 is the triplet collector lens (24 mm), Lens 3 is the plano convex lens (40 mm) and Lens 4 is the plano convex focusing lens (60 mm) from the triplet lens. Only part of the light passes through the aperture since the image size of the light source is larger than the diameter of the aperture diaphragm. Some space for the dichroic mirror for laser-scanning MOKE is indicated.

Considerations about LEDs matrix as a light source The high power LED matrix was chosen as a light source to illuminate the specimen with higher light intensity. However, only a small part of the light was available for the specimen illumination, since the image of the LED matrix at the aperture plane was bigger then the aperture diaphragm of the microscope.

In fact, the aperture diaphragm had a diameter of 10 mm while the LED matrix had a 20 mm side. Therefore, several trials were undertaken to reduce the size of the LED matrix but the image of the LED matrix at the aperture diaphragm always underwent a magnification. Therefore, it was not possible to have all the LED points inside a circle of 10 mm diameter. In addition, off-center light rays underwent greater refraction than central light rays along the light path (Fig. 3.10a and Fig. 3.12). This meant that part of the light beam was lost along the optical path. In the configurations, this light-loss effect played an important role because the size of the LED matrix was comparable to the diameter of the lenses and this effect was increasing with the increment of the distance between the lenses.

Moreover, the LEDs of the LED matrix are organized in row and column with free space between one LED point and the other. This means that the image of the LEDs of the LED matrix could not evenly fill the entire aperture diaphragm area. In configuration 4, these LEDs were better distributed than in configuration 2 and the images taken with the 25x and 50x had also an acceptable contrast. A diffuser [33] was added after the LED matrix to spread evenly the light coming from the LEDs in order to reduce the amount of glare that could be produced onto reflective specimens surface (Fig. 3.11).

Another factor that affected light loss was *etendue*, which refers to how the generated light is spread out in terms of area and angle. For LEDs, the entendue E is determined by the solid angle of the emitted light beam and the area of the light-emitting chip [34]:

$$\mathrm{E} = \pi n^2 A \sin^2 \theta. \tag{3.3}$$

Where n is the refractive index, A is the area of the light source and θ is the solid angle of light cone emitting from the source. The larger etendue is, the less light produced by the LEDs can be guided into the microscope objective (Fig. 3.12).

To understand how the illumination system is influenced by the size and the angle of light emission of the source, it is possible to make an approximate calculation of how much light from the source is actually transmitted into the objective lens. Taking a lossless system into account, then the ratio of the usable portion of the emitted light to the total emission of the LEDs gives the maximum possible efficiency for that system. If the setup of the Zeiss-AXIOMAT is considered a lossless system, the maximum efficiency is given by the ratio between the LEDs total output and the output that the microscope objectives can accept. Therefore, using the Eq. 3.3 in one dimension, it is possible to derive the maximum efficiency

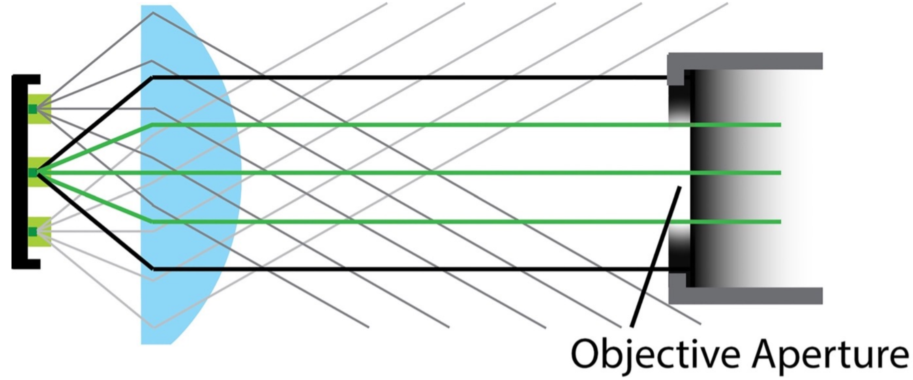

Figure 3.12: Efficiency of light projection is dependent on the LEDs etendue [34]. A lens is used to collimate the light from a LED with multiple emitters (green squares). While light from the central emitter (green rays) is projected onto the objective back aperture, light from off-center LEDs does not reach the aperture (grey rays). Moreover, the off-centered beam angles produce a wider beam, which also cannot be directed into the objective aperture (black rays).

[34]:

$$\text{Efficiency}_{max} = \frac{\pi n^2 A \sin^2 \theta_{usable}}{\pi n^2 A \sin^2 \theta_{total}} \tag{3.4}$$

Where θ_{usable} is the half-angle of usable light and θ_{total} is the half-angle of total light emitted by the light source. The LED matrix generates light with an output beam angle of 120°. To derive θ_{usable} the optical invariant is used. Applying the optical invariant to the system in

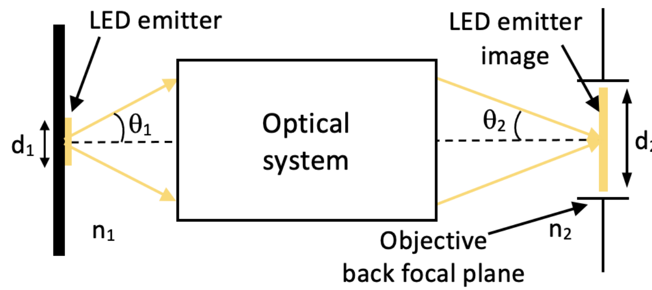

Figure 3.13: An illustration of the basic optical invariant (adapted from [35]). d_1 and d_2 are heights of object and image. θ_1 and θ_1 are aperture angles in object and image spaces. n_1 and n_2 are indices of refraction in object and image spaces.

Fig. 3.13, which can be used to represent the Zeiss-AXIOMAT setup, and using the LED matrix as the object and the back focal plane of the objective as the image, then the general equation of the optical invariant in the air ($n = 1$) becomes:

$$d_1 \sin \theta_1 = d_2 \sin \theta_2 \tag{3.5}$$

Where θ_1 is the half-angle of the total output beam of the LEDs and θ_2 is the half-angle of

the accepted illumination light from the objective, d_1 is the size of the LEDs chip and d_2 is the diameter of the back aperture of the objective lens. The objective lens on a standard compound microscope (depending on the manufacturer) can accept illumination light with a half-angle, θ_2, of 3.5°-5°. Light exceeding this half-angle will not pass through the objective lens, or if it passes, it may increase background light and reduce contrast. The size of the beam is limited by the back aperture of the objective lens, which is hardly larger than 10 mm. Assuming $\theta_2 = 5°$ and using $d_1 = 20\,\text{mm}$, $d_2 = 10\,\text{mm}$ inside Eq. 3.5 θ_1 can be derived:

$$\theta_1 = \arcsin \frac{d_2 \sin \theta_2}{d_1} = 2.5°. \tag{3.6}$$

Thus, the two parameters of the microscope θ_2 and d_2, limit the usable light which is diverging from the light source with an angle less than 2.5°. This means that given the output beam angle of 120° of the LEDs matrix, the maximum efficiency of the illuminating system is (from Eq. 3.4):

$$\text{Efficiency}_{max} = \frac{\sin^2 \theta_1}{\sin^2 \theta_{total}} = \frac{\sin^2 2.5°}{\sin^2 60°} = 0.003. \tag{3.7}$$

Thus, the 20 mm LED matrix with 120° beam angle would transmits only 0.3% of its light into the objective. Instead of a LED matrix of 20 mm length, having a LED matrix of 2 mm length, which means that the objective could collect rays diverging from the LED with angles less than 26°, would employ an efficiency of 51%. If more light needs to be transmitted, then it is required a smaller light source or a smaller output beam angle of the LED matrix in order to increase the efficiency.

Dust and ambient light

Dust and ambient light had also an important role on the quality of the domain images. To deal with these issues, some of the optical components of the microscope were wiped without deep cleaning, because there were other tasks to be accomplished (such as installing motors and encoders inside the microscope and setting up the laser-scanning MOKE). To reduce all the noise coming from the ambient light, the whole camera system was covered with aluminum paper. This improved the overall quality of the images taken by the CCD camera.

3.2.2 Addition of a camera system to visualize domain images

The sections above described how the light source was improved during the setup of the Zeiss-AXIOMAT as a wide-field MOKE microscope, working on LEDs degradation, achieving Köhler illumination and controlling the disturbance due to dust and ambient light. This section describes the process of adding a camera system to visualize domain images.

For the observation of magnetic domains, the camera system is almost as important as the objective lens in determining the performance of a magneto-optical microscope. It gives a significant contribution to the signal-to-noise ratio (SNR), but also determines the achievable spatial resolution. Digital high resolution cameras with high dynamic range monochrome and a bit depth of 12 or 16 bits are the most suitable for magneto-optical imaging [17].

In this project, a "PCO.PIXELFLY USB digital 14-bit CCD" camera [36] was employed to image magnetic domains. The acronym CCD stands for “charge-coupled device” and it is a technology used for the architecture of the image sensor.

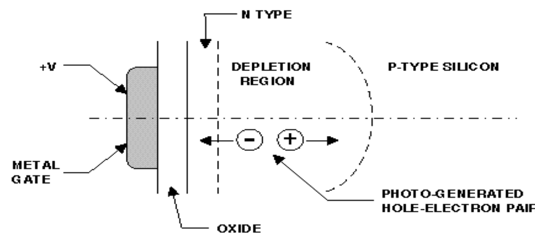

Figure 3.14: MOS capacitor [37].

The basis for the charge-coupled device in the image sensor is the MOS (Metal-Oxide-Semiconductor) structure. The simplest of all MOS structures is the MOS capacitor (Fig. 3.14). When a photon strikes the pixel, it is absorbed in the depletion region of MOS capacitor, and due to the photoelectric effect, an electron-hole pair is created with a conversion efficiency QE. The quantum efficiency (QE) is defined as the fraction of absorbed photons which contributes to the generation of the electron-hole pair. These pairs are then separated by the electric field of the biased MOS structure and the amount of charge accumulated is proportional to the optical radiation absorbed in its depletion area. The reading is made serially by carrying the charge on a unique output where an amplifier convert the charge into a voltage.

There are several parameters that describe the performance of a digital camera:

- Number of pixel of the sensor.
- Pixel size, i.e. the effective dimension of a single pixel.

- Effective sensitive area, given by: Number of pixel · Pixel size.
- Full well capacity, i.e. the maximum amount of charge that each pixel can store before saturation.
- Dynamic range, which represents the ratio between maximum output signal (full well capacity) and the noise floor of the camera. The dynamic range characterizes the ability of a device to capture in one image both the brightest and darkest areas of a scene. It is usually expressed in decibel.
- Dynamic range A/D, i.e. digital output bit depth, which represents the number of bit of the Analog-to-Digital Converter. The full well capacity divided by the bit depth determines the limit of precision for each gray level after the quantization.
- Readout noise, which describes all the sources of noise associated with converting the photoelectrons in a pixel to a digital number.
- Frame rate, number of frames per second.
- Quantum efficiency, which is a wavelength dependent fraction of photons converted into photo electrons.

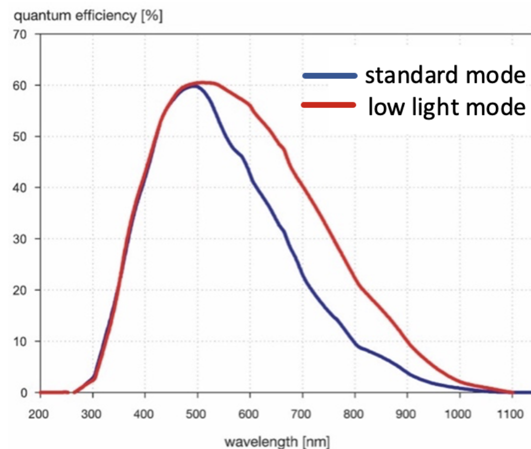

Figure 3.15: Quantum efficiency curves of the pco.pixelfly with two operation modes [36].

Fig. 3.15 shows some features of the CCD camera used in this project. The CCD camera is particularly suited for the blue LED matrix used in the wide-field MOKE microscope at the beginning since the quantum efficiency of the CCD camera, in the standard mode, for a wavelength $\lambda = 470\,\mathrm{nm}$ is almost the maximum available as shown in Fig. 3.15.

The following subsections describe the influence of the CCD camera on the spatial resolution of the wide-field MOKE microscope, the optical path employed to bring the reflected light

from the specimens to the camera sensor, and the software to control the camera.

Spatial resolution

The image sensor of a digital camera contains a large number of small pixels that collect photons. The final resolution of the image sensor is a function of the number of pixels and their size relative to the image projected onto the surface of the imaging array by the microscope optical system. The number of pixels in a digital image is known as the spatial density and the distance between each pixel is known as the sampling interval. Images with higher spatial resolution have more pixels within the same physical dimensions than those with lower spatial resolution.

Optical image details seen in the microscope that are smaller than the digital sampling interval (have a high spatial frequency) will not be correctly represented in the digital image. This means that when the optical resolution of the microscope is better than the spatial density, the spatial resolution of the resulting digital image is only limited by the spatial density. In order to maintain the spatial resolution of the objective lens in the resulting magneto-optical image, the Nyquist criterion must be satisfied. This criterion states that the sampling interval of the sensor has to be at least twice the highest specimen spatial frequency. Therefore, to capture the smallest feature present in a specimen, the sampling rate must be sufficient to collect two samples for each feature. This ensures that the intensity of the feature is retained in the imaging device.

From Eq. 2.7, the theoretical maximum optical resolution of the microscope for the objectives 25x and 50x can be derived:

$$R_{25x} = 0.61 \frac{\lambda}{NA_{25x}} = 0.44\,\mu\text{m}, \tag{3.8}$$

$$R_{50x} = 0.61 \frac{\lambda}{NA_{50x}} = 0.30\,\mu\text{m}. \tag{3.9}$$

Where $\lambda = 470\,\text{nm}$, R_{25x} is the optical resolution with the objective 25x given its numerical aperture $NA_{25x} = 0.65$ and R_{50x} is the resolution with the objective 50x given $NA_{50x} = 0.95$.

The image size I_{25x} of the distance R_{25x} projected onto the surface of the CCD sensor is given by the optical resolution R_{25x} multiplied by the objective magnification 25x:

$$I_{25x} = R_{25x} \cdot 25 = 11\,\mu\text{m}\ . \tag{3.10}$$

In this case, according to the Nyquist criterion to match the the optical resolution of the microscope and the spatial resolution of the digital image, a camera sensor having pixel size of 6.5 µm would be required. Instead, for the 50x objective a pixel size of 7.55 µm would be required.

The pixel size of the CCD camera is 6.45 µm [36]. Therefore, the optical limitation of the microscope and the limitation of the spatial density of the camera sensor in the spatial resolution of the resulting digital image are comparable. With the pixel size of 6.45 µm, the minimum distance distinguishable in the digital image would be 0.52 µm for the objective 25x and 0.26 µm for the 50x.

Optical path for the camera system

To assemble the components needed to focus an image of the specimen on the sensor, an optical breadboard was employed. The breadboard was adapted according for this setup and placed upon the observation module of the microscope. A mirror [38] was added to turn the

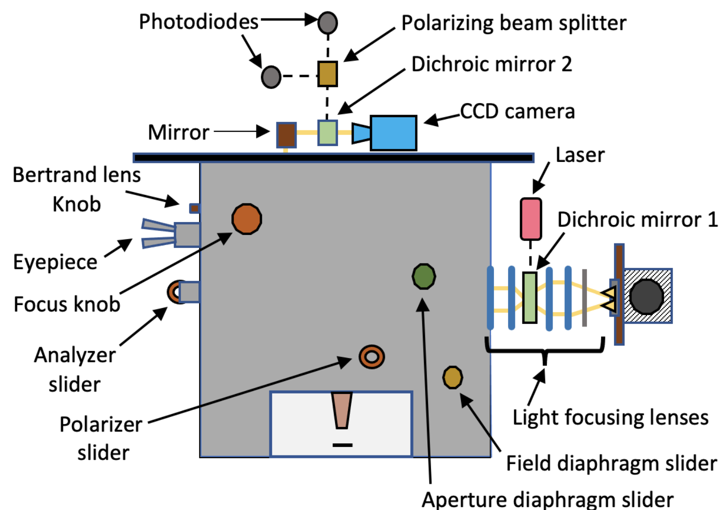

Figure 3.16: Zeiss-AXIOMAT after addition of the CCD camera. Space for the optical components (i.e., dichroic mirrors and photodioes) for the laser-scanning MOKE is also shown.

light beam coming out vertically from the observation module into a horizontal one. First, the microscope was set up for a correct visualization of the specimen through the eyepiece (see Section 3.2.3) and then the camera was positioned at a point where an image of the specimen was in focus. This point belongs to a plane of the set of image planes. There are about 41 mm between the mirror and the camera, enough to place a dichroic mirror for the laser-scanning

MOKE (Fig. 3.16).

During the entire design and setup of the wide-field MOKE microscope, the laser-scanning MOKE was also taken into account when designing the optical path for the camera. In fact, the optical path was designed in such a way that the optical elements for both LMOKE and WMOKE could be positioned. For instance, enough space was kept for the dichroic mirrors 1 and 2 used to couple the laser beam and to send the reflected beam towards the photodiodes (Fig. 3.16).

Software to control PCO camera

To acquire the domain images during the setup of the wide-field MOKE microscope, the software PCO.CAMWARE [39] was employed. With this software, it is possible to adjust all settings of the camera such as the exposure time. The option CONVERT CONTROL belonging to the camera properties was employed to manipulate the contrast of the domain images. Moreover, this software contains packages to use the PCO camera within the MATLAB and LabView environments.

3.2.3 Adjustment of optical system

After having improved the light source and added a camera system for the visualization of the domain images, this section introduces the adjustments of optical components, such as aperture diagphram, polarizer and analyser for obtaining magnetic domain images with good contrast. In fact, the setup of the optical system determines the final contrast of the magnetic domain images. Contrast in microscopy can be defined as the change in the intensity of a specific feature of the specimen relative to the background intensity or the surrounding features. Contrast is not an inherent property of the specimen but depends on the interaction of the specimen with light and the ability of the optical system to distinguish specific types of contrast. In order to obtain the best contrast, the adjustment of parameters (e.g., polarizer and analyzer values) is very important. Since all settings depend on the specimen, they are not systematic. Therefore, the parameters of the microscope must be used together with the parameters available in the software used to acquire the image each time.

The settings of the polarizer and analyzer are particularly important to achieve the best conditions to observe the Kerr effect. Therefore, the polarizer and analyzer should be in an

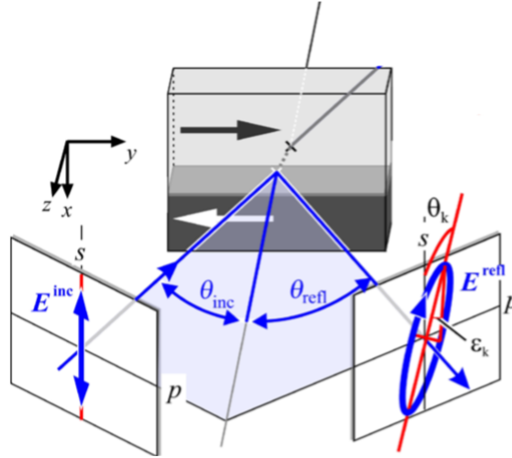

Figure 3.17: Reflection of a s polarized wave from a magnetic specimen (adapted from [17]).

extinction configuration to extinguish the light emitted from the first type of domain, which will appear completely black, while the second type of domains will appear more or less bright. If there is no extinction, it is difficult to distinguish domains because they will be all gray. In the following, an approximation of the light intensity captured by the CCD camera will be derived. This approximation contains information about the Kerr rotation. In doing so, two types of linear polarization are considered: s-polarized light and p-polarized light. Perpendicular (s) polarization is a linear polarization where the electric field is perpendicular to the plane of incidence, while parallel (p) polarization is the polarization where the electric field is parallel to the plane of incidence.

Let's consider a polar or longitudinal configuration and a linear s-polarized light reflected from a specimen surface. If the specimen is nonmagnetic, the reflected light will be only s-polarized. If the specimen is ferromagnetic then the reflection light generally consist of a p component, introduced by the magneto-optical Kerr effect, in addition to the dominant s component (Fig. 3.17). To measure the p component, the analyzer is set at a small angle from extinction [40, 41].

The two orthogonal components in the reflected light are:

$$\mathbf{E}^r = r_{ps}\mathbf{E}_s^i + r_{ss}\mathbf{E}_s^i = \mathbf{E}_s^r + \mathbf{E}_p^r. \tag{3.11}$$

Where $\mathbf{E}_{p,s}^r$ and $\mathbf{E}_{p,s}^r$ are the vectors of the incident and reflected light, respectively. The ratios $\frac{\mathbf{E}_p^r}{\mathbf{E}_s^i} = r_{ps}$ and $\frac{\mathbf{E}_s^r}{\mathbf{E}_s^i} = r_{ss}$ are reflection coefficients that define the p-polarized and s-polarized components after the reflection, respectively. While the ratio between the two components of

the reflected light, which is equal to the ratio of their associate reflection coefficient, gives the complex Kerr angle $\phi_{k,s}$ [17]:

$$\frac{\mathbf{E}_p^r}{\mathbf{E}_s^r} = \frac{r_{ps}}{r_{ss}} = \theta_{k,s} + i\epsilon_{k,s} = \phi_{k,s}. \tag{3.12}$$

Where $\theta_{k,s}$ and $\epsilon_{k,s}$ represents the Kerr rotation[2]and the Kerr ellipticity[2] (Fig. 3.17) for the s-polarized wave, respectively.

Having a p-polarized incidence light then the equation 3.12 for a p-polarized becomes:

$$\frac{\mathbf{E}_s^r}{\mathbf{E}_p^r} = \frac{r_{sp}}{r_{pp}} = \theta_{k,p} + i\epsilon_{k,p} = \phi_{k,p} \tag{3.13}$$

where r_{sp} is the reflection coefficient that defines the s-polarized component after the reflection.

When the analyzer is set at a small angle from extinction (Fig. 3.18), the intensity measured by the photodetector is [41]:

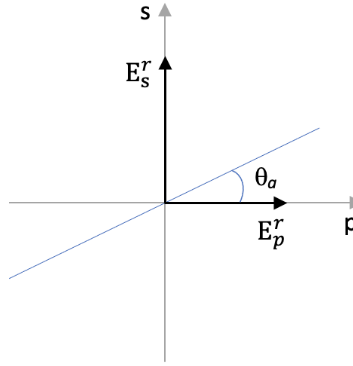

Figure 3.18: Analyzer at a small angle from extinction.

$$I \propto \left|\mathbf{E}_p^r \cos\theta_a + \mathbf{E}_s^r \sin\theta_a\right|^2 \approx \left|\mathbf{E}_s^r\theta_a + \mathbf{E}_p^r\right|^2 = \left|\mathbf{E}_s^r\right|^2 \left|\theta_a + \frac{\mathbf{E}_p^r}{\mathbf{E}_s^r}\right|^2 \tag{3.14}$$

Substituting $\frac{E_p^r}{E_s^r}$ from Eq. 3.12 into the Eq. 3.14, Eq. 3.15 is obtained:

$$I \propto \left|\mathbf{E}_s^r\right|^2 \left|\theta_a + \theta_k + i\epsilon_k\right|^2 \approx \left|\mathbf{E}_s^r\right|^2 \left(\theta_a^2 + 2\theta_a\theta_k\right). \tag{3.15}$$

Where both θ_k and ϵ_k are, in first approximation, linearly proportional to the magnetization. Thus also the measured intensity will be proportional to the magnetization.

The microscope Zeiss-AXIOMAT is already equipped with a polarizer and an analyzer and

[2]They are the same that were presented in Section 2.2.2.

in Fig. 3.16 the sliders used to set their value is shown. During the measurement, they can be set for a maximum extinction, e.g. polarizer at 0° and analyzer at 86°.

Achievement of higher levels of Kerr sensitivity

The advantage of using a Kerr microscope is that it is possible to select the MOKE effect (i.e., Longitudinal, transverse or polar) to be measured adjusting of the optical system. For the setup of the wide-field MOKE microscope, the polar MOKE was required. Moreover, it was possible to increase the sensitivity of the microscope to get a higher polar Kerr intensity setting the the analyzer and polarizer.

Section 2.2.2 described that to detect different magnetization components, different angles of incidence need to be provided. Therefore, it is important to select the angle of incidence of the light on the specimen. The condensered aperture diaphragm is responsible for the incident angle of light on the specimen (see Section 2.1). With this diaphragm, a slit allowing the selection of the incidence angle is required.

Illuminating a magnetic specimen with a s-polarized wave in the reflected light, there will be two orthogonal components: one polarized in the same s-direction with a reflection coefficient r_{ss} and the other p-component polarized orthogonally with a reflection coefficients r_{ps}. In most cases of magneto-optical imaging, the individual Kerr intensities are the relevant quantities and for the polar Kerr effect (also for longitudinal) the reflective intensities $|r_{ps}|^2$ or $|r_{sp}|^2$ are the figures of merit for the reflected light polarization variation in relation to the incident light [17]. Figure 3.19 shows the dependency of the polar and longitudinal reflection coefficients.

Fig. 3.19a shows that starting from a small incident angle, the polar Kerr intensity is very high and hardly changes in a wide angle range. The significant drop in $|r_{ps}|^2$ only occurs when the NA value is high. Instead, Fig. 3.19b shows that the longitudinal Kerr effect is very low for a small incident angle and it increases for high NA. Moreover, with the use of oil immersion objectives, the maximum Kerr intensity increases significantly. Oil immersion objective lens simplifies the magneto-optical imaging of magnetic domains in reflection.

The low angle of incidence for the polar component of the magnetization can be selected by taking the central portion of the light beam as in Fig. 3.20.a. Instead, the longitudinal component requires wider angle of incidence that can be selected with an off-centered slit, (Fig. 3.20b and Fig. 3.20c). In Fig. 3.20b, the polarization axis is perpendicular to the incidence

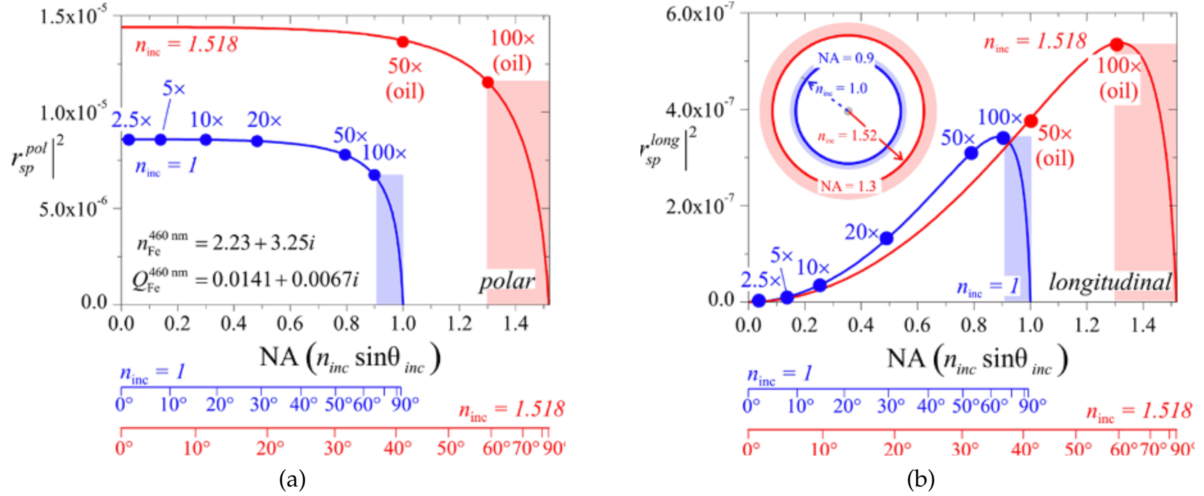

Figure 3.19: Change of Kerr intensity with numerical aperture NA for air (n_{inc} = 1) and oil immersion (n_{inc} = 1.518) objective lenses [17]. Typical values of NA for individual objective lenses of different magnification are indicated. (a) Polar Kerr Intensity. (b) Longitudinal Kerr Intensity.

plane X (formed by x and z axis), thus the incident light is s-polarized. Whereas, in Fig. 3.20c the polarization axis is parallel to the incidence plane Y (formed by y and z axis), thus the incident light is p-polarized.

In order to position the slit correctly, the image of the condenser aperture plane needs to be considered. As seen in Section 2.1.3, the aperture plane and the back focal plane of the objective belong to the same set of conjugate image plane. Therefore, the condenser aperture can be imaged by simply looking at the back focal plane by means of a Bertrand lens. In fact, a Bertrand lens projects an interference pattern formed at the objective back focal plane into focus at the microscope image plane. The image formed by the Bertrand lens is called conoscopic image and the characteristic of this image is that the distance of a point from the optical axis is a monotonous function of the inclination angle of the light beam [41]. When the polarizer and analyzer are crossed for maximum extinction, the image should appear uniformly dark. Instead, the conoscopic image of the optical microscope shows a cross-shaped extinction pattern (Fig. 3.20). An axial beam can be considered as being composed of individual rays that travel through lens surfaces each under a different plane and angle of incidence. All the rays not lying in a central incidence plane when are reflected will show a higher phase difference between the two components than the rays lying in the center of the pupil [40]. This means that all beams that are not in the central incident plane along or perpendicular to the polarization plane are reflected more strongly in an elliptical

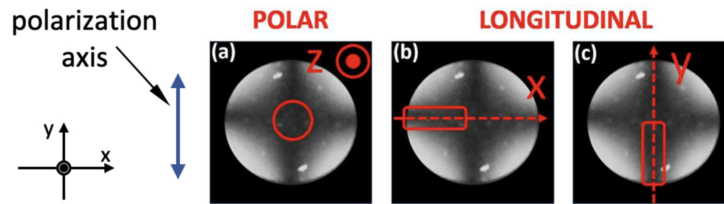

Figure 3.20: Representation of the cross-shaped extinction pattern and of the slit position for the different component of the magnetization (adapted from [41]). The polarization axis (↕) is kept vertical for all cases. The effective plane of incidence (Z, X, Y) are indicated. (b) Longitudinal with s-polarized incident light. (c) Longitudinal with p-polarized light.

and rotated polarization state in general and cannot be extinguished by the analyzer [41].

Looking at the conoscopic image, the slit should be moved in order to be placed correctly within the extinction pattern to maximize the magneto-optical contrast. Ideally, the slit should be placed inside the extinction pattern to ensure that the selected beam has a well-defined polarization set by the polarizer. Whereas, if the slit is opened beyond the extinction pattern, the amount of incident light will increase and the polarization state of the reflected light in the conoscopic image will give no magneto-optic contrast, leading to an increment of the background illumination of the imaging system.

The microscope Zeiss-AXIOMAT is equipped with an aperture diaphragm slider, which contains an aperture diaphragm and two centering screws (Fig. 3.16). It is possible to adjust the size of the aperture iris diaphragm by turning the knurled knob on the aperture slider and position the slit (the iris diaphragm) with the centering screws in one of the desired position as in Fig. 3.20.

Configurations to Focus Specimen Image into Eyepiece

After having installed and positioned the light source in the right way, obtaining Köhler illumination (as seen in Section 3.2.1), it is possible to proceed with the visualization of the specimen into the eyepiece. In the following, the Fig. 3.21 will be taken as a reference to describe the steps needed to obtain a sharp image of the specimen into focus inside the eyepiece and then on the CCD camera.

I. Set the LED driver at maximum power and direct the light flux into the eyepiece using the optical path 20.1 (Fig. 3.4). Set zoom 1 using the knob for the zoom OPTOVAR.
II. Place the specimen on the stage and swing in the objective. The specimen must be adjusted exactly at the right angles to the optical axis. Otherwise even slight deviations in

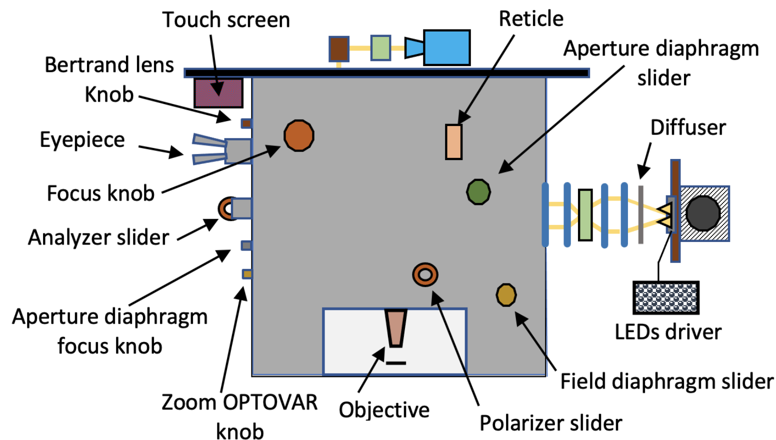

Figure 3.21: Adjustment of optical components of Zeiss-AXIOMAT for focusing an image of the specimen into eyepiece or on the CCD camera.

the adjustment decreases the sharpness in the image with high magnification objectives.

III. Insert the reticle and focus the eyepiece on its rectangular shape and turn the eyepiece tubes clockwise until the crosslines appear sharp.

IV. Look into the eyepiece and find the specimen image moving the objective with the buttons Up and Dn on the touch screen (see Section 3.2.4) and focus.

V. Center and focus the field diaphragm:

   i. Close the field diaphragm slit, using the field diaphragm slider, until its edge becomes visible in the field of view.

   ii. Center the field slit image in the eyepiece with the centering screw on the slider. Once centered, open the slit turning again the knurled disk until its edge just disappears behind the field of view edge.

VI. Swing in the Bertrand lens: for the following steps it is required a mirror-like specimen.

   i. Swing in the Bertrand lens using the Betrand lens knob.

   ii. Looking into the eyepiece an image of back focal plane of the objectives will be visible. In the same image an image of the aperture diaphragm and of the LEDs (provided that the diffuser has been removed) will be in focus, since they belong to the same set of conjugate focal planes. Most probably, these images are not sharp and not centered. Then, proceed with the next step, i.e. center the aperture diaphragm.

VII. Center the aperture diaphragm:

i. Swing in the Bertrand lens and looking into the eyepiece, close the aperture diaphragm using the aperture slider until the edge of the diaphragm becomes visible at the back focal plane. If the edge is not in focus, then use the aperture focus knob to get a sharp image of the edge.
ii. Center the the edge of the slit with regard to the back focal plane with the centering screw on the aperture slider. Set the aperture diagram so that its image corresponds to about 2/3 or 3/4 of the diameter of the objective back focal plane.

If the light source is not centered or the LEDs are not in focus at the back focal plane of the objectives, it is possible to look at the back focal plane via eyepiece or via Tube 2 (Fig. 3.4) directing the light toward them. For a better adjustment of the LED matrix, tube 2 (without eyepiece) should be used. Since the LED matrix can be moved only backward and forward, the LEDs image can be adjusted only by bringing it into focus at the back focal plane. Therefore, to focus the image, it is possible to look via eyepiece at the back focal plane using the Bertrand lens. The steps for focusing an image of LEDs at the back focal plane of the objectives are described below:

I. Reduce the LEDs intensity with the potentiometer of the LEDs driver.
II. Remove the diffuser from the light source.
III. Move the light source backward and forward until you see a sharp image of the LEDs at the back focal plane.

Once all the adjustment have been done, swing out the Bertrand lens to bring back an image of the specimen into the eyepiece. At this point for the imaging of the magnetic domains with the CCD camera, an alternative optical path (e.g., optical path 19.1 in the Fig. 3.4) should be chosen in order to direct the reflected light beam toward the CCD camera sensor. Thus, domain images with high contrast are obtained using the camera software and adjusting the analyzer and the aperture, in order to increase Kerr sensitivity.

3.2.4 Obtainment of better objectives control through a positioning system

The sections above described the improvement of the light source, the addition of a camera to visualize domain images and the adjustement of the optical system during the setup of the Zeiss-AXIOMAT as wide-field MOKE microscope. This section describes how a better objectives control was obtained through a control system.

The Zeiss-AXIOMAT comes with a control unit to handle the position of the objectives relative to the specimen. To focus on the specimen, a joystick could be moved on the control unit to position the objectives. Moreover, if a fine focus was needed, it was also possible to move the objectives further with the focus knob. During the development of the wide-field MOKE microscope, a more accurate and functional mechanism of controlling the objectives was implemented. In particular, a positioning system with a graphical user interface for a better control of the objectives was developed (Fig. 3.22). This positioning system employed a microcontroller, a display, a stepper motor and an encoder to control the objectives.

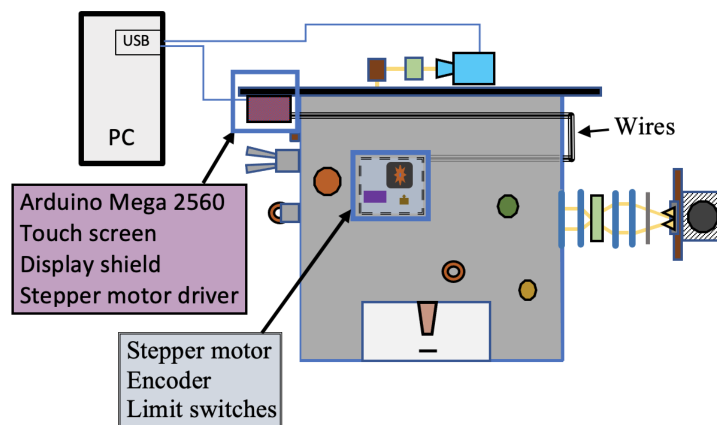

Figure 3.22: Positioning system with graphical user interface (GUI) developed for Zeiss-AXIOMAT. A housing, containing the touch screen and some other components, is installed outside the microscope to allow the objective control. Some other components are inside the microscope such as the motor, the encoder and the limit switches.

As a microcontroller, Arduino Mega 2560 [42] was selected since it was suitable for this project. In fact, it has a high number of input/output pins, 6 interrupt pins and several libraries for display and motors. Moreover, it was available with different components useful for prototyping. For instance, cables, breadboard, external power supply, motor, motor driver, rotary encoder and so on. Arduino Mega was employed to control a touch display, a stepper motor driver and a magnetic encoder.

With this new system (Arduino, display, stepper motor and encoder), it is possible to move the objectives at two different speeds and save preference positions for each objective in order to reach them later. For example, one of these positions could be the one where the specimen is in focus with a certain objective. Thus, it is possible to save this position and then to tell the objective, after having moved it elsewhere, to re-position itself in the saved position. During the measurements, switches from one objective to another are frequent and the focus on the

specimen may change. Nevertheless, thanks to this function, it is easy to re-set the objectives on the pre-saved focus position, bringing the specimen again in focus. In the following, it is described how to pre-save a focus-position as well as control all the system components with a position control system (Arduino, display, stepper motor and encoder). In particular, the next sections will introduce the addition of a graphical user interface through a display, the replacement of the internal DC motor with a stepper motor and a driver, the adjustment of the limit switches, the addition of an encoder, and the programming functions employed in the position control of the objectives.

Addition of a graphical user interface through a display

In the initial configuration of Zeiss-AXIOMAT with the control unit, it was only possible to move the objective up and down, while after the addition of the display more options for the objective control are available. For instance, a menu is introduced (Fig. 3.23a), where it is possible to choose the options for controlling the objective (Fig. 3.23b). For each objective it is possible to save a desired position in order to reposition the objective in the saved position later by clicking on save and go button, respectively (Fig. 3.23b). There are two different speeds for focusing on the specimen: Up and Dn move the objectives up and down a small distance while Up+ and Dn+ move the objectives up and down a long distance. Up and Dn are slower, but more precise in positioning than Up+ and Dn+. When the buttons are held down until the desired position is reached, the objective moves accordingly according to the chosen speed and precision.

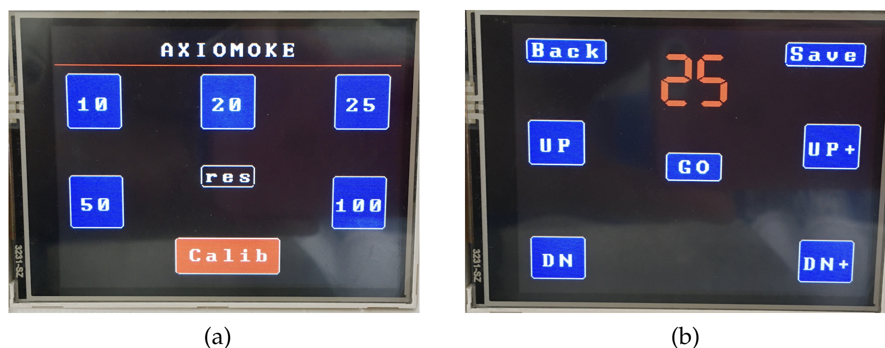

(a) (b)

Figure 3.23: Graphical user interface (GUI) of the positioning system. (a) Main menu. (b) Objective-25x menu.

In the Main menu (Fig. 3.23b) the option "Calib" stands for calibration. Calibration returns

the objectives to a default position and is used to reset the internal global counter, which is used to account for the position of the objectives. Calibration is necessary whenever the positioning of the objectives does not match the desired position. When the objectives is moved manually, while the microcontroller is switched off, it could be needed to calibrate if the encoder counter exceeds 2 mm counts.

The res (reset) button is needed to unlock the system whenever the limit switches give a wrong signal. Limit switches are used to limit the movement range of objectives so that they do not exceed the space available to them. Sometimes due to vibrations caused by the motor, the switches give wrong signals. If a objective is in a position where get any signals should not be generated from the switches then the res button can be employed to unlock the system.

The save button is used to save the position of the objective that is being used at that moment. The position is saved inside the EEPROM memory of the microcontroller.

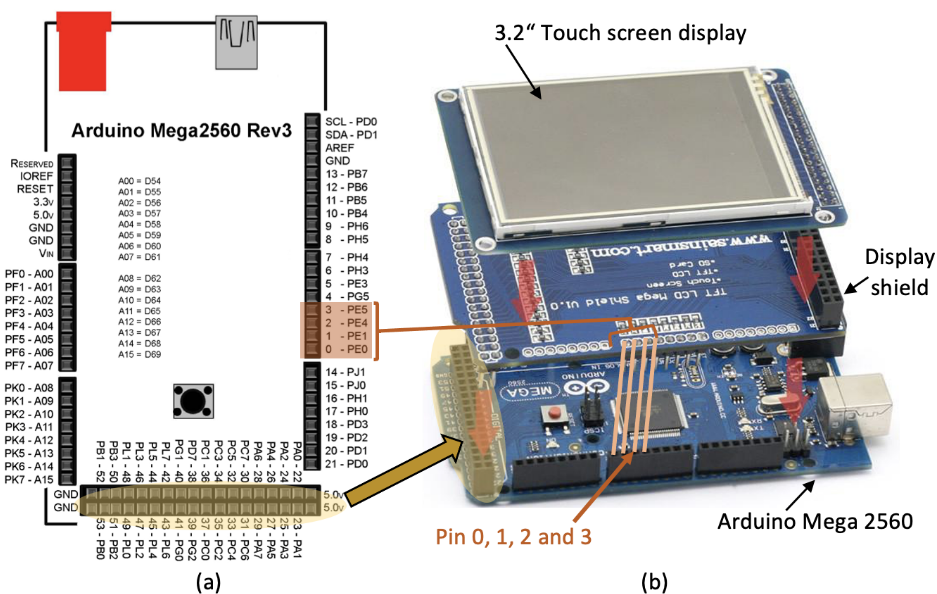

Figure 3.24: (a) Arduino Mega 2560 pinout. (b) The touch display, the shield and the Arduino are connected one on top of the other. The Arduino pins occupied the shield are shown (adapted from [43, 44]).

Concerning the display, a 3.2″ TFT touch screen [45] with a display shield [46] was employed. The display shield allows easy coupling of the display and Arduino Mega without the presence of cables around (Fig. 3.24).

To program the display, some external libraries were used such as UTFT and URTouch [43, 47] compatible with the Arduino Mega, the 3.2″ display and the display shield. To make them

work some parameters need to be set, depending on the display model and the shield (see the manuals in [43] [47]). The shield simplifies the assembly, but at the same time constrains the use of some Arduino pins predefined by the shield itself. The display shield occupied pins 0 and 1 (Fig. 3.24b), which are used by Arduino for serial communication with the computer and the shield connection often created a conflict by blocking the touch of display. Moreover, the shield occupied the interrupts pins 2 and 3 which were needed for other purposes in the development of the positioning system control. To overcome these issues, the shield has been modified by moving some of these pre-assigned pins to unused analog pins of Arduino. For instance, some shield pins of the group J19 were moved to the pin group J22 [48]. These modifications made it possible to use some analog pins (pins A3, A4 and A5) instead of digital pins (pins 2, 3 and 5). Thus, it was possible to free the digital pins 0 and 1 used for the serial communication and the interrupts pins 2 and 3 used for other purposes. This solution was adopted because analog pins were not occupied by the shield and analog pins can be used also as digital pins.

The Arduino pins are grouped by 8 and numbered from 0 to 7 (Fig. 3.24a). However, pins in the same group do not always belong to the same port. For instance, the digital pins going from 0 to 7 belong to different ports (Fig. 3.24a and Fig. 3.25). This fact has been taken into account during the relocation of the pins, because some functions of UTFT library use the direct port manipulation. Therefore, during the reallocation, the port number of a digital pin was paired with the port number of the analog pin, instead of using their pin numbers. An example is shown in Fig. 3.25, where the digital pin number 5, corresponding to the port number E3, is connected to pin A3 corresponding to port number F3. The pins were reallocated in the following way: pin 0 to A0, pin 1 to A1, pin 2 to A4, pin 3 to A5 and pin 5 to A3. The pins numbers underlined in Fig. 3.25 were not reallocated since they were not needed. In addition, moving only the necessary pins led to fewer twisted and cumbersome wires since the pins that had to be soldered together were diagonally opposite each other (Fig. A.1 in the Appendix).

PORT NUMBER	PF7	PF6	PF5	PF4	PF3	PF2	PF1	PF0
ANALOG PINS -->	A7	A6	A5	A4	A3	A2	A1	A0
DIGITAL PINS -->	0	1	2	3	4	5	6	7
PORT NUMBER	PE0	PE1	PE4	PE5	PG5	PE3	PH3	PH4

Figure 3.25: Display shield pin modification.

All these modifications were needed for plugging Arduino Mega, display and shield one on top of the other (Fig. 3.24). Doing so, two extra interrupts pins (2 and 3) were gained and the touch freezing issue (now pin 0 and 1 are disconnected from the shield) was solved. However, the Arduino was unplugged from the display and the shield because a different arrangement of these components were found while designing the housing, which contains all the electronic components (see Section 3.3). For the latter arrangement, there was no longer any need to change the digital pins. In fact, it was possible to choose different Arduino pins for the display shield and the shield pins could be connected to the selected Arduino pins through wires. For instance, if instead of the Arduino pin 2, the pin A4 is used (as before) to connected the shield pin 6, it is no longer necessary to modify the digital pins because it is possible simply to connect via wire pin 6 of the shield (pin 6 of the group J19 [48]) to the Arduino pin A4.

In addition to the pin change, there was another problem with the display. This problem was related to the fact that touch at the edges was not recognized well and sometimes pressing one button would activate another. To overcome this problem, the buttons have been spaced apart and the less used ones, such as the save and reset buttons, have been made smaller (Fig. 3.23). The display has also been recalibrated, obtaining new coordinates that have been added to the URTouchCD.h file (for further details on this procedure see the manual in [47]).

Replacement of the internal DC motor

In this section, the reasons behind the replacement of the DC with a stepper motor and a driver will be highlighted. Moreover, some basic concepts relating the DC motor, stepper motor and their drivers will be introduced for a better understanding of their functionalities.

A brief introduction to DC motor and its driver A DC (direct current) motor is an electromagnetic device that converts electrical energy into mechanical energy for rotation using the interaction of magnetic fields and conductors [49]. The motor components are designed in such a way that the interaction of the current and the magnetic field produces a continuous and regular rotary motion. There are many types of DC motors and the brushed DC motor (BDC) is the simplest of all motors and usually consists of the following parts (Fig. 3.26a):

Stator: a fixed part of the motor in which the rotor rotates. The stator generates a stationary magnetic field around the rotor.

Rotor: the rotating part of the motor and it is axially mounted in the center of the stator housing. The rotor is also called the armature and consists of one or more windings. When these windings are energized, they generate a magnetic field. The magnetic poles of the rotor magnetic field will be attracted by the opposite magnetic poles of the stator, producing a torque on the rotor and this make the rotor turn. As the motor rotates, the rotor coils (winding) are energized and de-energized in such way that the magnetic poles generated by the rotor are always opposed to the stator poles. This switching of the magnetic field in the rotor winding is called commutation [50].

Brushes and commutator: brushed DC motors do not require a controller to switch the current in the motor windings because this switching is done mechanically. A segmented copper sleeve, known as the commutator, is placed on the shaft of the BDC motor. As the motor turns, a series of electromechanical contacts, called brushes, runs over the commutator segments, allowing current to flow to the rotating motor windings in the correct sequence and direction. The commutator segments are attached to different rotor windings, so when a voltage is applied across the motor brushes, a current is generated, giving rise to a dynamic magnetic field within the motor.

The components of a motor are designed to ensure that the interaction of currents and magnetic fields provides a continuous and regular rotary motion. The equivalent electrical circuit of a DC motor is shown in Fig. 3.26b. In this type of motor, the windings regardless

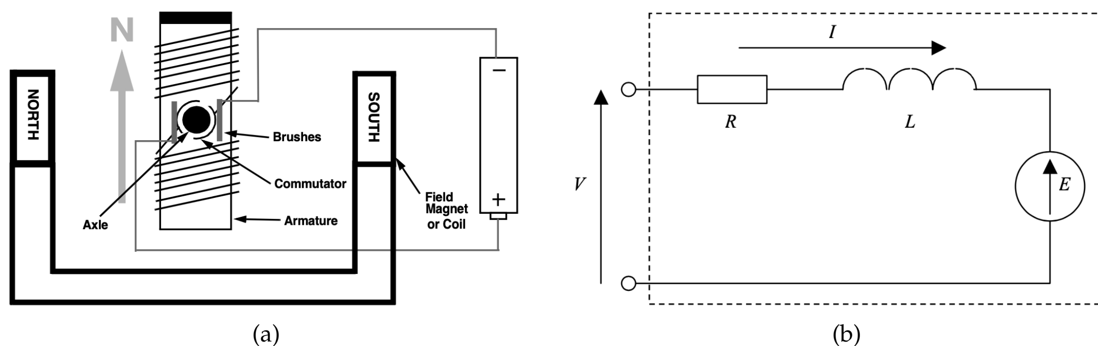

Figure 3.26: (a) Simple two-pole brushed DC motor [50]. (b) Equivalent electrical circuit of a DC motor [49].

of the number of their configurations can be considered as one large continuous winding. In the Fig. 3.26b the equivalent electrical circuit of a DC motor is shown. Where V is the voltage applied to the motor terminals, L and R are the inductance and resistance of the motor windings respectively and E is the motional electromotive force (e.m.f.) developed

internally through the motor windings. Motional e.m.f. arises as a consequence of the motor windings passing through magnetic flux generated by the stator windings. When the device is acting as a motor (rather than a generator), E always opposes V because the induced e.m.f. always acts to reduce the current in the loop and for this reason it is called Bemf (back e.m.f.).

The equation relating these terms is given by [51]:

$$V = E + I \cdot R + L\frac{dI}{dt} \tag{3.16}$$

and given a constant I, under a steady state condition, we get:

$$V = E + R \cdot I \quad \longrightarrow \quad I = \frac{V - E}{R}. \tag{3.17}$$

The term (R·I) represents the loss that occurs in the motor windings due to the their resistance. It is usually referred to as "copper loss" and causes a significant increase in temperature when the motor is running.

The speed and torque of the DC motor depend on the strength of the magnetic field generated in the rotor, which in turn depends on the current flowing in the motor windings. Therefore, by adjusting the rotor voltage (thus the current) the motor speed can be changed. The torque T, generated by the interaction between the magnetic field flux of the stator ϕ_f and the current in the windings I [51]:

$$T = k_t \cdot \phi_f \cdot I = K_T \cdot I. \tag{3.18}$$

Where K_T is the torque constant $\left[\frac{N \cdot m}{A}\right]$ of the motor. The BEMF (E) produced by the rotation of the rotor at a speed ω_m in the presence of the stator field ϕ_f is given by [51]:

$$E = k_e \cdot \phi_f \cdot \omega_m = K_E \cdot \omega_m. \tag{3.19}$$

Where K_E is the volatge constant $\left[\frac{V \cdot sec}{rad}\right]$ of the motor.

A typical torque vs speed curve of a DC motor is represented in Fig. 3.27. Where T_s is the starting (or stall) torque and it is the maximum torque the a motor can produce starting at zero speed. The speed ω_{max} is the maximum speed the motor can reach with no load. We can notice that the torsion decreases with increasing speed. This is due to the fact that BEMF increases with increasing speed (Eq. 3.19), which decreases the current in the windings (Eq. 3.17) and consequently the torque decreases (Eq. 3.18).

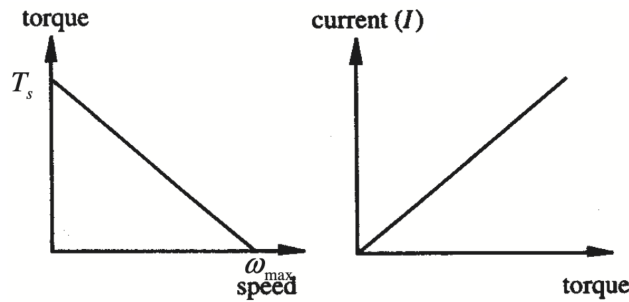

Figure 3.27: DC motor torque-speed curve [52].

The speed of DC motors can be controlled through a controller using pulse width modulation (PWM) to vary the voltage supply of the motor. The drive circuits allow the controllers to vary the current in the windings of the BDC motor, thus enabling control of the motor speed (Fig. 3.28).

DC motor drivers There are many driving methods for brushed DC motors. In cases where the motor only needs to turn in one direction, a High-Side or Low-Side drive circuit can be used (as reported in [50]). To drive the motor in two directions (forward and reverse), the direction of the motor current must be switched. This can be achieved by using four power transistors (Q_1 - Q_4) arranged in a configuration called H configuration (H-bridge), as shown in Fig. 3.28. Where the H-bridge can be seen as it is divided in two parts, or half-bridges. One

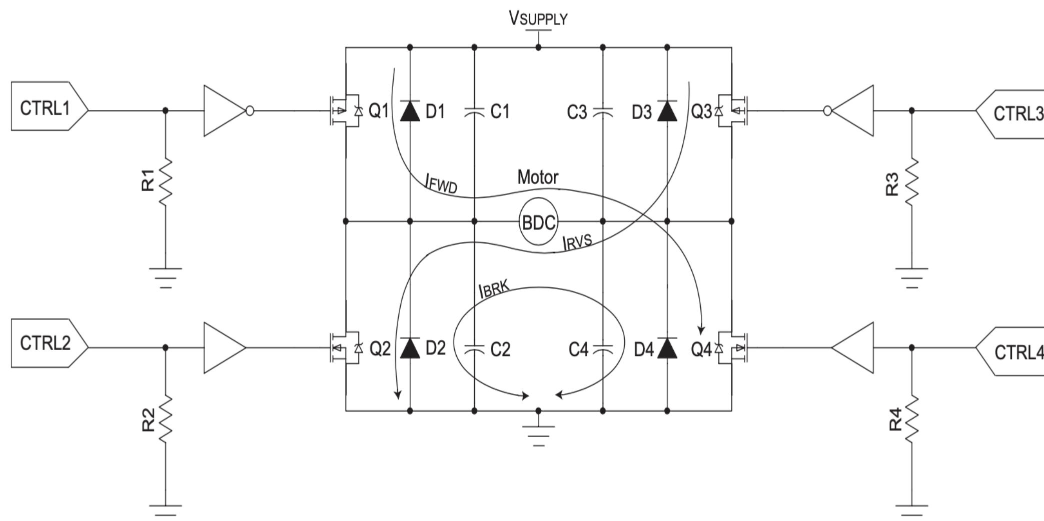

Figure 3.28: Bidirection BDC motor Drive (H-bridge) circuit [50].

half bridge is made up of transistors Q_1 and Q_2 while the other half-bridge is made up of

transistors Q_3 and Q_4 (Fig. 3.28). Each of these half bridges is capable of switching one side of the BDC motor to either V_{supply} or ground. For instance, when Q_1 is on and Q_2 is off, the left side of the motor will be at the potential of the supply voltage V_{supply}. And keeping Q_4 on and Q_3 off the opposite side of the motor will be grounded. The arrow of the forward current (I_{FWD}) shows the resulting current flow for this configuration. The diodes (D_1 - D_2) protect the MOSFETs from current spikes, generated by the BEMF, when the MOSFETs are switched off. For more details about the H-bridge driving circuit see [50].

A brief introduction to stepper motor and its driver Stepper motors, like DC motors, are powered by direct current, but do not use the brushes and mechanical commutators found in typical DC motors. Instead, they are a brushless DC motor whose stator contains many evenly spaced wire windings that act as magnetic poles when excited. While their rotor consists of a pair of gear-shaped permanent magnets. The motor's electronic controller switches the current to each successive coil of the stator to drive the rotor from pole to pole. These motors are called "stepper" motors because the controller controls which pole the rotor will jump to, thereby obtaining a precise, step-by-step rotational movement.

Stepper motors occupy a unique position in the field of motor control and are commonly used in measurement and control applications. There are three basic stepper motors types (Fig. 3.29): variable reluctance, permanent magnet and hybrid.

Variable reluctance (VR): consists of a soft iron multi-toothed rotor and a wound stator (Fig. 3.29a). When the stator windings are energized with DC current, its poles become magnetised and attract the rotor teeth, generating a rotation.

Permanent magnet (PM): these motors have a magnetised rotor with alternating north and south poles situated in a straight line parallel to the rotor shaft (Fig. 3.29b). In contrast to the VR motor, the PM motor does not have a toothed rotor.

Hybrid motors: these motors combine features of both permanent magnet and variable reluctance motor technology (Fig. 3.29c). The hybrid stepper motor, compared to other two types of motor, provides better performance in terms of step resolution, torque and speed. The rotor is multi-toothed in the same way as the VR motor and holds an axially magnetized magnet around its shaft. The teeth on the rotor ensure an enhanced path that allows the magnetic flux to be guided to the preferred positions in the airgap. This leads to a further improvement in the stopping, holding and dynamic torque characteristics of the

motor compared to the VR and PM types.

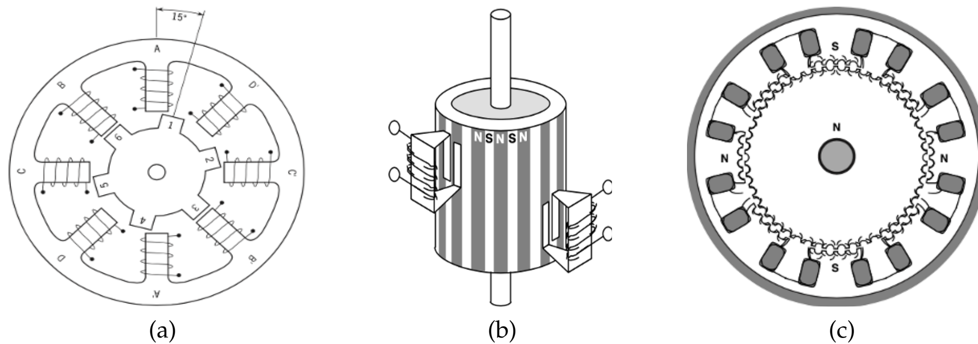

Figure 3.29: Different types of stepper motors (adapted from [53]). (a) Cross-section of a variable reluctance motor. (b) Permanent magnet stepper motor. (c) Cross-section of a hybrid stepper motor.

The stator of the stepping motor holds multiple windings. Depending on the type of winding, stepper motors can be divided into two groups: bipolar stepper motors and unipolar stepper motors (Fig. 3.30).

Unipolar: this type of stepper motor consists of two windings, each winding has a center tap (Fig. 3.30a). The central taps are either connected to each other or kept separate, thus a unipolar motor can have 5 or 6 wires. All unipolar motors are driven in the same way i.e., the center tap wire is connected to the power source, and the ends of the winding are alternately grounded.

Bipolar: this type of stepper motor consists of two windings and has four 4 wires. It has no central tap and therefore the current flows through a whole winding at a time instead of only half the winding as in the case of the unipolar stepper motor (Fig. 3.30b). As a consequence, bipolar motors produce more torque than unipolar motors of the same size. However, bipolar motors require a more complex control circuit than unipolar motors. In a bipolar motor the current flow in the winding is bidirectional. This means that the polarity of each end of the winding has to be changed.

The windings of a stepper mode are organized into groups called *phases*. When each phase is energized in sequence, the motor rotates one step at a time. Generally, stepper motors have two phases and a bipolar motor with two phases has one winding per phase and a unipolar motor has one winding (with a center tap) per phase.

Before for the DC motor, the control circuit named H-bridge was presented and it is used also for a bipolar motor to change the polarity on the ends of one winding. Each bipolar

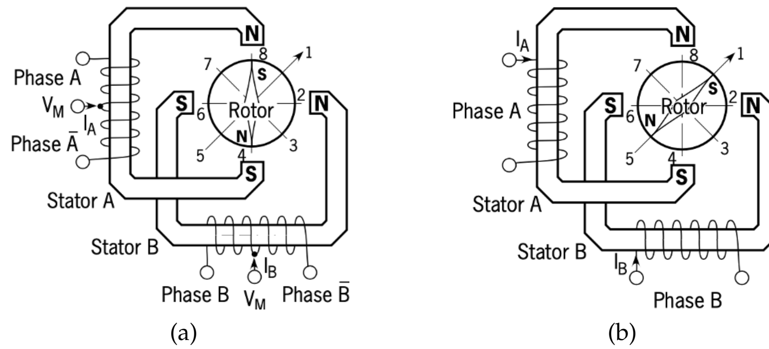

Figure 3.30: Different type of windings [53]. (a) Unipolar motor. (b) Bipolar motor.

motor needs two H-bridges as it has two windings. More details concerning driver circuits can be found in [53, 54]. There are several features that must be taken into account before selecting a particular motor such as physical size, step size and torque vs speed.

One of the characteristics to take into account when choosing a stepper motor is its step size. For instance, in the case of hybrid motors, step sizes range from 3.6° (100 steps per revolution) to 0.9° (400 steps per revolution). Torque and speed characteristics are also to be considered when selecting the stepper motor, a typical "speed-torque curve" is shown in Fig. 3.31, where the vertical axis represents the torque and the horizontal axis represents the rotor speed of the motor in P.P.S. (pulse per second), which is the pulse number (number of steps) per second. Here, the holding, pull-in and pull-out torques, as well as the maximum

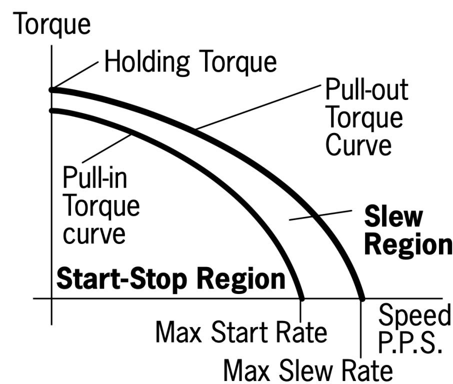

Figure 3.31: Torque vs. speed characteristics of a stepper motor [53].

slew rate shown in Fig. 3.31 are briefly introduced. The holding torque is the maximum torque produced by the motor at standstill i.e., the torque required to rotate the motor's shaft while the windings are energized. The pull-in torque is the maximum torque at which a

motor can start to rotate without acceleration to move the load, at a given frequency, from a standing start without losing any step. The stepper motor cannot start to rotate when the load torque exceeds the pull-in torque. The pull-in curve defines an area called the start-stop region and represents the maximum frequency at which the motor, with an applied load, can start/stop instantaneously with no loss of synchronism. The pull-out torque is also called "dynamic torque" and indicates the highest torque that a stepper motor can produce dynamically, while rotating, without losing steps. The motor goes out of step if it operates at a point beyond the pull-out torque curve. The region between the pull-in and pull-out curves defines an area called slew region. When the motor works in this area, it needs to be accelerated or decelerated and not started/stopped instantaneously. The maximum slew rate is the maximum operating frequency of the motor when no load is applied.

When the pull-in torque is not high enough, a quick start/stop is not possible, and the motor must be accelerated incrementally from a low frequency. The higher the inertia (mass) of the load, the harder it is to start and stop the motor. The pull-in characteristics also vary according to the load i.e., the greater the load inertia, the smaller the pull-in area. It can be seen from the shape of the curve that the stepping rate affects the torque output capability of the stepper motor. As the speed increases, the torque output decreases because the inductance of the motor is the dominant circuit element at high speeds. Moreover, the shape of the speed-torque curve may vary depending on the type of driver used. Most motor manufacturers provide these speed-torque curves for their motors and it is important to understand the type of driver or drive method used by them when developing the curve, because the torque and speed characteristics of a given motor may vary significantly depending on the drive method used.

Stepper driver A stepper drive can be used to control stepper motor operation. Stepper motor drives are specifically designed to drive stepper motors and they operate by sending current through various phases in a series of pulses to the stepper motor. A stepper motor translates electronic signals into mechanical movement whenever an input pulse is applied to the motor driver and each pulse moves the rotor in constant increments. In order to rotate the rotor by one revolution given a motor with a resolution of 1.8°, the stepper motor should receive 200 pulses (360°/1.8°= 200) in full step operation.

A stepper motor is classified by it step angle and also according to its frame size corre-

sponding to the diameter of the motor body. For instance, the body diameter of a stepper motor of size 11 is approximately 1.1 inches. However, in the same frame size classification, the body length may vary and the torque available at the output of a motor of a particular frame size will increase as the body length increases.

The operating principle of stepper motors is to switch its stator poles to the logical values LOW and HIGH in order to achieve the desired steps. To do this, it is required a logic to generate the switching sequence for these voltage levels. It is possible to implement this using a microcontroller. However, microcontrollers have an operating voltage limit (i.e., 3.3 V or 5 V while many stepper motors work at higher voltages. Therefore, to control a stepper motor using a microcontroller, we would need a stepper driver. The rated voltage of the stepper drive is higher than the voltage of the microcontroller. Stepper drives make the voltage switching simple and safe.

Moreover, stepper motors operate at high current then a microcontroller while stepper motor drivers are designed to switch high current or reverse its direction triggered by low current electrical input signals. Some of the stepper motor drivers include logic circuits (such as DRV8825 [55]) in addition to a Darlington transistor array or an H-bridge based MOSFETs, and these drivers also require even fewer input signal pins.

Addition of a stepper motor and motor driver Controlling a brushed DC motor is simple compared to a stepper motor. In fact, it is enough to apply a voltage to make them rotate and use a PWM signal to control the speed. They also offer high torque at low speeds. However, a stepper motor can be a good choice when controlled motion is required. They offer a great advantage in applications where rotation angle, speed, position and synchronism need to be controlled. Stepper motors have a high number of poles compared to DC motors and can move precisely between their many poles without the use of a position encoder. Precise increments in movement allow excellent speed control, which makes them a good choice for this project.

Before arriving at the choice of components to replace the DC motor, several tests were carried out. The components provided in the Arduino kit were employed to make an initial study of the feasibility of the control system for this project. This preliminary study with kit components was also done because it was possible to work from home at a time when access to the lab was limited due to Covid19.

The work on the positioning system started with a L293D motor driver, a ULN2003 based stepper drive board, a small DC motor and a 28BYJ-48 stepper motor. L293D motor driver [56] can be used for both DC motor and stepper motor. With its two H-Bridges, it is capable of driving a pair of DC motors or one stepper motor. Each H-Bridge is used to drive one of the electromagnetic coils of a stepper motor. It was used to drive the DC motor giving a PWM signal to control the speed of the motor. The L293D can provide bidirectional drive currents of up to 600 mA at voltages from 4.5 V to 36 V. It was suitable to drive the original DC motor. Nevertheless, during the development of the positioning system it has been decided to use a stepper motor.

As mentioned before stepper motors offer more advantages than a DC motor for the project where is it required to control the positioning of the objectives. The ULN2003 driver board [57] was used to to work with the stepper motor 28BYJ-48 [58]. This stepper driver consists of an array of 7 Darlington transistor pairs and each pair can drive loads of up to 500 mA and 50 V. his driver was used because it was included inside a board made to be used with the motor 28BYJ-48. The stepper motor 28BYJ-48 is 4 phases, 5-wire unipolar motor and runs on 5 V. Each step made by the rotor corresponds to a rotation of 11.25°and therefore it makes (360°/11.25°) 32 steps per revolution. Since it is a geared motor, with a gear ratio of 64:1, it can rotate the motor shaft by 0.176° (11.25°/64) at each step.

To run the stepper motor, the Arduino was programmed using two libraries: Stepper and AccelStepper. These libraries provide extra functionality by making it easy to manage motor operations. They were employed to implement functions to control the direction and the speed of the motor. For testing purposes, a pointer was attached to the rotor to simulate a clock. By moving the rotor one step at a time and controlling the number of steps, it was possible to position the pointer in any mark on the clock. Since the motor was moving in full-step mode, the difference between one mark and another was 5.625°degrees, which equals the angular resolution of the motor. The rotation of the motor will result in a linear movement of the objectives. Therefore, being able to position the rotor on certain marks on the watch also means being able to control the positioning of the objectives.

The AccelStepper library [59] improves on the standard Stepper library by adding new functions. Accelstepper supports acceleration/deceleration and half-step driving. Previously, with the Stepper library, the motor was moved from a standstill at the set speed in approximately one step. This generated jerky movements both when the rotor started

and when it stopped moving. With the AccelStepper library, by using a smaller, constant acceleration/deceleration until the set speed is reached, the problem of jerky movement was solved. Concerning the acceleration, to accelerate the motor a pause is used between two consecutive steps and this pause gradually decreases as the number of steps increases. To decelerate, this pause is gradually increased starting from the minimum value. Moreover, thanks to the AccelStepper library it was possible to turn the motor also in half-step mode. In microstepping control, such as half-step mode, the driver does not deliver discrete current pulses, but sends two sinusoidal voltage waves with a phase difference of 90°to the motor windings. These sinusoidal voltages allow the current in the windings to gradually rise and fall, moving the motor by fractions of a full-step. There are some benefits of microstepping control. For instance, the angular resolution increases. Microstepping control provides very smooth motor rotation than full-step operation. Moreover, microstepping control can split a full-step producing a small step angle, thus significantly increasing the resolution (the smallest increment the motor can move). However, as the resolution increases, the torque output per incremental step decreases. This can lead to a degradation of motor accuracy if the incremental torque is insufficient to overcome the load and inertia of the motor [60].

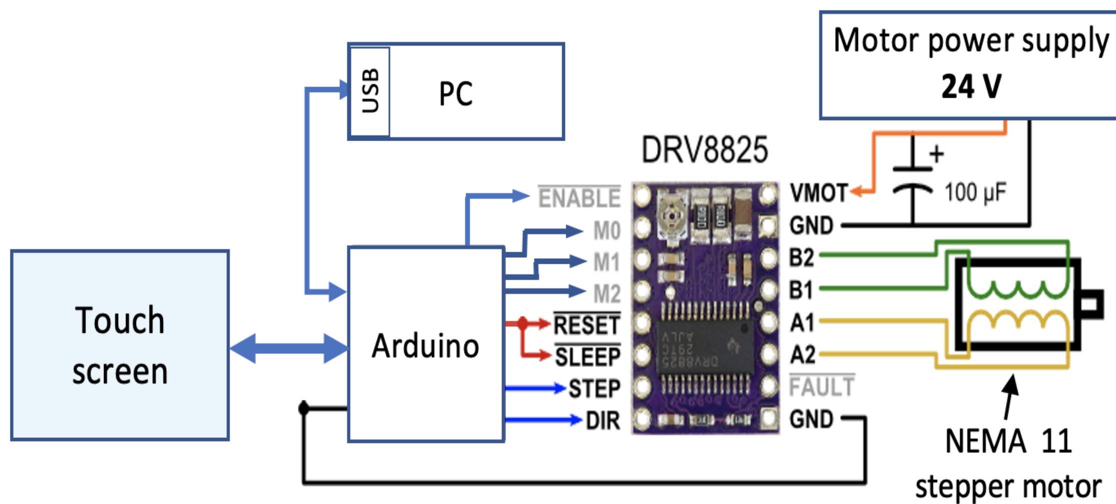

Figure 3.32: Stepper motor and the driver DRV8825 added to the positioning system is controlled through the touch screen display (adapted from [61]).

After realising that it was possible to implement the system to control the objectives, thanks to the preliminary study with Arduino kit, new components different from those in the kit were selected. A new motor and a motor driver were selected because the latter ones inside

the kit had specifications that did not meet the requirements of the project. As a motor, a NEMA 11 stepper motor was employed, as well as the driver DRV8825 as a stepper motor driver (Fig. 3.32). In the following, the considerations made before the selection of the stepper motor and its driver will be discussed.

Motor selection The DC motor inside the microscope is connected to the microscope knob by a gear with a gear ratio of 6:1 (90/15). The microscope knob is graduated with 125 marks. One interval of the graduation on the knob corresponds to a vertical shift of the objective of 1 µm (page 13, on [30]). Therefore, to move the objectives 1 cm the knob would need to make 80 (1 cm/125 µm) revolutions. The 28BYJ-48 stepper motor has a maximum speed of 15 RPM (revolutions per minute) [62]. To run 480 revolutions (80 revolutions $\cdot$ 6) at a rate of 15 RPM, the stepper motor 28BYJ-48 would take 32 (480/15) minutes. However, this time was very long as the maximum time suitable for this project would have been less than 2 minutes. In order to move the objectives by 1 cm in less than two minutes, it is required a motor that makes at least 240 (480/2) revolutions per minute. For this reason, a NEMA 11 as a stepper motor was selected. The NEMA 11 employed in this project has following features: 200 Steps/Rev, 0.67 A/Phase and dimension of 28 mm $\times$ 45 mm [61]. This motor is a hybrid bipolar stepper motor with 2 phases (4 wires) and can be controlled by a stepper motor driver. During the selection of this motor, several factors were taken into account, i.e. size, resolution, pull-out torque and rotation speed.

The space available inside the microscope for the motor was about 3 cm wide and 5 cm long. Therefore, the size of a NEMA 11 was right for this project. There were two variants of this motor, i.e. one long and one short. The longer one was chosen even though it was a bit narrow. This decision was made because with the same diameter, the length of the motor also influences the torque provided by the motor (see *A brief introduction to DC motor and its driver* in Section 3.2.4). There was not much information available on the microscope in order to calculate the load torque and acceleration torque to find the torque required by the motor. The small stepper motor provided with the Arduino kit was used to make some experiments with different weights. These experiments showed that the torque of 300 gf $\cdot$ cm (grams-force x centimeters) provided by the small motor was enough to move the microscope knob. Up to a speed of 7000 PPS, the stepper motor NEMA 11 can deliver a torque of more than 300 g $\cdot$ cm as shown in Fig. 3.33. Therefore, this motor was well suited for the purposes of this project.

However, for this project, only speeds up to 4000 were to be considered, because since the Arduino clock frequency is 16 MHz, the fastest motor speed that the AceelStepper library can reliably support is about 4000 PPS (pulse per second) [63].

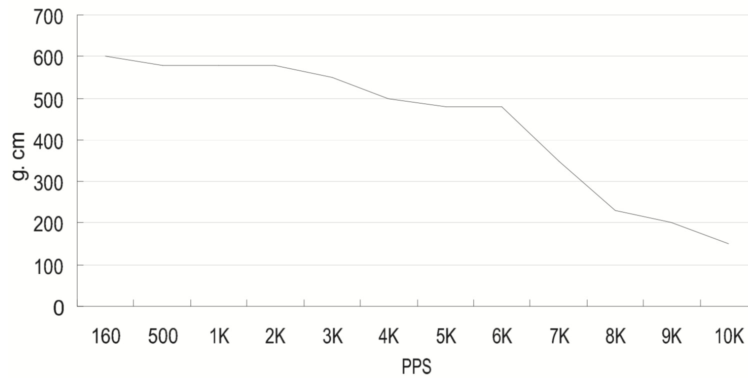

Figure 3.33: Nema 11 - Pull-out torque curve. V_{MOTOR} 24 V, $Phase_{current}$ 0.67 A, Half-Step mode [64].

The pulse rate of the motor determines the speed of the motor and one pulse per second means one step per second. With the new motor to move the objectives by 1 cm i.e., to make 240 revolutions, it is need to step the motor at a speed of 1600 PPS, which is well supported by the motor. To find the speed, the following calculation has been made:

$$\frac{400 \cdot 240}{60} = 1600 \quad PPS.$$

Where 240 are the total revolutions, 400 are the steps required for one revolution at half-step mode and 60 are the seconds in 1 minute.

To run the motor, a new stepper driver was employed since the ones inside the Arduino kit were not able to provide 670 mA, required by the new stepper motor. As a stepper motor driver the driver carrier provided by Pololu was selected [65]. This stepper motor driver carrier includes the controller DRV8825, which is designed to drive a bipolar stepper motor [66]. DRV8825 is a microstepping motor controller with built-in indexer for easy operation. It allows configuration of the motor in full-step up to 1/32-step modes. It provides also a simple step and direction control interface. This device has two H-bridge and it operates from 8.2 V to 45 V and can deliver up to approximately 1.5 A per phase without a heat sink.

Moreover, the carrier board comes with a potentiometer which allows to set the maximum output current. This operation is needed to use voltages above the stepper motor's rated voltage to achieve higher step rates and higher torque [67]. Choosing a high voltage for the

motor reduces the effect of BEMF on decreasing the current in the windings (Eq. 3.17), thus also the torque is less affected. The rated voltage of the motor NEMA 11 is 4.5 V. Dividing this voltage by the motor resistance per phase, the value of the rated current can be found i.e., 670 mA. Since this rated current must not be exceeded, it is required to limit the maximum current flowing through the motor coils. This maximum current can be limited to 670 mA by setting a reference voltage (V_{ref}) using the potentiometer on the driver carrier. A guide on how to set this Vref can be found in [65]. The value of V_{ref} is calculated using a simple formula [66]:

$$V_{\text{ref}} = \text{Current limit} \cdot (\text{A} \cdot \text{R}_{\text{Isense}}). \tag{3.20}$$

Where the current limit is 670 mA, R_{Isense} is 0.1 Ω (R_{Isense} = R_3, [68] and A is a gain equal to 5 set by the DRV8825 internal circuit [66]. Substituting the values inside the formula, it is possible to find V_{ref} = 0.67x5x 0.1 = 335 mV.

From Table 2, on the datasheet [66], representing the relative current and step directions, it can be noticed that when setting the motor for full-step mode, the driver uses only 71% of the winding current. Therefore, when the motor is used only in the full-step configuration, the winding current limit can be raised up to 940 mA (0,67x0.71 = 0.94). Since, the motor is employed only in microstepping mode in this project, the current limit is set to 670 mA.

Thanks to the driver, a higher voltage than the motor rated voltage can be used as motor power supply. The motor voltage of 24 V was selected, same as the voltage used to derive the pull-out torque in the Fig. 3.33. A 100 µF electrolytic capacitor across motor power supply pins was added, as suggested in [65]. The addition of the capacitor is necessary as the driver has low-ESR ceramic capacitors on board, which makes it vulnerable to voltage spikes. This occurs especially in cases like ours where power cables longer than a few centimetres are used. In some situations, these spikes can exceed 45 V (the maximum rated voltage of the DRV8825), which could damage the driver and even the motor.

To control the driver and therefore the stepper motor, the AceelStepper library was initially used. For example, it was used for calibration, for moving up and down with two different speeds, for positioning in certain predefined positions. However, during the development of the positioning system custom functions needed to be implemented. AccelStepper provides functions that allows to move the objectives from a position X to Y, but to do this it is required to know the distance in steps between X and Y beforehand. Instead, the positioning system required functions that could generate steps without knowing Y's position. For this reason,

new functions were developed and the AccelStepper library was employed only for few operations such as calibration and objectives movement with low speed. Moreover, the AccelStepper library was used to define the maximum speed and maximum acceleration for proper motor operation. In order to find the maximum speed and adequate acceleration several experiments were carried out by providing different values for speed and acceleration. And once these values were found, based on these values new customized functions were implemented. For instance, when move the motor is moved upwards while holding the button on the display, the motor accelerates until it reaches maximum speed. It then runs at that constant speed and when the button is released, the motor stops. Since it was not possible to know in advance when the motor should stop, the maximum speed was set such that the motor was not in the SLEW region. There was no information about this region and as seen above, this region is defined by 2 curves (Pull-In and Pull-Out) and it widens as the speed increases (Fig. 3.31). The stepper motor, NEMA 11, provides a high torque up to 7000 PPS (Fig. 3.33) and by using it below 4000 PPS, it was expected to operate the motor outside the SLEW region. In fact, from the experiments, using the AccelStepper library, it was found that the motor was able to stop instantly under 4000 PPS. In addition, it was found that an acceleration/deceleration rate of up to 1000 was well tolerated.

In order to accelerate the motor up to the maximum speed, pulses were sent to the controller in the form of a signal as in Fig. 3.34. Where the T_{ON} time was kept it fixed at 18 µs and decreased the T_{OFF} time with every 100 pulses until the maximum speed was reached. The T_{OFF} time at the beginning is 1000 µs and decreases to 268 µs when the motor reaches the maximum speed. Each time the time T_{OFF} decreases, the speed increases accordingly and in about 10 s it reaches 3497 PPS. This results in an acceleration rate of:

$$\frac{3497 - 982}{10} = 252 \text{ steps/s}^2,$$

where 982 is the PPS at the beginning. The acceleration rate 252 steps/s^2 is acceptable as it is less than 1000.

The time 18 µs (T_{ON}) was taken from the waveform obtained during the experiments using the AccelStepper library. During the experiments with the library, it was found that the time T_{ON} was 20 µs and T_{OFF} was varied until a maximum speed of about 4000 PPS was reached. Similar procedures were implemented for the custom functions employed for the position control system. Moreover, several tests were carried out by varying the T_{ON} and T_{OFF} and

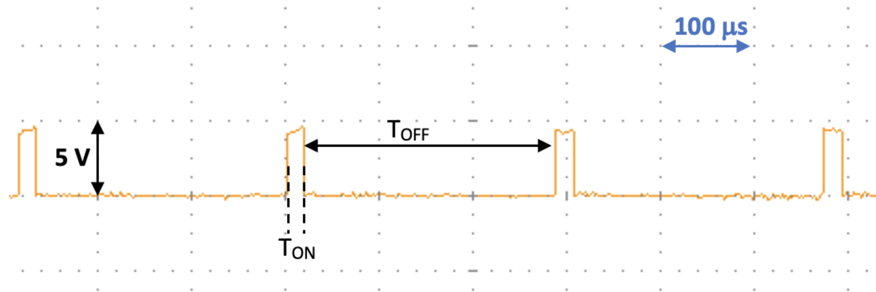

Figure 3.34: Signal period when the motor is rotating at maximum speed. Measurement made with an oscilloscope.

giving more than 4000 steps per second, it was found that sometimes the motor got stuck or made strange noises. For this reason the maximum speed was taken under 4000 PPS (i.e., 3497 PPS) and as said before this speed was more than enough for this project. In the Arduino code, for T_{ON} it was used 16 µs because the microcontroller needs time to execute instructions and thus 16 µs became 18 µs in reality.

For deceleration same thing was done i.e., T_{ON} was fixed at 14 µs and T_{OFF} from 244 µs increased to 1000 µs. The deceleration function was implemented only for the function that manages the positioning of objectives in predefined places. The controller was set to 1/fourth mode to make positioning more accurate. This microstepping mode along with the use of acceleration and deceleration made the positioning slow. Therefore, in this positioning function a different rate of acceleration and deceleration was used, i.e. T_{ON} was set to 14 µs instead of 18 µs in order to have a higher acceleration rate. The motor accelerated up to 70% of the position to be covered and then the last 30% was reached by decelerating. The deceleration was used for two main reasons. First, because in the positioning in preset positions, the arrival position was known. Second, it was needed to make the motor stopping smooth and slow so that the positioning was more accurate. In addition, a low speed before stopping decreases the vertical displacement of the encoder housing and so the error in positioning is also decreased. A low speed also gave the system more time to update the encoder position in order to stop the motor (see *Addition of an encoder* in Section 3.2.4). The acceleration was used to have smooth and non-abrupt movements. In addition, the low initial speed could be used to move the objectives a few distances.

As said before, the AccelStepper library was still used only for the calibration function and for moving the objectives up and down at low speeds. In the following, it will be presented how the AccelStepper library has been employed for the calibration and for the low speed

movement.

To perform the calibration, the right limit switch was used to figure out when the default position was reached. For the calibration, a high enough number of steps were given to the driver to move a metal piece, linked with the motor movement, so that it did not touch and trigger the right limit switch (see *Adjustment of the limit switches* in Section 3.2.4). In the following, it is described the calculation to find the minimum number of steps to be taken by the motor to bring the metal piece to trigger the right limit switch.

Between the left and right limit switches there are about 10 cm and in one cm there are about 20 indents in the threaded rod on which the metal piece moves (see *Adjustment of the limit switches* in Section 3.2.4). In addition, the piece of metal covered about one indent with each revolution of the knob. Therefore, the controller in full-step mode to cover 10 cm had to provide: $200 turns \cdot 6 turns \cdot 200 steps = 240.000$ steps. Where 200 turns are the revolutions of the knob to cover 10 cm, 6 are the motor revolutions per one complete turn of the knob and 200 are the steps per motor revolution. According to this approximate calculation to move the piece of metal 2 mm the controller must provide 4800 steps. A check on the accuracy of this calculation was done after the mounting of the encoder on the piece of metal (see *Addition of an encoder* in Section 3.2.4). It was found that the steps provided by the controller to move the encoder 2 mm were 4820. Therefore, this manual calculation had been very accurate.

During development the half-step mode was employed for the calibration and therefore the step numbers calculated above has been doubled to 480,000. The half-step mode was used to reduce the impact of the metal piece on the limit switch. The right-hand limit switch often gave problems by getting stuck and this led to a system malfunction because the limit switch generated so many interruptions. So once the limit switch was reached, the metal piece could not be moved from over the switch. Therefore, a new way to handle the calibration was employed. With the new way, once the limit switch was hit, the motor automatically moved the piece of metal from above the limit switch. Hence, also the zero position (default position) was shifted by few mm.

Concerning the use of AccelStepper library for up and down movements of the objectives at low speed, the library was used in the same way as for calibration. The only difference is that in this case a small number of steps were chosen for the motor to take. Compared to the high speed version, this function allows a more precise and accurate movement. In this case, each touch on the display corresponds to fixed steps made by the motor with a very small

acceleration. The fixed number of steps were such that the motor rotated the focus knob one mark, which corresponds to the displacement of 1 μm of the objectives (Fig. 3.38). The fixed number of steps varies depending on how the controller is used. For instance, in full-step mode it was calculated that to turn one mark it is needed need to provide about 10 steps. This number was found by dividing the steps needed for one revolution of the focus knob, that is 1200 by the number of marks on the knob, that is 125.

In order to achieve greater control of the objectives through the positioning system, two external buttons have been added in addition to the software side: one to reset and one ON/OFF to manage the controller (Fig. A.8 in the Appendix). The reset button is used to restart the Arduino if the system freezes. The ON/OFF button activates and deactivates the controller and therefore also the motor. The ON/OFF button is also used to switch off the motor if the motor does not stop where it should.

During development, the number of fixed steps was slightly changed for one mark on the knob. To move the objectives at low speed, instead of full-step 1/fourth-step was chosen and the number of steps for this mode was 80, but it was set to 50. Using 1/fourth-step and 50 steps, it was possible to move the focus knob even less than one mark with a smooth and accurate movement.

Adjustment of the limit switches

The stepper motor is connected to the microscope knob, which in turn is connected to a threaded rod. There is a piece of metal on the threaded rod that moves laterally when the knob is turned. This metal part is used to operate the limit switches that are used to limit the movement range of the objectives and therefore also to limit the motor (Fig. 3.35). The two limit switches are used to stop the motor to prevent damage to the objective and the motor itself.

An ordinary limit switch is an electromechanical device that consists of a mechanical actuator connected to a series of electrical contacts. When an object, such as the piece of metal mentioned above, makes physical contact with the actuator, the movement of the actuator plunger will cause the electrical contacts inside the switch to close (for normally open circuits) or open (for normally closed circuits) their electrical connection. Limit switches use the mechanical movement of the plunger to change the electrical switch status. Inside the microscope there were three limit switches used previously for motor control. They are

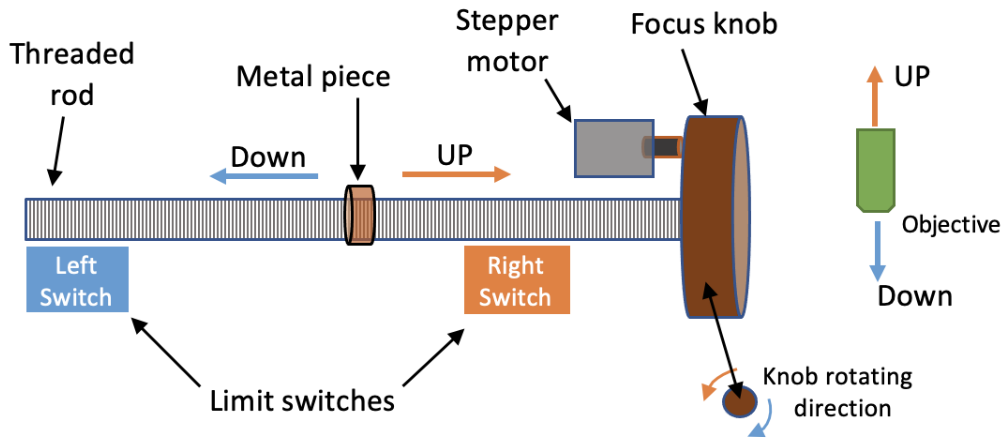

Figure 3.35: Limit switches inside Zeiss-AXIOMAT. The metal piece moves when the focus knob turns and it is used to trigger the limit switches.

normally close circuit and for the positioning system only two of them were used. A fixed one (Right-Switch) that limits the upward movement of the objectives and a mobile one (Left-Switch) used to limit the downward movement.

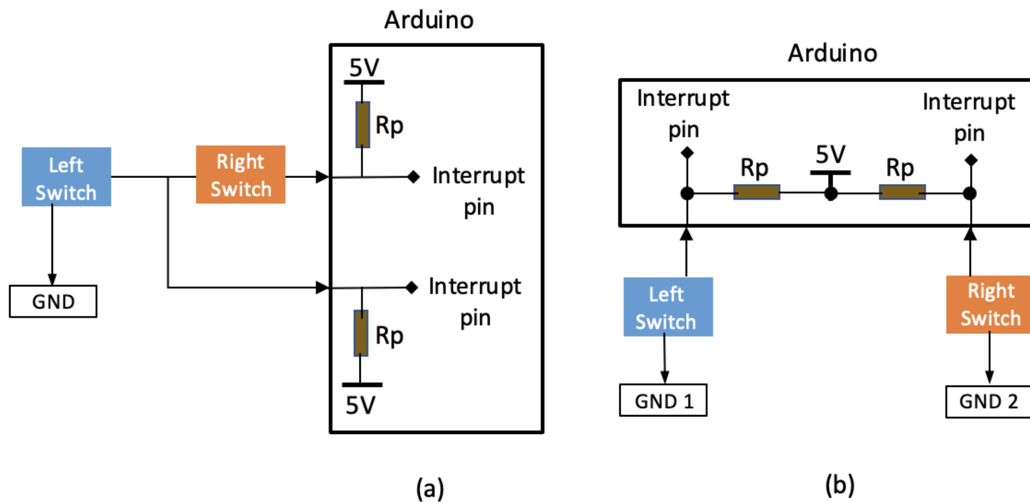

Figure 3.36: Limit switches connection. The internal pull-up resistors Rp of Arduino are shown. (a) The two limit switches connected in series. (b) The two limit switches connected in parallel with separate ground.

To handle the signals from the limit switches, 2 interrupt-enabled pins on the Arduino were used (Fig. 3.36). A modification of the existing connections of the limit switches was required because when the left limit switch triggered, the right one also generated a signal. This was due to the fact that the limit switches were connected in series (Fig. 3.36a). Therefore, the two

limit switches were separated and connected in parallel, but despite this, the limit switches still sometimes triggered together. It was found that the use of same ground pin for the limit switches caused some sort of cross talk between them. Therefore, to two separate grounds were employed for the switches and this solved the latter problem (Fig. 3.36b).

Addition of an encoder

The sections above described the addition of a graphical user interface through a display, the replacement of the internal DC motor with a stepper motor and a driver, as well as the adjustment of the limit switches during the development of the wide-field MOKE microscope. This section introduces the addition of an encoder, which has and important role in the development of the position control system. Moreover, two communication protocols employed to manage the encoder will be described.

In general, an encoder is a device that converts data from one format to another. In position sensing, it can detect and convert mechanical movement into an encoded analog or digital output signal. More specifically, encoders encode angle of rotation and linear displacement. An encoder that detects rotation is called a rotary encoder and an encoder that detects linear movement is called a linear encoder.

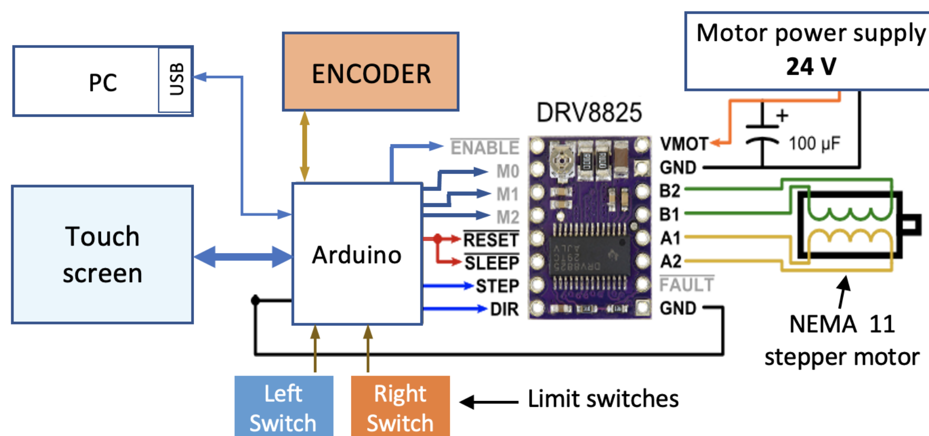

Figure 3.37: Addition of the encoder RLM to the positioning system. It is controlled by Arduino.

In this project, an encoder was included for a better positioning of the objectives (Fig. 3.37). An incremental magnetic encoder was employed to sense the position variation of the objectives. An incremental encoder does not indicate the absolute position, unlike an absolute encoder, it only reports changes in position. Moreover, it provides the direction of movement

for each reported position change. For this project a RoLin miniature packaged was selected, which is a component level encoder [69]. It operates at 5 V, which makes it suitable for Arduino.

A resolution of 1 µm was selected for the encoder, which corresponds to the movement of the objectives when the focus knob is turned by one mark. The resolution is the smallest movement detected by the encoder. The encoder has been attached to the piece of metal used for the limit switches (Fig. 3.38). This choice is due to the fact that the displacement of the metal piece is linked to the displacement of the objectives. When the focus knob is turned, the metal piece moves before the objectives. This means that when an objective lens moves 1 µm, the piece of metal will move more than 1 µm. So the choice of a resolution of 1 µm was sufficient to detect the displacement of the piece of metal and therefore also the objectives.

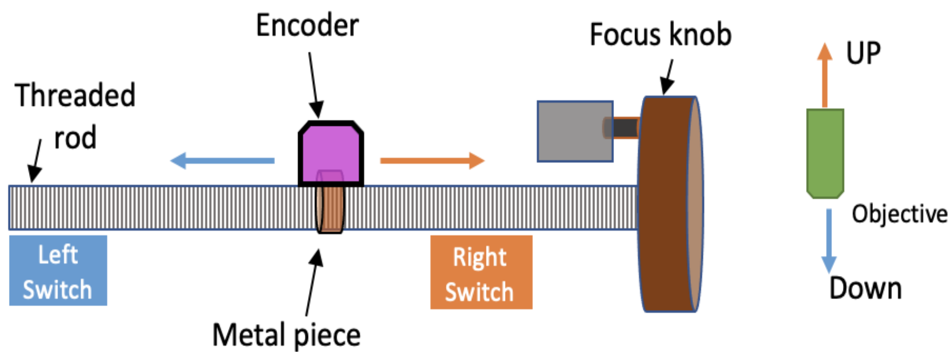

Figure 3.38: Encoder is fixed on the metal piece which moves left or right depending on the focus knob rotation direction.

The minimum edge separation (µs) of the PWM output signals of the encoder and its resolution (µm) influence the maximum speed at which the encoder can move [69]. The minimum speed offered at a resolution of 1 µm corresponds to 0.2 m/s (i.e., 240 cm in 2 minutes) was more than sufficient for this project. However, it was chosen 0.47 m/s corresponding to a minimum edge separation of 1 µs, as their price was the same.

The encoder has an internal period counter, and it is reset automatically when the encoder is switched on. Using the SSI or BiSS communication protocol it is possible to read the value of the period counter. This counter counts every time the encoder travels 2 mm. In addition to this counter, it has an internal counter that counts the position within 2 mm. With a resolution of 1 µm, this counter counts a maximum of 2000 times. This number also corresponds to the interpolation factor corresponding to the 1 µm resolution. The counter bits

are represented by the letter P and the internal counter bits by S as shown in Fig. 3.39 for the SSI protocol. The position information is output in incremental quadrature and parallel, SSI or

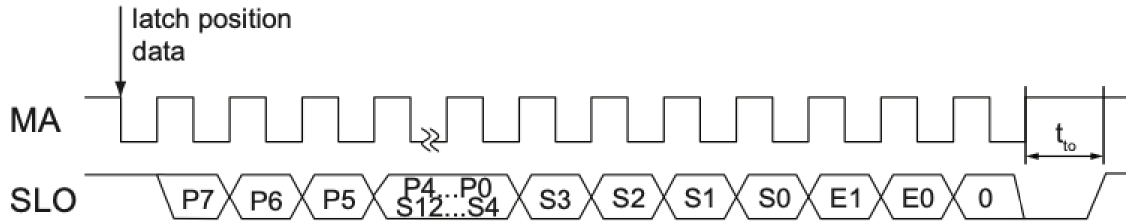

Figure 3.39: Encoder - SSI - Timing diagram [69].

BiSS format. For this project the option incremental quadrature with SSI output were selected. This choice was mainly due to the fact that SSI was compatible with the SPI used by Arduino. Reading the output using SPI protocol instead of reading two interrupts signals (A and B [69]) generated by the incremental encoder made the system faster. The incremental encoder uses a quadrature encoder to generate its A and B output signals. The pulses emitted by A and B have a PWM waveform with a duty cycle of 50% as they are encoded in quadrature. This means that when the incremental encoder is moving at a constant speed, there is a 90° phase difference between the two outputs. This phase difference between signals A and B is positive or negative depending on the direction of movement of the encoder. These two signals were read by the Arduino using the interrupt pins and every time the encoder moved, an interrupt was generated. Therefore, the Arduino had to handle several interrupt routines while the encoder was moving. Instead, using the SPI protocol the output could be read only when necessary. Thus, the system was not overloaded with continuous interrupt calls.

Inside the microscope the encoder can move a maximum of 13 cm. Covering this distance the counter would count a maximum of 65 and therefore an 8-bit counter is sufficient. However, for the length of the period counter 24 bits was selected because in the datasheet [69] there were some inconsistencies in the representation of the P and S bits. Due to the presence of bit S13 it seemed that the number 24 referred to the total bit of the output. Since the price of the device did not differ much, 24 bits were chosen to be on the safe side. However, after contacting the manufacturer it was verified that the presence of S13 in the datasheet is incorrect.

Two other features that are important for this project are related to the SSI protocol and are the maximum master clock frequency of 4 MHz and the timeout of 20 µs. While reading

the counter bits, it was found that the timeout value reported on the datasheet was wrong. Instead of being 20 μs it is only 2 μs. Before understanding how this value was obtained, a brief SSI e SPI communication protocols working principles will be given. Moreover, it will be also discussed how SPI was employed instead of SSI to read the encoder bits.

SSI communication interface Synchronous serial interface (SSI) is a serial interface standard widely used in industrial applications (especially encoders). It is a synchronous, point-to-point connection from a master (such as a microcontroller) to a slave (such as an encoder) (Fig. 3.40). In this type of interface, position data is continuously updated by the sensor and provided to the output register. The clock and data signals are transmitted according RS-422 standards

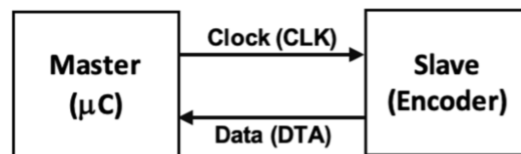

Figure 3.40: Simple SSI block diagram [70].

[70]. Synchronous data transmission is a transmission method that employs a common clock signal to transmit data synchronously between the receiving end and the transmitting end. Since there are no start and stop bits, the bandwidth of the data transmission can be better exploited to obtain more message bits and make the whole transmission process easier. An ideal SSI timing diagram is shown in Fig. 3.41 and it represents a single data transmission using SSI protocol.

In the idle state, the encoder clock line and data line are kept HIGH while the slave continues to update its current data (Fig. 3.41). The transmission mode is triggered when the master starts a train of clock pulses. After the first falling edge of the clock (A), the slave automatically freezes its current data. With the first rising edge (B), the first bit (MSB) is transmitted, and with the following rising edges, bits are transmitted sequentially to the output. Then when the LSB is transferred (end of transmission) a further rising edge of the clock sets the clock line HIGH (C) and the data output LOW since there is no bit to transmit. The data line remains LOW for a period of time, t_m, to recognize the transfer timeout. If a clock signal (data output request) is received within this time, the same data will be transmitted again (multiple transmission). On the other hand, if there are no clock pulses within time t_m, the data line is set to HIGH (idle mode) and the slave starts updating

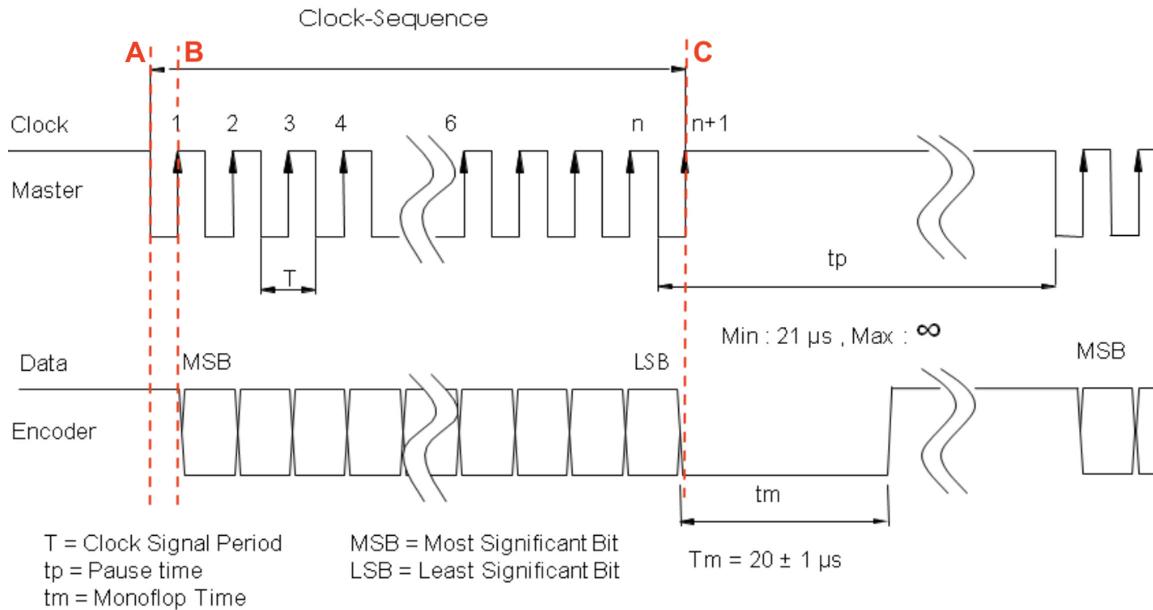

Figure 3.41: SSI timing diagram (adapted from [70]).

its value. This means that the single transmission of the data word is finished. The time t_m stands for transfer timeout. This is the minimum time required by the encoder to detect that the data transmission is complete. The time t_p is called the pause time or the delay between two consecutive clock sequences from the master.

SPI communication interface Serial Peripheral Interface (SPI) is a serial communication protocol. It is a synchronous, full duplex interface based on master-slave. A master can send data to a slave and a slave can send data to the master simultaneously. To enable synchronous data transmission, the SPI uses four wires. An SPI can have only one master and can have several slaves. A master is usually a microcontroller and the slaves can be a sensor such as an encoder.

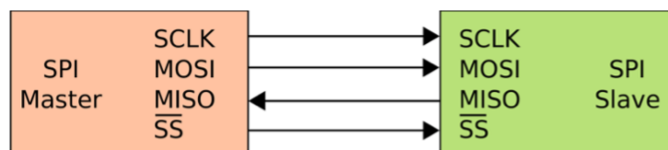

Figure 3.42: Simple SPI block diagram [71].

The SPI interface has four lines (Fig. 3.42) MISO, MOSI, SS, and CLK:

MISO: Master in Slave Out - The Slave line for sending data to the master.

MOSI: Master Out Slave In - The Master line for sending data to the Slaves.

SCK: Serial Clock - The clock pulses which synchronize data transmission generated by the master.

SS: Slave Select – This line connected to the SS pin of a slave is used by the master to select the salve. Each SPI device needs a unique SS line back to the Master. The Master using a normal GPIO pins selects the salve on the SPI bus to communicate with it. The term Chip Select (CS) is sometimes used instead of Salve Select (SS).

To initialize SPI communication, the master sets the SS pin of the slave to LOW and then send the clock signal. During communication, data is simultaneously transmitted (shifted out serially onto the MOSI bus) and received (the data onto the MISO bus is sampled). The clock generated by the master synchronizes the shifting and sampling of data. The SPI interface allows to select the rising or falling edge of the clock for sampling and/or shifting the data.

In SPI, the master can set the clock polarity (CPOL) and clock phase (CPHA). The CPOL bit sets the polarity of the clock signal during the idle state. The CPHA bit selects the clock phase. According to the CPHA bit, the rising or falling clock edge is used to sample and/or shift the data. The master needs to select the clock polarity and phase according to the requirements of the slave. Depending on the selection of the CPOL and CPHA bits, there are four SPI modes [72].

Configuration of SPI as SSI In the description of the protocols above, some similarities between the SSI and SPI protocols can be found. For instance, they are two serial and synchronized protocols and they both have one line for clock and one line for data transmission from slave to master (Fig. 3.40 and Fig. 3.42). Therefore, it is possible to configure SPI to use SSI in order to read bits from the encoder.

To configure the interface of the protocols the clock (MA) and slave out (SLO) of encoder were connected to SCK (pin 52) and MISO (pin 50) of Arduino, respectively. The encoder has no MOSI and SS pins. There was no need of a SS pin to select the encoder since only one slave was employed i.e., the encoder. Therefore, it was enough to send the clock pulses to read the bits from the encoder.

In SSI (Fig. 3.41), the clock and the data line are HIGH in the idle state and the bits are transmitted on the rising edge of the clock. The SPI, on Arduino, was configured in the same

way through the employment of the SPI library. The data mode was set as SPI_MODE2 and the clock divider as SPI_CLOCK_DIV16 [73]. The data mode SPI_MODE2 was used to set the idle state of the clock and of the data. Moreover, in this mode (CPOL 1 and CPHA 0), the master transmitted its data on the MOSI on rising edge and samples encoder data, available on the MISO, on falling edge. The encoder put out its data on MISO bus on the rising edge of the clock. The clock divider SPI_CLOCK_DIV16 was used to divide the clock frequency of Arduino. Arduino Mega has a clock frequency of 16 MHz and it was divided this by 16 in order to stay below the permissible clock frequency of the encoder i.e., 4 MHz.

Arduino with the SPI protocol can transmit/receive one byte at a time. This means that to get more than 8 bits, it was needed to send/read several times. In this case, the encoder did not receive any data from Arduino but for the communication it was required that the master sends something. Therefore, a byte of worthless (dummy) data was transmitted on the MOSI line even if there was nothing connected. For instance, in the following reading it was sent 0 as a dummy data to receive the first byte from the encoder: firstByte = SPI.transfer(0x00).

Bit number	1	2	...	9	...	16	17	18	19	20	21	22	23	24	25	26	27	28	29	30	31	32	33	34	35	36	37	38	39	40
SLO bits	1	P23	...	P16	...	P9	P8	P7	P6	P5	P4	P3	P2	P1	P0	S10	S9	S8	S7	S6	S5	S4	S3	S2	S1	S0	E0	E1	0	X
Inside Bit No.	7	6	...	7	...	0	7	6	5	4	3	2	1	0	7	6	5	4	3	2	1	0	7	6	5	4	3	2	1	0
Byte number	B5			B4			B3								B2								B1							

Figure 3.43: Bytes read by Arduino.

The encoder had in total 38 bits as slave output (SLO) bits (Fig. 3.43). This means it is required to read 5 times to get all the SLO bits. The 38 bits were given by the sum of 24 P bits, 11 S bits, 2 E bits and one 0 bit. Where P bits are the period counter bits, S bits are the position inside period counter bits, E bits are the error bits and 0 is set by default. In this configuration, the encoder had 11 S bits because the S bits counter, counts until 2000 and it is needed 11 bits to represent 2000. The error bits were used to report various faults encountered by the encoder.

When reading the bits from the encoder, the first bit read (bit number 1 or bit 7 of the byte B5) was not P23 but it was a 1. This occurs because Arduino starts to sample the SLO data with the first falling edge of the clock while the SLO output is still frozen to HIGH i.e., 1 (Fig. 3.44). This only happened for the first bit of the SLO bits and for the other bits after that the reading was normal. To read the 38 SLO bits, the SPI function "SPI.transfer(0x00)" was called 5 times, paying attention not to exceed T_{t0} (i.e., 20 µs) between two consecutive calls.

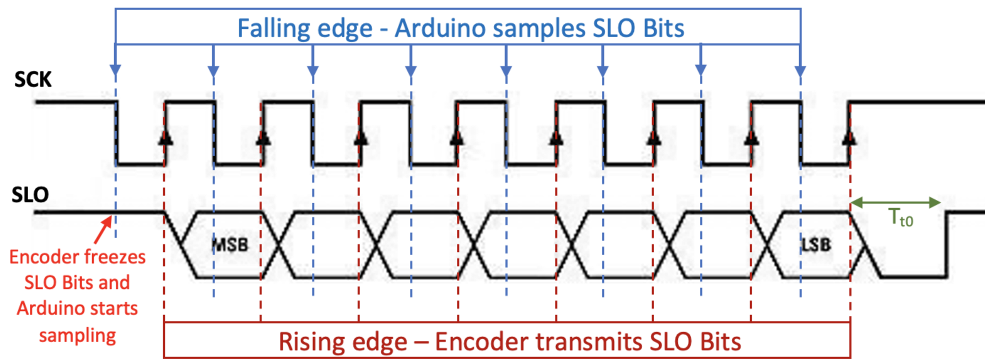

Figure 3.44: SPI as SSI - Timing diagram.

However, with the readings unreliable bits were found, i.e. they varied with each reading. To find a solution, several tests were made employing a pulse generator [74] and an oscilloscope. With the pulse generator, 40 pulses was applied with a lower frequency of 250 kHz and the encoder output bits were read with the oscilloscope. A low frequency was used to exclude the high frequency from possible causes. Using the pulse generator, stable bits were obtained from the encoder output (SLO bits), which meant that the problem related to the unstable value was due to Arduino. The issue related to unstable bits reading was solved accessing directly the registers (SPCR, SPSR and SPDR) used to manage SPI communication. In other words, the functions provided by SPI library was not used anymore for the reading of the encoder output bits (SLO bits). Instead, the SPI registers were used for the reading, bypassing the SPI library. The bits of the registers (SPCR and SPSR) need to be set in order to configure the communication parameters, while the data register (SPDR) is used to receive the encoder bits (SLO bits). The communication parameters chosen were the same as those used before with the SPI library, i.e. frequency of 250 kHz, idle state of CLK and DATA line HIGH.

Directly accessing the data register to read the bits solved the earlier problem and it was possible to read the SLO bits even with the Arduino. However, even though the bits were stable, they did not match the expected value. In other words, if it was expected to read 2, the encoder gave a very high value that was different from 2. To find a solution to this issue, several tests was carried out with the pulse generator and the oscilloscope. Analyzing the output of the Arduino with the oscilloscope a 1 bit (HIGH level) was found at the beginning of every 8 bits. It seemed that the encoder after every single transfer (of the total 5) set the output to 1. Measuring the time between two consecutive transfers and it was found a T_{t0} of

2 µs. This meant that the time t_0 was not 20 µs as stated on the datasheet, but 2 µs. For this reason after 2 2 µs the output was set high (point A in Fig. 3.45a). Immediately afterwards, it met the falling edge so encoder froze the data (point B in Fig. 3.45a). At the next rising edge it output the first data, i.e. 0 (point C in Fig. 3.45a). The first bit 0 was correct because the encoder was not on the magnetic scale. For a better understanding, more tests were carried out with the pulse generator giving pulses at different frequencies. Analyzing the output on

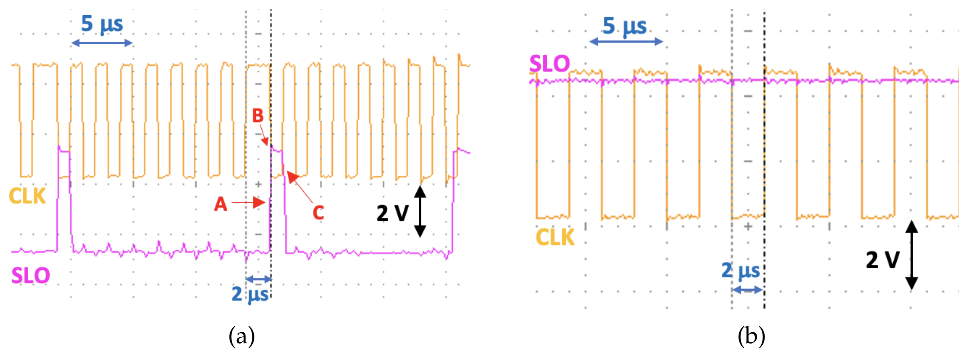

(a) (b)

Figure 3.45: Encoder timeout verification. (a) The first bit is high at every transfer. Arduino provides the CLK signal. (b) All bits are high at every transfer. Pulse generator provides CLK signal.

the oscilloscope it was found that for frequencies below 250 kHz the output was always High (Fig. 3.45b). This means that immediately after the start of the transfer, if the clock is high for more than 2 µs then the encoder terminates the transfer by bringing up the output. Then for each subsequent falling edge of the clock the encoder freezes its data, but it is not able to output anything as it has to immediately terminate the transfer and so the output remains at 1. It was also found that for frequencies above 250 kHz, and therefore also at 4 MHz, the encoder provided stable data.

Some other tests with Arduino were carried out to verify the value of the T_{t0} of 2 µs. A pause between two consecutive transfers was given and studying the behaviour of the encoder depending on the duration of the pause it was found that if this pause exceeds 2 µs then the encoder ends the transfer (Fig. 3.46). In this way, it was possible to be sure about the value of T_{t0} of 2 µs. Thus, the error in the datasheet regarding the time T_{t0} was confirmed.

Moreover, it was found that by varying the frequency the time between two consecutive transfers varied with the frequency. This time became less than 2 µs for frequencies above 250 kHz. Therefore, at the end a frequency of 4 MHz was chosen for the transfers of the encoder bits (SLO bits) as Arduino could read all the encoder bits without any problems.

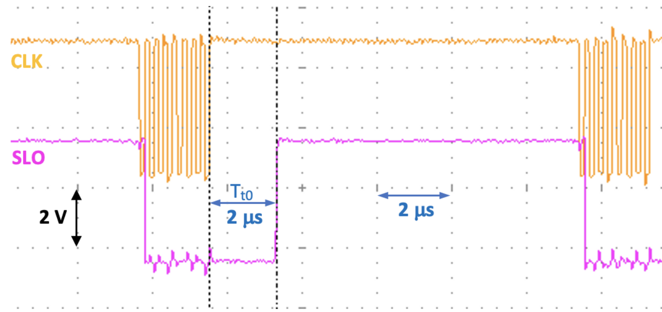

Figure 3.46: Encoder timeout verification with Arduino.

After successfully reading the data, the encoder was installed inside the microscope. The encoder as was positioned as shown in Fig. 3.47, i.e. with the earthing pin pointing to the left. This choice was due to the fact that the right-hand switch marks the position 0 and the encoder increments the counters going to the left. The figure shows the displacements of other elements such as the objective and the knob. In addition, the figure shows the situation

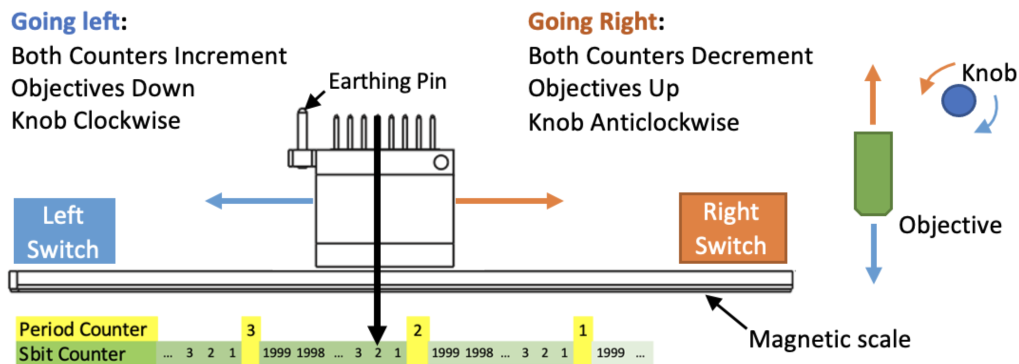

Figure 3.47: Encoder position inside microscope and its displacement.

in which the encoder, after being switched on, has moved to the left from position 0. Moving to the left, the period counter increases with every 2000 counts of the internal counter (i.e., Sbits). The internal counter is the counter that counts the movement within a period. The latter counter also increases as it moves to the left.

When the power supply is turned off, the period counter resets, but the internal period counter does not. This means that after switching the encoder on again, the period counter will read 0, while the internal counter will still read the same position as before. In order not to lose the period information, it was saved in the Arduino EEPROM memory. Another thing noticed was that if the encoder was moved to the right after power-on, the period counter

went into underflow when it had to decrease. This problem was solved by handling the underflow within the function implemented to read the encoder.

In order to install the encoder on the metal piece, a specially designed housing was 3D-printed. Unfortunately, there was barely enough space on the metal piece to fix the housing properly. This led to a problem in positioning due to a vibration of the housing during the shift of the metal piece as well as to a vertical movement of few mm of the housing when the metal piece stopped. Let's take a practical example to explain the problem encountered due to the vertical movement of the housing when the objective was moved to focus the specimen and the position was saved. When the encoder arrived at the focus position, it was stopped and gave 324. Nevertheless, due to the slight vertical movement of the housing immediately afterwards, the encoder gave a different number: 326 instead of 324. Now when the position was saved, 326 was kept in memory instead of 324. Therefore, when the objective needed to be repositioned at the focus point, which was 324, the motor actually stopped at 326, which was the wrong pre-saved position. This error was most visible with long shifts of the encoder and especially in those to the left. However, it was found experimentally that if the positioning was not correct then by simply moving the objective down and giving the positioning command again this error was not anymore visible. Moreover, the using of the deceleration in the positioning of the objective in the pre-set positions reduced the vertical displacement of the housing. Thus, the positioning was smooth and accurate.

At the end, the installation of the encoder hosing was not changed, because in normal microscope operation the objective was not moved much. And, when the positioning is not correct, the objective could be moved down and then reposition it again. The best solution would have been to modify the metal piece in order to better fix the encoder. But the metal piece is connected to other pieces in the microscope, and it was not worth disassembling everything at that time.

By using the encoder, it was possible to save precise objective positions. In order to keep track of these positions even after the system is switched off, the EEPROM memory inside the microcontroller was employed. For each objective the position of the counters were saved i.e., the global period counter and the counter that counts the position within a period i.e. the Sbit values. The global period counter is different from the encoder's period counter (Pbit counter). This global counter was implemented as a solution to the problem of the reset of the encoder period counter after restart and also to handle underflows due to negative

counts. To manage the saving and reading of data from memory, the EEPROM library was employed. All the functions for the positining system were implemented by trying to reduce their number of memory accesses for writing. This was done because EEPROM memory has a limited number of write cycles.

Description of programming functions employed in position control

In order to operate the positioning control system using the microcontroller, several functions were exploited. Each one performs a specific task which then determines the correct operation of the system. Some of these functions are defined by the libraries used in the project and others are written by us. Below a brief description is given about the operation of some of the functions employed for the positioning system.

UTFT myGLCD(Model, RS, WR, CS, RST): defines an object of class UTFT used to manage the screen. The parameters supplied to the function depend on the screen and shield used [43].

URTouch myTouch(TCLK, TCS, TDIN, TDOUT, IRQ): defines an object of class URTouch used to manage the screen touch. The parameters provided refer to the pins used to enable touch management [47].

void rSwitchInterrupt(): handles the interruption generated by the right limit switch. Used to stop the motor and to move the objectives to position 0.

void lSwitchInterrupt(): handles the interrupt generated by the left limit switch. It is used to stop the motor.

void reset_switch_flag(): reads the status of the limit switches and updates the flags associated with them. This function is used to unlock the system when the limit switches generate false interrupts.

void ASwitchInterrupt(): handles interrupts generated by the encoder and updates the objective position. This function is used to take into account when someone turns the microscope knob manually. This function is disabled, in order not to generate so many interrupts, whenever the motor moves the objectives.

void set_period_counter_at_start(): assigns the start position value to a global counter.

void read_encoder(): handles the reading of the encoder bits and does a double check to exclude read errors. This function is called to check the objective position.

bool read_encoder_for_positioning(): handles the reading of encoder bits for correct positioning of the objective. Used only to control the correct reaching of the set position. Returns true when the encoder is at the desired position.

void menu0(): creates a user interface providing the functionality to move, focus the specimen and save preference positions.

void saved(): saves the positions chosen by the user in the microcontroller's EEPROM memory. Saves only if the information is to be updated, thus reducing the number of times the memory is written.

void error_message(int e): prints on the screen the messages chosen to report some kind of problem.

void microstepping(int precision): sets the microstepping mode based on the given value.

void Calibration(): returns the objective and thus also the encoder to position 0. It employs the rSwitchInterrupt() function.

void goUp(): moves the objectives upwards by a small number of fixed steps. Uses acceleration and microstepping.

void goDown(): does the same of goUp() but moves the objectives downwards.

void go_up_high_speed(int x1, int y1, int x2, int y2): moves the objective upwards with a relatively high speed. Uses acceleration and microstepping. It does not use fixed numbers of steps, but makes the motor turn as long as the user holds the up button.

void go_down_high_speed(int x1, int y1, int x2, int y2): does the same thing as (go up high speed) but moves the objectives downwards.

void go_Saved_Position(): handles the positioning of the objectives in predefined places. Uses microstepping, acceleration and deceleration. Accelerates up to 70% of the distance in steps. It automatically calculates when to start decelerating and uses the read_encoder_for_positioning() function.

3.3 Key Support Activities

In this section, the key support activities conducted during the development of the wide-field MOKE microscope are described. These activities are the optimisation of a photodiode amplifier, as well as the design and print of a cage to house all the electronic components needed to control the system.

Optimizing photodiode amplifier circuit

In this project, a photodetector was employed to check the variation of light intensity along the optical path and to obtain a quantitative measure of light (see Section 3.2.1). In particular, an instrument that could measure the relative change of light intensity between one point and another along the optical path was necessary. Despite having a photodetector (Fig. 3.48a), it was not suitable for the work because its output immediately became saturated due to both high gain and maximum output of only 4.5 V. Since the photodetector was employed for a high-power LED matrix, it was necessary that the gain could be set according to the intensity of light measured. Furthermore, a higher maximum output was required for obtaining a wider range of output values depending on the light intensity.

Based on available components in the lab, the photodetector was modified. Since a photodiode generates a current proportional to the light striking its active area, a transimpedance amplifier was employed to convert this current into an output voltage (Fig. 3.48b). A potentiometer (ranging from 100 Ω to 10 kΩ) was used for the variable gain (R_f), a second potentiometer for the offset nulling, two 9 V batteries for $\pm V_{supply}$ and a multimeter to measure the output voltage. As an operational amplifier, a μA741 was employed [75]. The μA741 requires a minimum $\pm V_{supply}$ of ±5 V and can withstand up to ±15 V. All the components were soldered on a prototyping board to obtain a portable photodetector.

During the measurements with the photodetector, an offset of about 10 mV was encountered. Using the potentiometer for the offset adjustment, it was possible to bring the output to 0 V. Mainly two types of measurement were realized: first, the variation of light intensity along the optical path and second, the variation of light intensity only between two lenses. For the first type of measurement, a point very close to the LED matrix was taken as reference and a gain was chosen such that the output remained below saturation. Then, the variation of the light intensity was analyzed along the optical path. For the second type of measurement,

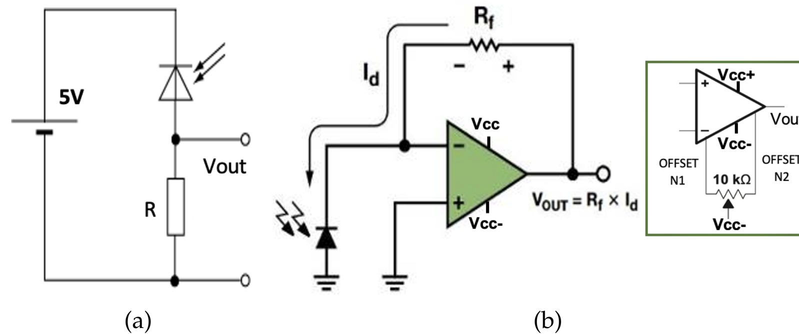

Figure 3.48: (a) Photodiode amplifier with resistor. (b) Transimpedance Amplifier Circuit (adapted from [76]).

a high gain was chosen in order to better distinguish the small variation of light and at the same time the output always remained below saturation.

The first configuration of the photodetector (Fig. 3.48a) was the original one already available. This configuration employed a high value resistor, which was important in other project applications. However, in this project the high value resistor brought the photodetector output to immediate saturation due to high light intensity of the LED matrix. Moreover, the photodiode was seen as a voltage generator and this affected the linearity of the circuit. To overcome these issues, a second configuration of the photodetector was implemented specifically for this project. The second configuration has several advantages compared to the original configuration. In the following, a brief analysis relating the new version of the photodetector optimized circuit (Fig. 3.48b) is presented. The photodetector optimized circuit operates the photodiode in photovoltaic mode, where the operational amplifier keeps the voltage across the photodiode at 0 V. This leads to an increase in response as the capacitor is not charged/discharged. Furthermore, since the voltage is kept constant, the photodiode acts as a current source and the output of the circuit is more linear. The voltage-current curve of the photodiode (Fig. 3.49a) is very similar to that of a conventional diode, with the exception that the entire curve will shift up or down as the light level changes. The total current through the photodiode is the sum of photocurrent (current produced due to the light) and dark current (current generated in the absence of light). The dark current is small for a small reverse voltage across the photodiode (Fig. 3.49b) and this current must be minimized to maximize the sensitivity of the device. Therefore, connecting the photodiode at a virtual ground, the dark current is reduced.

The main reason for the connection of the photodiode to a virtual ground is that there were

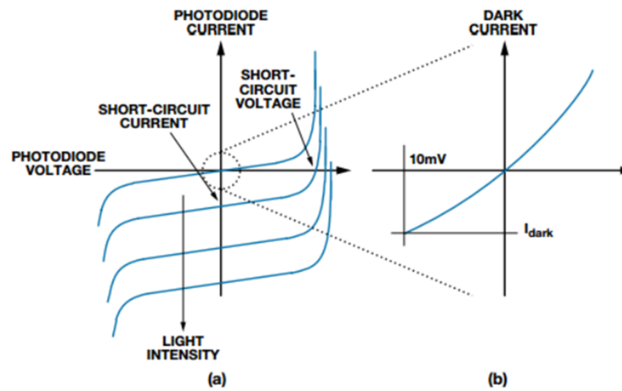

Figure 3.49: Typical photodiode transfer function [76].

no longer constrains relating its reverse bias voltage. Therefore, it was possible to choose a larger V_{supply}, thereby increasing also the maximum V_{output}. However, a reverse voltage of 0 V also means a higher diode capacitance.

When a capacitance, such as the capacitance of the photodiode, is added on the input of an OpAmp, it tends to become unstable. The circuit stability can be evaluated doing the magnitude Bode plot of the frequency response of A(s) combining with the Bode plot of the $1/\beta$(s) (Fig. 3.50a). Where A(s) is the forward gain, i.e. open loop gain, (A_{vd}) of the μA741 and β(s) is the gain of the feedback block, i.e. from output to the $(-)$ terminal. One should look at the frequency f^* where $|$ Gloop$(f^*)| = 1$ and check the closure angle at which $|A(s)|$ and $|1/\beta(s)|$ intersect each other. For this circuit this closure angle is 40 dB/dec before and 40 dB/dec after the intersection (Fig. 3.50a) and this is the case for an unstable but not divergent configuration with a phase margin of $\approx 0°$ [77]. Thus, in the output of the photodetector a not perfect signal with ringing effects must be expected. In fact, in Fig. 3.50 representing the PWM signal of the LEDs driver measured with the photodiode, it is possible to see oscillations at each step. However, the circuit could be stabilized by adding a capacitance C_c across the feedback resistor. The capacitance C_c adds a pole to $1/\beta$(s). The value of C_c can be selected such that the closure angle between A(s) and $1/\beta$(s) is reduced. The pole can be placed at f^* obtaining $1/\beta'$(s) and thus reducing the closure angle to 20 dB/dec. Making the closure angle of 20 dB/dec after the intersection, a phase margin of 45° would be obtained.

Since it was possible to measure the PWM frequency of the LEDs driver using the photodetector, no further stabilization of the circuit was required. The close loop bandwidth of $|F(s)|$,

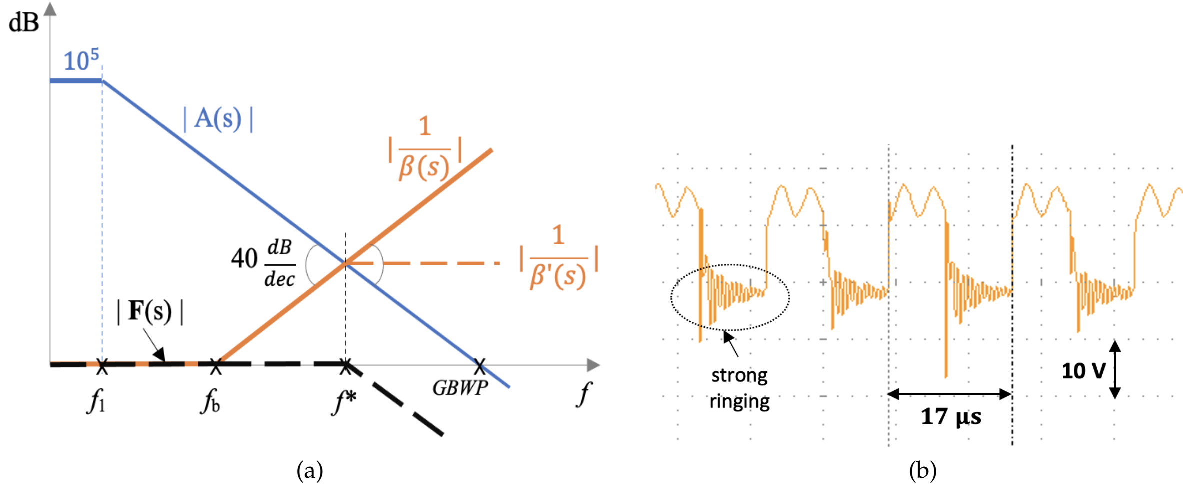

Figure 3.50: (a) Magnitude Bode plot of the Transimpedence amplifier. (b) Transimpedence amplifier output measuring the PWM signal frequency of LEDs driver.

i.e. of the circuit, was calculated from Eq. 3.21:

$$\begin{aligned} GBWP &= A^* f^* \\ A^* &= \frac{f^*}{f_b} \qquad \Rightarrow \qquad f^* = \sqrt{GBWP \cdot f_b}. \\ f_b &= \frac{1}{2\pi R_f (C_i + C_j)} \end{aligned} \tag{3.21}$$

Where f_1 is the first pole of the OpAmp located at the frequency $f = 10\,\text{Hz}$ [75], f_b is the pole of β(s) located at $f \approx 160\,\text{kHz}$, f^* is the closed loop bandwidth, GBWP (1 MHz) is the gain bandwidth product of the OpAmp, C_i is 1.4 pF, C_j is 1.2 nF at $V_{reverse}$ = 0 V [78] and R_f is the feedback resistance. For R_f, 1 kΩ was selected, thus a close loop bandwidth of 400 kHz was found.

Design of housing to host components

So far, the optimization of a photodiode amplifier circuit has been described as the first key support activity in this project. Now, the second key support activity will be introduced.

After the implementation of the positioning system, the electronic components needed to be arranged in an orderly and organized manner. Therefore, a simple housing to hold all the components as well as a housing for the encoder were designed using 3D printing (Fig. A.6 and Fig. A.4 in the Appendix). For the design of the simple housing to hold all

the components, FreeCAD, a free and open-source computer-aided design (CAD) modeler, was employed. FreeCad offers valuable tools for constructing objects. A basic technique of solid modelling called Constructive Solid Geometry (CSG) was used [79]. To design the components housing, mainly primitive shapes such as cubes and cylinders were employed and combined, subtracting one shape from another or intersecting one shape with another. These tools such as combination, subtraction or intersection used during the design are tools of the Part Workbench of FreeCAD. During the housing design several aspects were taken into account, such as ventilation holes, cable connections and the robustness of the container after printing. The corners between one wall and the other were strengthened to make the housing more robust.All the electronic components were installed in their corresponding positions inside the housing and the result obtained was more than satisfactory. Using FreeCAD, also a housing for the encoder was designed in order to fix it inside the microscope (Fig. A.4 in the Appendix).

4 Progress Evaluation after Wide-field MOKE Microscope Setup

The setup of the Zeiss-AXIOMAT microscope as a wide-field MOKE required several working stages, starting from a basic configuration of the microscope until reaching a final configuration allowing the obtainment of satisfactory images of the magnetic domains. At each stage, several strategic setup decisions were taken with the aim of achieving the desired result. In the following, the best images obtained during the different working stages will be presented. These images allow a visual assessment of the better performance achieved by the Wide-field MOKE compared to the Zeiss-AXIOMAT. During the setup, the specimen NM021 (Co/Ir/Pt) was used for magnetic domain imaging, employing mostly 25x and 50x as objectives. Moreover, the LED matrix at maximum power was used when the images of the magnetic domains were taken. For each image, the configuration of the elements contributing to the quality of the image will be provided, e.g. the lenses, the aperture, the analyzer and the exposure time of the camera.

The values of aperture, analyzer and exposure time are mutually dependent. For example, when the incident light perpendicular to the surface of the specimen has to be captured, the aperture will be closed, but doing the amount of light will be reduced. Thus, the exposure time will have to be increased to make the camera sensor more sensitive. In the same way, setting the analyzer towards maximum extinction, light will be reduced. Thus, as before, the exposure time of the camera will have to be increased. By setting these three parameters, satisfactory images of the domains can be obtained.

The diaphragm knob presents marks to indicate the value of the aperture, the maximum corresponds to 35. The opening of the aperture is indicated using these values. Also the analyzer presents marks, which will be used to indicate its position. The analyzer will be kept between 80° and 90°, near the maximum extinction, since the polarizer has been set to

0°. As exposure value, 100 ms to 500 ms will be used.

A high exposure value was used to acquire the first images. Thus, in order to have a comparison also in terms of time, high exposure times were used also during development. As seen above, during the development the light source was replaced and therefore the color of the LED light used will be specified. During image acquisition with the camera the "conversion control" option provided with the PCO camera software was employed. This option allowed a further improvement of the contrast of the images.

Domain images with first configuration: this is one of the first images showing the magnetic domains. This image was obtained in the initial configuration of the microscope, after the replacement of the halogen lamp in the lamp house with the blue LED matrix. The light was focused at the aperture diaphragm with the original Zeiss-AXIOMAT lenses. The aperture was set to 30, the polarizer to 84° and the exposure time to 500 ms. Several images were taken with both the 25x and the 50x. Nevertheless, here only an image taken with the 25x is presented (Fig. 4.1), since the images taken with the 50x were not showing any magnetic domains. In Image 1 (Fig. 4.1), some magnetic domain structures are visible. However, this result was not satisfactory as the exposure time was high, the contrast was not good and, above all, only part of the field of view was visible. This was mainly due to the optical path of the camera system, which had to be redesigned.

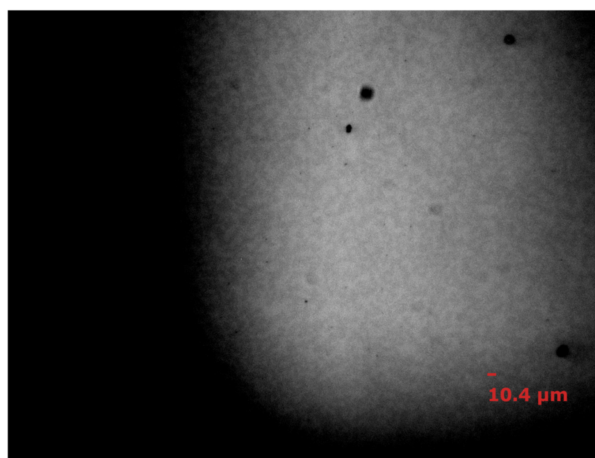

Figure 4.1: Domain image 1 with objective 25x.

Domain image with second configuration: to improve the visibility of magnetic domains after having taken Image 1, some components (e.g. beam splitter) were removed by the optical path of the camera and the camera was aligned with the optical path. In addition, the whole camera system was covered with aluminum foil to remove the disturbance of the ambient light. Instead of having an aperture of 30, the aperture was set to 35. Whereas, the following components remain the same as in the first configuration: blue LED matrix as light source, original lenses to collimate the light source, exposure time of 500 ms, a polarizer of 84°. Similarly to the case of configuration 1, also in this configuration no images of the magnetic domains were obtained through the objective 50x. Fig. 4.2 shows Image 2 obtained with the objective 25x. As before, the results were not satisfactory. The magnetic domains were not

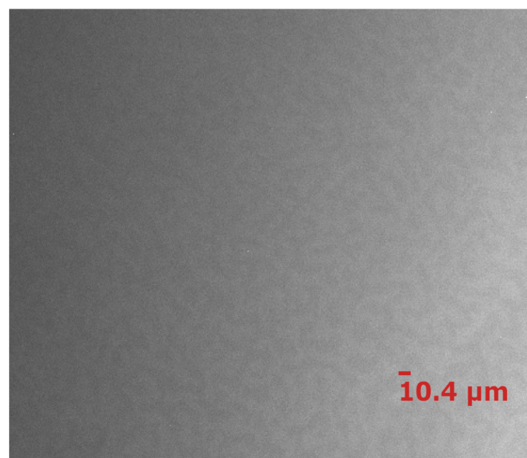

Figure 4.2: Domain image 2 with objective 25x.

visible because of the presence of a bright and a less bright area in the image. This was due to the illumination system, which was not configured correctly. In fact, Köhler illumination was not yet satisfied in this configuration, because the LED matrix was positioned at the bottom of the lamp house. Meaning that it was not at the appropriate position along the optical path for achieving Köhler illumination.

Domain images with third configuration: to achieve Köhler Illumination, the LED matrix was placed in a new customized mounting that allowed the adjustment of its position. Moreover, the lens used to collimate was substituted and a light diffuser was added. After this upgrade, it was for the first time possible to obtain images of the magnetic domains with the 50x objective (Fig. 4.3b). Furthermore, from this moment the positioning system to move

the objectives was operative and the saving position option allowed a quick change of the objectives focus on the specimen. In fact, it was now possible to save the position of each objective and thus, to focus the specimen by simply selecting the option on the touch screen.

For the 25x objective, an exposure time of 100 ms and an aperture of 35 were employed, with the polarizer set to 84°. Whereas, for the 50x objective an exposure time of 200 ms and an aperture of 27 were employed with the polarizer at 84°. The aperture used with the 50x objective is smaller than the 25x because the interference pattern at the back focal plane of the 50x has a smaller size than the interference pattern with the 25x. Moreover, the exposure with the 25x is lower than the one in the configurations before. A smaller exposure time could be set thanks to a correct configuration of the optical components for Köhler illumination.

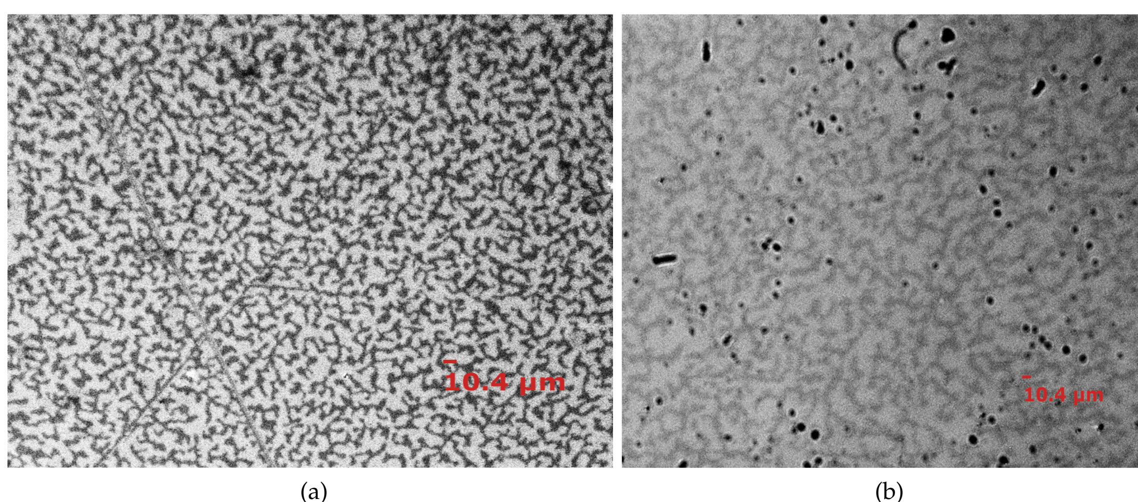

(a) (b)

Figure 4.3: (a) Domain image 3 with 25x objective. (b) Domain image 4 with 50x objective.

These new images present good contrast, especially the image taken with the 25x (Fig. 4.3a), which shows the expected pattern of magnetic domains for this type of specimen. In addition, there are no shadows in the images. However, part of the specimen in the image obtained with the 50x (Fig. 4.3b) was not in focus. This is due to the fact that the stage, where the specimen is placed for observation, was not perfectly flat. In addition, the depth of field is smaller for the 50x objective than for the 25x. Therefore, in the 50x image (Fig. 4.3b) the effect of the tilted stage is more visible. If the image taken with the 25x objective (Fig. 4.3a) was satisfactory, a new configuration was employed to further improve the illumination system and obtain better domain images with the 50x objective. Before describing the results obtained with the fourth configuration, some images taken on the specimen SE031 are briefly

discussed below.

In addition to the specimen NM021, the specimen SE031 containing smaller magnetic domains was employed. The zoom OPTOVAR was also used during these tests. The images of this second specimen (SE031) with the objective 50x did not show any magnetic domains. Whereas, the objective 25x was able to capture the structures of the magnetic domains, even if the image was still not satisfactory (Fig. 4.4). For the objective 25x, an exposure time of 200 ms and an aperture of 33 were set, in combination with the polarizer at 86°were employed.

After having taken this image (Fig. 4.4), the zoom OPTOVAR was employed with the objective 25x, an exposure time of 200 ms, an aperture of 33 and the polarizer at 86° for observing the first specimen (NM021) (Fig. 4.5a). Whereas, the exposure time was raised to 500 ms for observing the second specimen (SE021) (Fig. 4.5b). The exposure time was increased because the use of the zoom OPTOVAR reduced the quantity of light. In fact, the use of zoom OPTOVAR allows images to be magnified, but does not increase the resolution of the system.

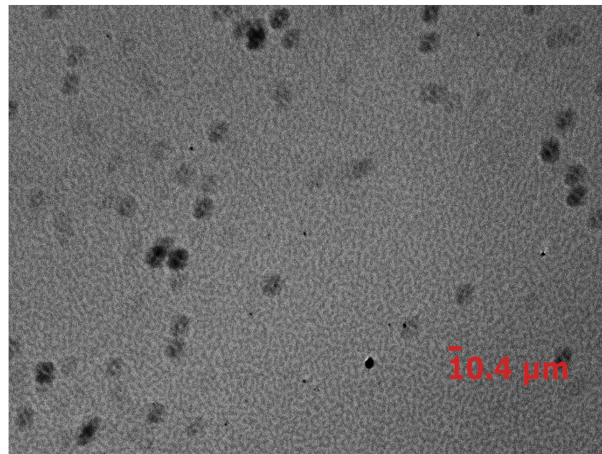

Figure 4.4: Domain image 5 with objective 25x. As specimen a second specimen (SE031) has been used and it contains smaller magnetic domains than the first specimen.

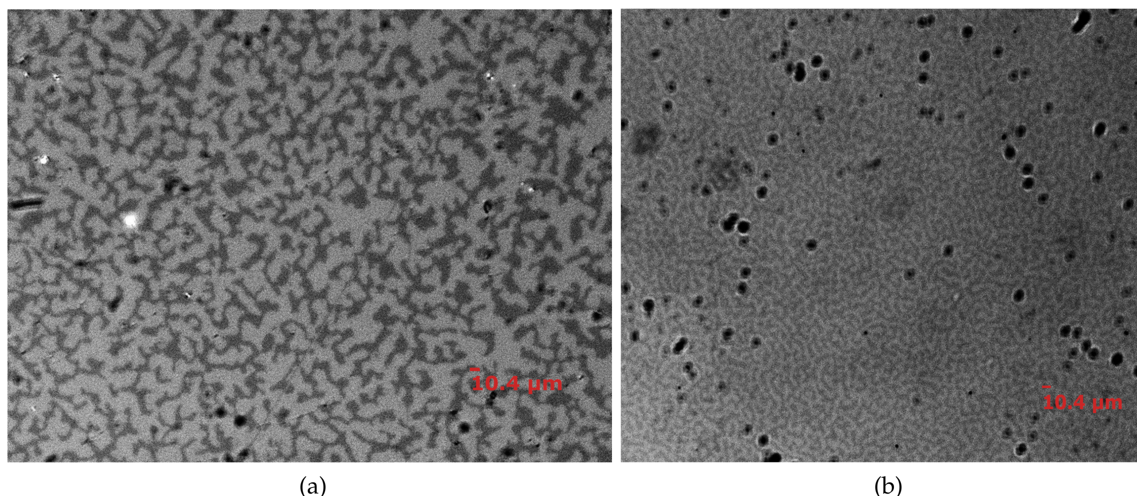

(a) (b)

Figure 4.5: For these domain images Zoom OPTOVAR at 2x with 25x objective has been used. (a) Domain image 6 of the first specimen (NM021). (b) Domain image 7 of the second specimen (SE031).

Domain images with fourth configuration: as mentioned before, configuration 4 was employed to further improve the images obtained with the 50x objective. To do this, the collimation of the light from the source in the illumination system was modified, through the addition of a new lens. This modification allowed more light rays perpendicular to the surface of the specimen in comparison with the previous configuration. These perpendicular rays contributed to the contrast of the image as they contain more information about the MOKE effect measured.

For the objective 25x, an exposure time of 100 ms and an aperture of 33 were set, in combination with the polarizer at 86° were employed. The new image taken with the 25x objective (Fig. 4.6a), presented satisfactory visualization of the magnetic domains. For the 50x objective, the following setting were adopted: exposure time of 100 ms, aperture of 27, and polarizer at 86°. In addition, the slit of the aperture was centered on a single LED. This way, the contrast in the images with the 50x, improved significantly compared to before. Through configuration 4, the image taken with the 50x objective (Fig. 4.6b) improved significantly.

Regarding the images of the second specimen (SE031), configuration 4 improved the visualization of the magnetic domains with both the 25x and the 50x objectives (Fig. 4.7a and Fig. 4.7b). The images show the expected pattern of magnetic domains for this type of specimen (Fig. 4.7a and Fig. 4.7b).

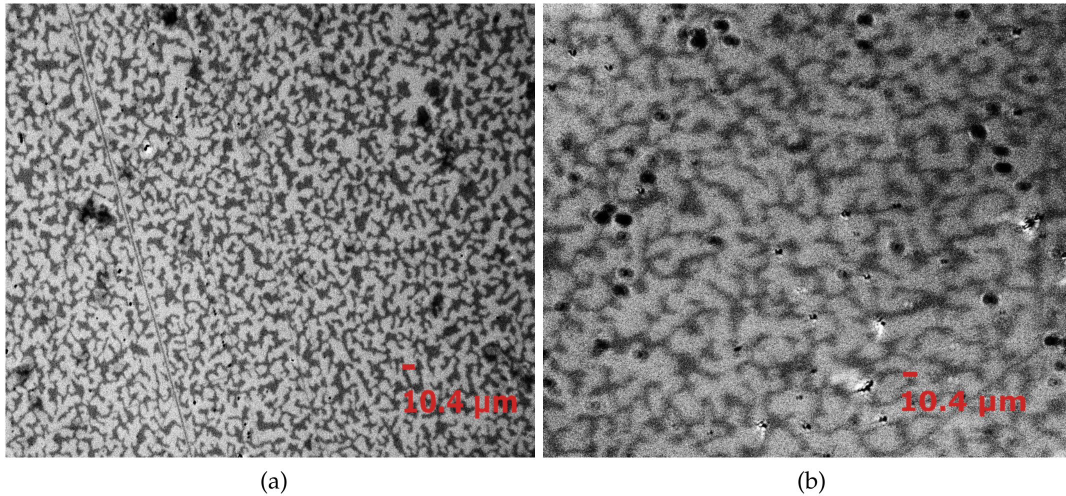

(a) (b)

Figure 4.6: The first specimen (NM021) has been used for these images. (a) Domain image 8 with 25x objective. (b) Domain image 9 with 50x objective.

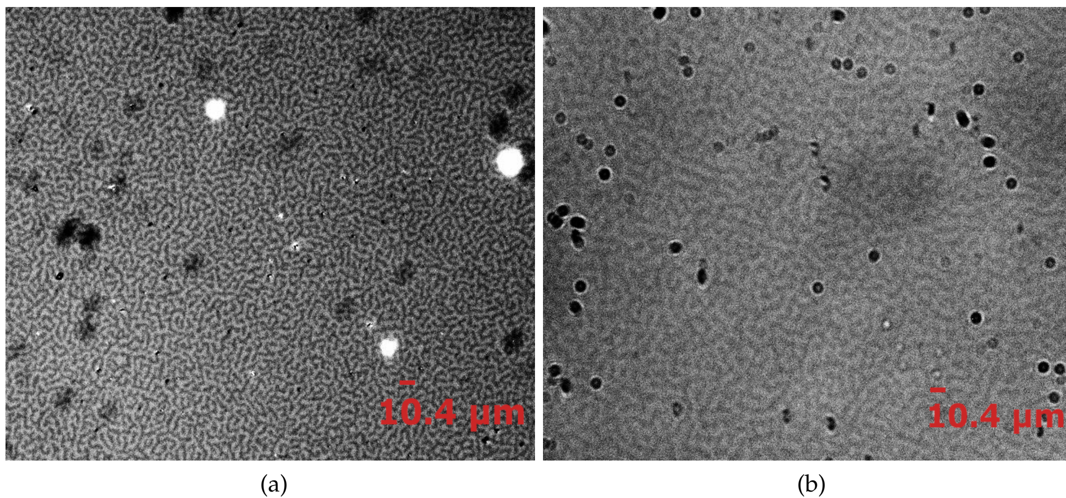

(a) (b)

Figure 4.7: The second specimen (SE031) has been used for these domain images. (a) Domain image 10 using 25x objective. (b) Domain image 11 with 50x objective.

During the development of this project, only the specimen NM021 was used for the most part part of the images. Even though the domain images of the second specimen (SE031) were not as good as the ones of the first specimen, the results obtained were satisfactory. Comparing the images, it is possible to confirm the improvement achieved from the beginning to the end of setup of the Zeiss-AXIOMAT as a Kerr microscope.

Magnetic domain size: After setting up the microscope, the size of the magnetic domains were measured. In order to measure the size of the magnetic domains, the size of a single pixel in the image was first calculated. A specimen having a 30 µm pattern was employed and its images were taken using different lenses. The pattern in the image occupied a number of pixels depending on the objective used. For example, using the 50x objective, the 30 µm wide pattern occupied 58 pixels in the image. The size of one pixel was found dividing 30 µm per 58, obtaining 0.52 µm, which corresponds to the pixel size in the image. In Fig. 4.8, the pixel size of the image relative to each objective is reported.

Objective	Pixel size in the image (µm)
5x	2.5
10x	1.2
25x	0.52
50x	0.25

Figure 4.8: Pixel size in the image depending on the objective employed.

After finding the size of an individual pixel in the image, the size of a magnetic domain was measured by simply counting the number of pixels in the image occupied by the magnetic domain. Through this pixel count, a reference size of 10.4 µm was obtained, which corresponds to the 20 pixels width in the images. This reference size was used to provide a general information about the size of the domains in an image, which corresponds to the expected size of magnetic domains measurable through other wide-field MOKE microscopes (i.e., approximately between 1 µm and 100 µm).

5 Conclusion and Final Considerations

Magnetic domains imaging is widely employed to study microstructures of magnetic specimens in magnetic research as well as in the development of magnetic devices. There are different instruments employed for this purpose. This thesis has focused mainly on the wide-field MOKE microscope and laser-scanning MOKE microscope. In particular, the design, implementation and the characterization of a wide-field MOKE microscope started from a Zeiss-AXIOMAT. Nevertheless, in the various setup stages the future implementation of a laser-scanning MOKE microscope was also considered.

The configuration of the Zeiss-AXIOMAT as a wide-field MOKE microscope was realized through the following stages: improvement of the light source, addition of a CCD camera, obtainment of better objectives control through a positioning system with graphical user interface, substitution of the DC motor with a stepper motor and a driver, and addition of a magnetic encoder.

During the configuration, the improvement of the microscope performance and magnetic domain imaging was verified. For reaching this purpose, a comparison was made between the magnetic domain images obtained at the initial configuration stages and the magnetic domain images obtained after the final configuration as wide-field MOKE microscope.

In particular, after the first configuration, which corresponds to the replacement of the halogen lamp in the lamp house with the blue LED matrix, the domain images obtained were not satisfactory. This was due to the bad contrast, high exposure time and limited visibility of the field of view. After the second configuration, which corresponds to a better alignment of the camera, the domain images were still unsatisfactory. In this case, the exposure time of the camera was still high and the presence of a shadow area in the image suggested an incorrectly configured illumination system. After the third configuration, which corresponds to the addition of a new customized mounting for the adjustment of the LED matrix position to achieve Köhler illumination, better domain images were obtained. Nevertheless, if satisfactory

results were obtained with the objective 25x, further improvement of the illumination system was made in order to obtain better results also with the objective 50x. After the fourth configuration, which corresponds to the addition of a new lens for improving the illumination system and the collimation of the light source, satisfactory domain images were obtained with both the objectives 25x and 50x. The quality of these final images of the magnetic domains were more than satisfactory. In addition, the position control system with graphic user interface provided a good control of the objectives. However, some considerations for further improvement of both the image quality and the positioning control system are reported below.

First, the presence of dust has a negative impact on the quality of the image since it does not allow proper illumination and generates shadows on the specimen. The microscope was set up in a room, which was not very clean. Therefore, the microscope should be moved into a cleaner room in order to wipe the lenses for avoiding disturbances in the final image.

Second, the encoder housing is not always stable. Occasionally, it shifts vertically causing an incorrect reading of the objectives position. Due to time constraints related to this project, it was not possible to find a solution to solve this issue. Therefore, it would be required to find an alternative way to fix the encoder making it more stable in the future.

Third, a large part of the light source gets lost instead of illuminating the specimen. This occurs because of the relatively big size of the light source. Due to limited time, it was not possible to design and develop a new illuminating system including a new and smaller light source. However, a smaller light source such as fibre-coupled LEDs could be used to replace the LED matrix later on.

Finally, the vertical positioning of the objectives to focus on the specimen is exclusively handled through a microcontroller and a touch screen at the moment. Nevertheless, the interface with the microcontroller could be handled with a computer and all the commands could be run via MATLAB.

Despite these considerations for future improvement, the images obtained after the final configuration presented magnetic domains with a better defined shape and better contrast in comparison to the images obtained in the previous configurations. Therefore, it is possible to conclude that the setup of the Zeiss-AXIOMAT as wide-field MOKE microscope was successful. The final results show that the wide-field MOKE microscope now allows the study

of microstructures on magnetic specimens for research relating magnetic devices. Moreover, the setup of the Zeiss-AXIOMAT as wide-field MOKE microscope was realized taking into consideration also the future additional setup as laser-scanning MOKE microscope. The future double configuration will allow higher benefits for the study of magnetic devices, because it will be possible to study the characteristics of specimens both locally (through the laser-scanning MOKE microscope) and on a wider area (through the wide-field MOKE microscope).

Appendix

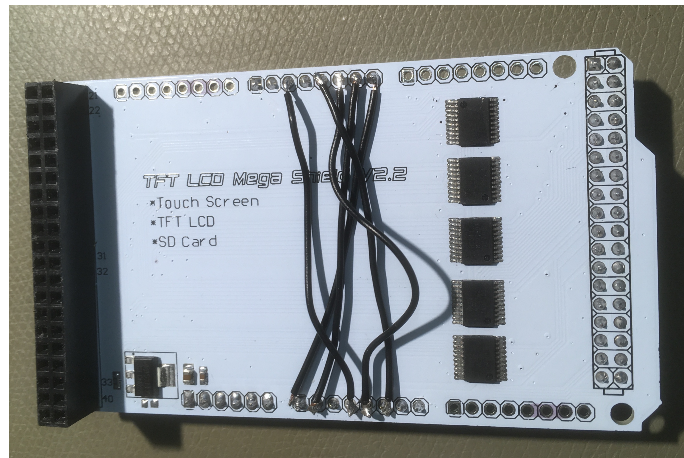

Figure A.1: Pins reallocation of the Arduino display shield.

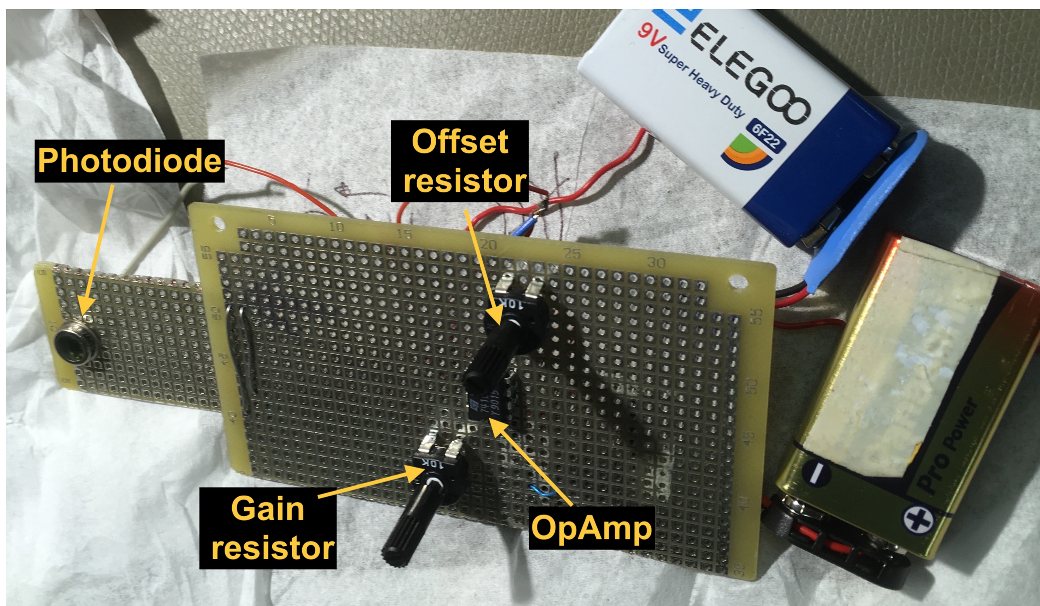

Figure A.2: Adapted version of the photodetector.

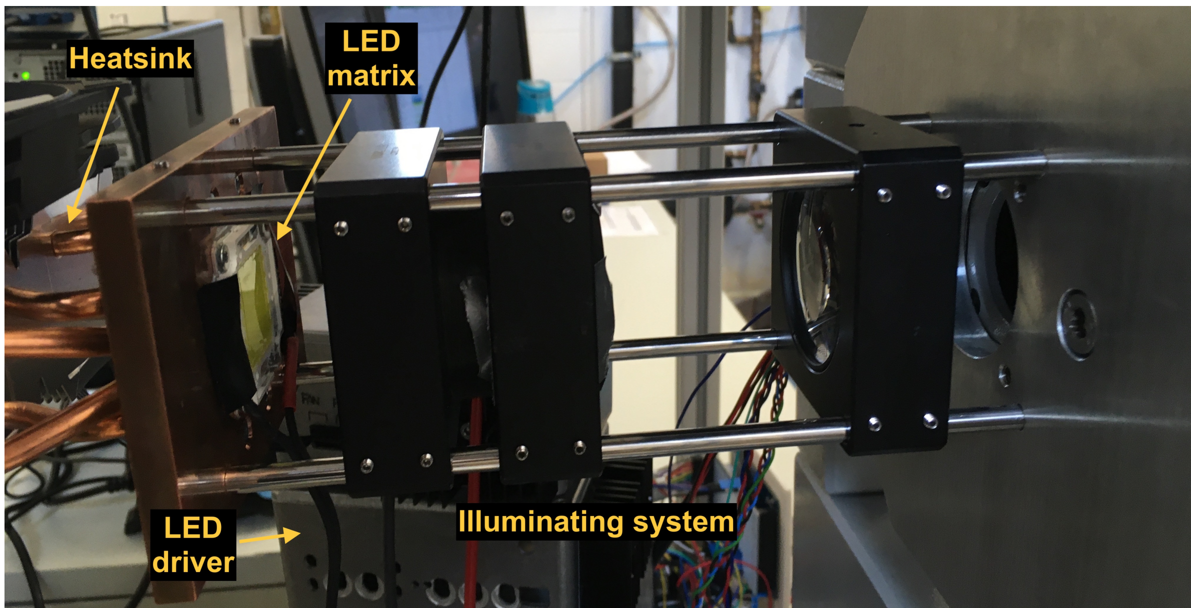

Figure A.3: Illuminating system after the setup of Zess-AXIOMAT.

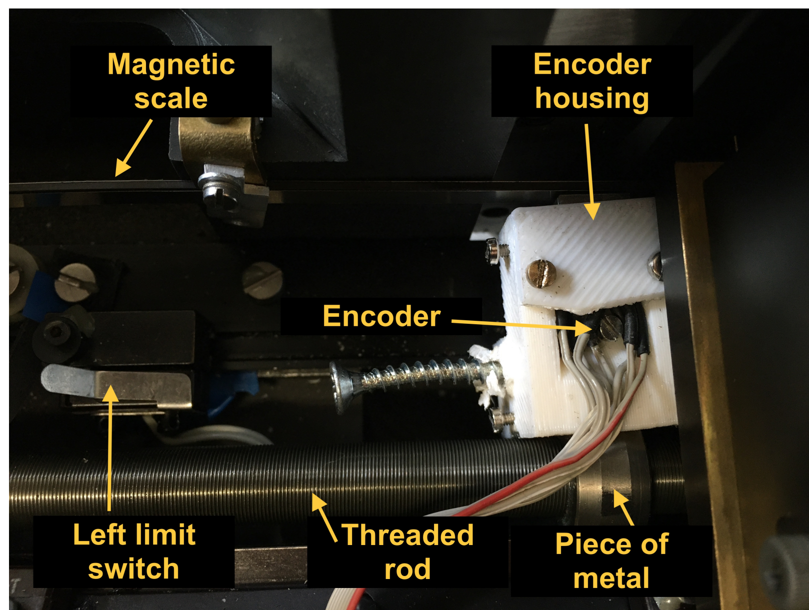

Figure A.4: Encoder housing and left limit switch inside the microscope.

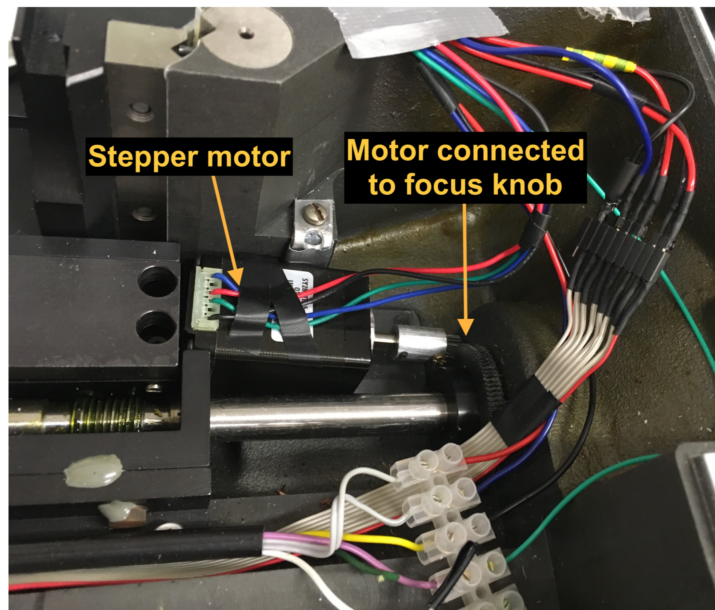

Figure A.5: Stepper motor inside the microscope.

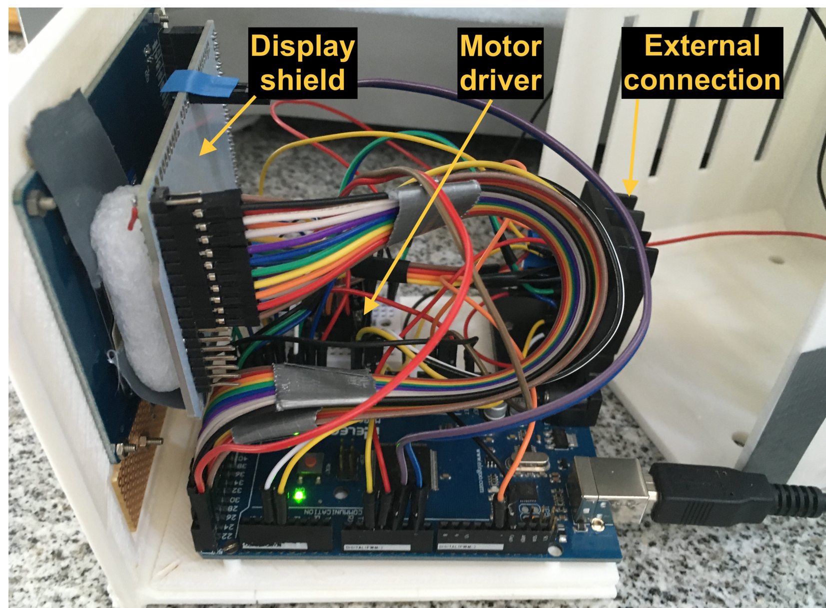

Figure A.6: The touch screen with its display shield is fixed to the front face of the components housing. Arduino MEGA 2560 and stepper motor driver are fixed to the bottom face of the components housing.

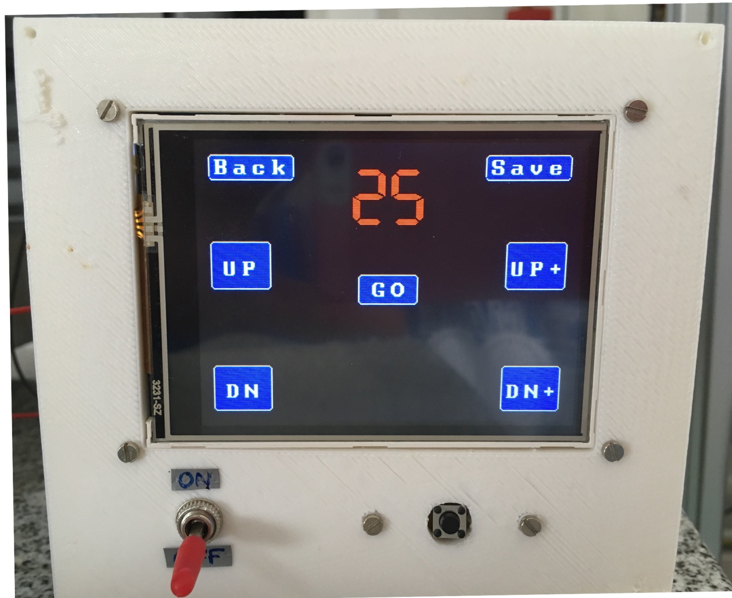

Figure A.7: Touch screen inside the component housing.

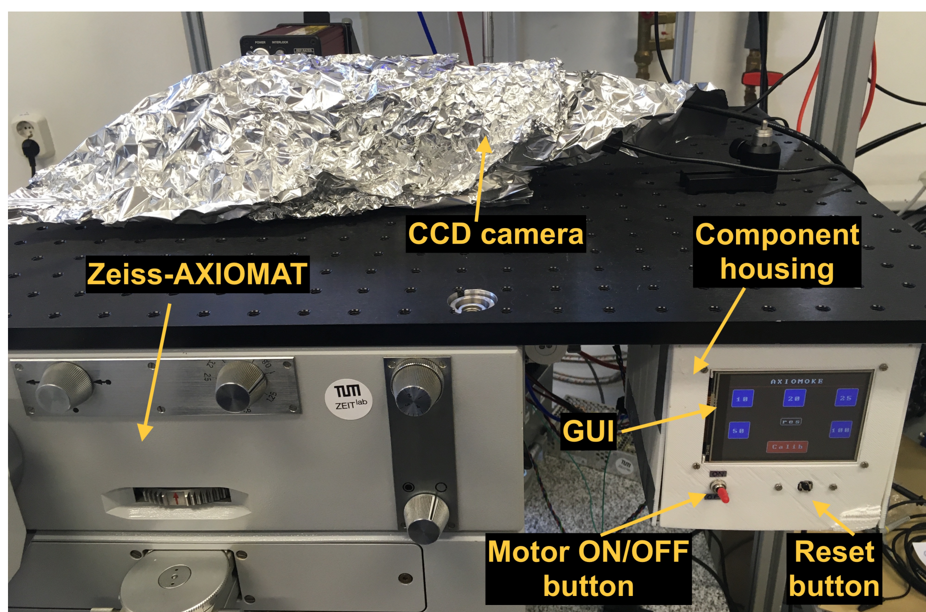

Figure A.8: Components housing seen from front side. Two external buttons are shown.

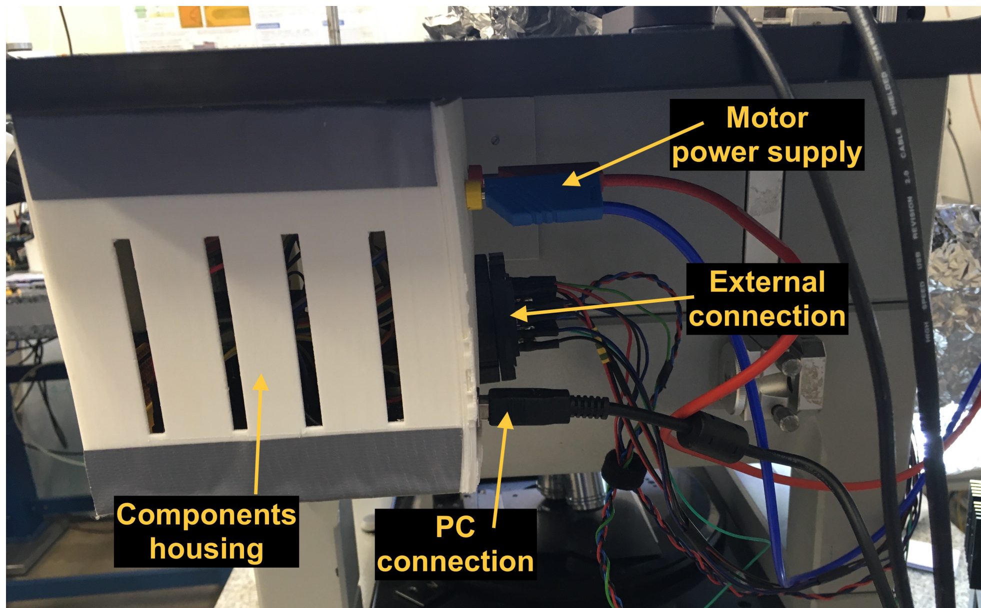

Figure A.9: Components housing seen from lateral side.

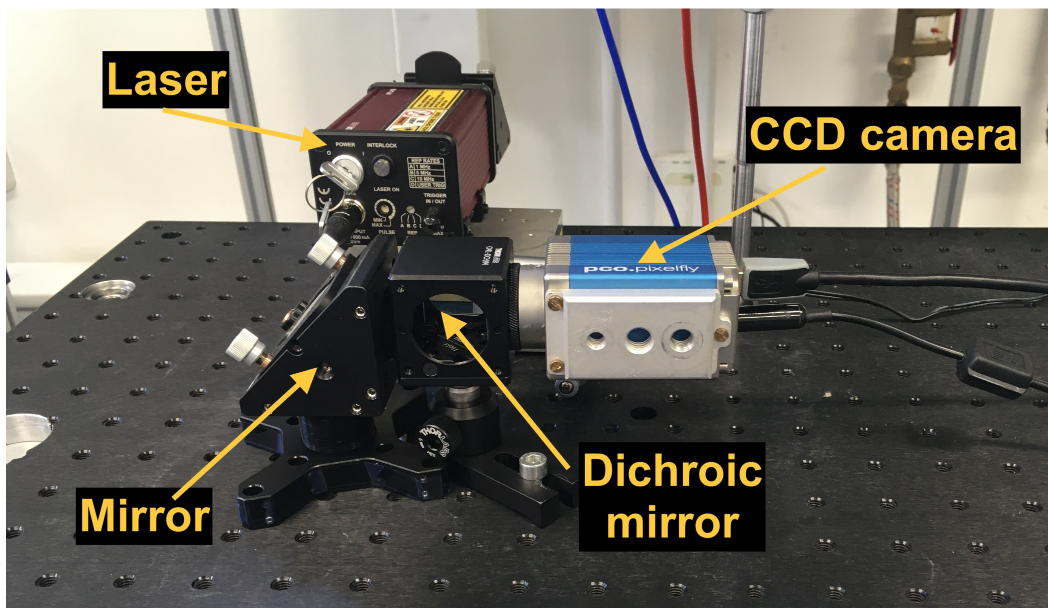

Figure A.10: CCD camera.

Bibliography

[1] W. Kuch. "Magnetic Imaging". In: *Magnetism: A Synchrotron Radiation Approach*. Ed. by E. Beaurepaire, H. Bulou, F. Scheurer, and J.-P. Kappler. Berlin, Heidelberg: Springer Berlin Heidelberg, 2006, pp. 275–320.

[2] A. Hubert and R. Schäfer. *Magnetic Domains: The Analysis of Magnetic Microstructures*. Springer, 1998. ISBN: 9783540641087. URL: https://books.google.de/books?id=pBE421LYs-MC.

[3] *Education in Microscopy and Digital Imaging*. URL: http://zeiss-campus.magnet.fsu.edu/articles/basics/reflected.html.

[4] *Microscopy Resource Center*. URL: https://www.olympus-lifescience.com/en/microscope-resource/primer/anatomy/reflected/.

[5] *Lens optics*. URL: https://www.britannica.com/technology/lens-optics.

[6] P. Mazzoldi, M. Nigro, and C. Voci. *Fisica*. Fisica. Edises, 1998. ISBN: 9788879591522. URL: https://books.google.de/books?id=PKs7AAAACAAJ.

[7] *Positive lens*. URL: https://en.wikipedia.org/wiki/Lens#/media/File:Lens1.svg.

[8] *Focal points of thin lenses*. URL: http://eyesvisions.com/image/uysrvin56p.jpg.

[9] *Introduction to Lenses and Geometrical Optics*. URL: https://www.olympus-lifescience.com/en/microscope-resource/primer/lightandcolor/lensesintro/.

[10] *Thin Lenses*. URL: https://phys.libretexts.org/Bookshelves/University_Physics/Book%3A_University_Physics_(OpenStax)/Map%3A_University_Physics_III_-_Optics_and_Modern_Physics_(OpenStax)/02%3A_Geometric_Optics_and_Image_Formation/2.05%3A_Thin_Lenses.

[11] D. A. Rowlands. *Physics of Digital Photography (Second Edition)*. 2053-2563. IOP Publishing, 2020. ISBN: 978-0-7503-2558-5. URL: http://dx.doi.org/10.1088/978-0-7503-2558-5.

[12] *Ray diagram for different positions of object*. URL: https://byjus.com/physics/to-find-image-distance-for-varying-object-distances-of-a-convex-lens-with-ray-diagrams/.

[13] *Oblique parallel rays*. URL: https://www.sarthaks.com/?qa=blob&qa_blobid=1266969969048832.

[14] *Longitudinal chromatic aberration*. URL: https://expertphotography.com/chromatic-aberration-photography/.

[15] *Köhler Illumination*. URL: https://www.olympus-lifescience.com/de/microscope-resource/primer/anatomy/kohler/.

[16] *The Rayleigh Criterion*. URL: https://www.zeiss.com/microscopy/int/solutions/reference/basic-microscopy/numerical-aperture-and-resolution.html.

[17] J. McCord. "Progress in magnetic domain observation by advanced magneto-optical microscopy". In: *Journal of Physics D: Applied Physics* 48.33 (July 2015), p. 333001. DOI: 10.1088/0022-3727/48/33/333001. URL: https://doi.org/10.1088%2F0022-3727%2F48%2F33%2F333001.

[18] *Numerical Aperture light cones*. URL: https://www.microscopyu.com/microscopy-basics/numerical-aperture.

[19] *Depth of Field Ranges*. URL: https://www.microscopyu.com/microscopy-basics/depth-of-field-and-depth-of-focus.

[20] *Depth of field and Depth of focus explanation*. URL: http://www.microscopist.co.uk/wp-content/uploads/2017/04/Depth-of-Field-and-depth-of-focus.pdf.

[21] *Microscope alignment for optimal image quality: Köhler Illumination*. URL: https://www.youtube.com/watch?v=ZRZ9_ov6Fak&list=PLE5ZmKUjv9OA-I7-b8aG8EmFGScUheh2j&index=25&t=1s.

[22] S. Breitkreutz-v. Gamm. "Perpendicular Nanomagnetic Logic: Digital Logic Circuits from Field-coupled Magnets". PhD thesis. Apr. 2015.

[23] C. Riva and G. Gentili. *Appunti di campi elettromagnetici*. Maggioli Editore, 2013. ISBN: 9788838762369. URL: https://books.google.de/books?id=lp8pnwEACAAJ.

[24] S. Breitkreutz. "Aufbau eines magneto-optischen Messplatzes zur Charakterisierung von Co/Pt-Mehrlagenschichten". MA thesis. Technische Universität München, 2009.

[25] J. D. Jackson. *Classical electrodynamics*. John Wiley & Sons, 2007.

[26] T. Haider. "A review of magneto-optic effects and its application". In: *Int. J. Electromagn. Appl* 7.1 (2017), pp. 17–24.

[27] M. Metz. "High Power LED Driver". 2004.

[28] *Model 1835-C Multi-Function Optical Meter*. URL: ftp://download.newport.com/Photonics/Power%20Meters/Obsolete%20Products/1835-c/1835-C%20Manual%20.pdf.

[29] *LeCroy WaveJet 324A Digital Oscilloscope*. URL: https://www.itm.com/pdfs/cache/www.itm.com/wavejet-324a/datasheet/wavejet-324a-datasheet.pdf.

[30] *Zeiss Axiomat Operating Instructions*. URL: https://archive.org/details/manual_Zeiss_Axiomat_User_Manual/mode/2up.

[31] *MATLAB for PCO*. URL: https://www.pco.de/software/third-party-software/matlab/.

[32] *ACL50832U - Aspheric Condenser Lens*. URL: https://www.thorlabs.com/thorproduct.cfm?partnumber=ACL50832U.

[33] *Diffuser DG05-120*. URL: https://www.thorlabs.com/thorproduct.cfm?partnumber=DG05-120.

[34] J. B. Bosse, N. S. Tanneti, I. B. Hogue, and L. W. Enquist. "Open LED Illuminator: A Simple and Inexpensive LED Illuminator for Fast Multicolor Particle Tracking in Neurons". In: *PLOS ONE* 10 (Nov. 2015). URL: https://doi.org/10.1371/journal.pone.0143547.

[35] *An illustration of the basic optical invariant*. URL: https://www.laserfocusworld.com/biooptics/bioimaging/fluorescence/article/14190718/solidstate-light-sourcesfluorescence-microscopy-hybrid-approach-lets-solidstate-sources-light-up-fluorescence.

[36] *pco.pixelfly - CCD camera*. URL: https://www.pco.de/fileadmin/user_upload/pco-product_sheets/pco.pixelfly_usb_data_sheet.pdf.

[37] *An Introduction to Scientific Imaging Charge-Coupled Devices*. URL: https://fiorini.faculty.polimi.it/Progettazione%20elettronica%20per%20strumentazione%20biomedica/SITe-CCD.pdf.

[38] *KCB1C - Right-Angle Kinematic Mirror Mount*. URL: https://www.thorlabs.com/thorproduct.cfm?partnumber=KCB1C#ad-image-0.

[39] *pco.camware User Manual*. URL: https://www.pco.de/fileadmin/fileadmin/user_upload/pco-manuals/pco.camware_manual.pdf.

[40] Z. Qiu and S. D. Bader. "Surface magneto-optic Kerr effect". In: *Review of Scientific Instruments* 71.3 (2000), pp. 1243–1255.

[41] M. stella. "Development of a Kerr microscope for the study of magnetic micro and nanostructures". MA thesis. Politecnico di Milano, 2016/2017.

[42] *Arduino MEGA 2560 Pinout Diagram*. URL: https://content.arduino.cc/assets/Pinout-Mega2560rev3_latest.pdf.

[43] *UTFT library*. URL: http://www.rinkydinkelectronics.com/library.php?id=51.

[44] *Display, Shield and Arduino connection*. URL: https://www.sainsmart.com/products/mega-2560-3-2-tft-tft-shield.

[45] *3.2inch-TFT-Display*. URL: https://aconfluence.no/display/SS/TFT+320QVT+9341+3.2+Inch+LCD+Display+Module?desktop=true¯oName=view-file.

[46] *TFT LCD MEGA Shield V2*. URL: https://www.komputer.de/zen/index.php?main_page=product_info&products_id=218.

[47] *URTouch library*. URL: http://www.rinkydinkelectronics.com/library.php?id=92.

[48] *TFT MEGA V2 Schematic*. URL: https://www.komputer.de/wordpress/wp-content/uploads/2014/03/TFT_MEGA_V2.0.pdf.

[49] *An Introduction to Low Voltage DC Motors*. URL: ftp://ftp.dei.polimi.it/outgoing/Massimo.Ghioni/Power%20Electronics%20/Motor%20control/DC/DC%20-%20motors.pdf.

[50] *Brushed DC Motor Fundamentals*. URL: ftp://ftp.dei.polimi.it/outgoing/Massimo.Ghioni/Power%20Electronics%20/Motor%20control/DC/DC%20motor%20basics.pdf.

[51] N. Mohan, T. M. Undeland, and W. P. Robbins. *Power Electronics. Converters, Applications and Design*. third. John Wiley and Sons, Inc, 2003.

[52] *POSITION CONTROL OF A DC MOTOR*. URL: ftp://ftp.dei.polimi.it/outgoing/Massimo.Ghioni/Power%20Electronics%20/Motor%20control/DC/DC%20Motor%20Fundamentals.pdf.

[53] *Stepper Motor Basics*. URL: ftp://ftp.dei.polimi.it/outgoing/Massimo.Ghioni/Power%20Electronics%20/Motor%20control/stepper/Stepper%20Motor%20Basics.pdf.

[54] *Stepping Motors Fundamentals*. URL: ftp://ftp.dei.polimi.it/outgoing/Massimo.Ghioni/Power%20Electronics%20/Motor%20control/stepper/Stepping%20%20motor%20basics.pdf.

[55] *DRV8825 Stepper Motor Driver Carrier*. URL: https://www.pololu.com/product/2133.

[56] *L293x Quadruple Half-H Drivers*. URL: https://www.ti.com/lit/ds/symlink/l293.pdf.

[57] *4 Phase ULN2003 Stepper Motor Driver PCB*. URL: https://www.electronicoscaldas.com/datasheet/ULN2003A-PCB.pdf.

[58] *28BYJ-48 – 5V Stepper Motor*. URL: http://robocraft.ru/files/datasheet/28BYJ-48.pdf.

[59] *AccelStepper library for Arduino*. URL: https://www.airspayce.com/mikem/arduino/AccelStepper/.

[60] *Microstepping - Faulhaber*. URL: https://www.faulhaber.com/fileadmin/user_upload_global/support/MC_Support/Motors/AppNotes/Faulhaber_AN015_EN.pdf.

[61] *NEMA 11-size hybrid bipolar stepping motor*. URL: https://www.pololu.com/product/1206.

[62] *28BYJ-48 Stepper Motor with ULN2003 Driver*. URL: https://www.makerguides.com/28byj-48-stepper-motor-arduino-tutorial/.

[63] *AccelStepper Class Reference*. URL: https://www.airspayce.com/mikem/arduino/AccelStepper/classAccelStepper.html.

[64] *SY28STH45-0674A - Hybrid Stepping Motor Specification*. URL: https://www.pololu.com/file/0J687/SY28STH45-0674A.pdf.

[65] *DRV8825 Stepper Motor Driver Carrier*. URL: https://www.pololu.com/product/2133.

[66] *DRV8825 Stepper Motor Controller IC.* URL: https://www.ti.com/lit/ds/symlink/drv8825.pdf?ts=1614792126870&ref_url=https%253A%252F%252Fwww.google.com%252F.

[67] *Stepper Motor Explained.* URL: https://www.e-jpc.com/stepper-motor-voltage-explained/.

[68] *DRV8825 Stepper Motor Driver Carrier Schematic.* URL: https://www.pololu.com/file/0J603/drv8824-drv8825-stepper-motor-driver-carrier-schematic-diagram.pdf.

[69] *Data sheet RLMD01-09.* URL: https://www.rls.si/eng/fileuploader/download/download/?d=1&file=custom%2Fupload%2FRLMD01_09EN_datasheet.pdf.

[70] *AbsoluteEncoders Context Technology SSI AppNote.* URL: https://www.posital.com/media/posital_media/documents/AbsoluteEncoders_Context_Technology_SSI_AppNote.pdf.

[71] *SPI - Single master to single slave.* URL: https://it.wikipedia.org/wiki/Serial_Peripheral_Interface#/media/File:SPI_single_slave.svg.

[72] *The Serial Peripheral Interface (SPI).* URL: http://avrbeginners.net/architecture/spi/spi.html.

[73] *SPI library.* URL: https://www.arduino.cc/en/reference/SPI.

[74] *HP 8112A Pulse generator.* URL: http://userequip.com/files/specs/1549/HP%208112A%20Operating%20&%20Programming%20Only.pdf.

[75] *µA741 General Purpose Operational Amplifiers.* URL: https://www.ti.com/lit/ds/symlink/ua741.pdf?ts=1613505505137&ref_url=https%253A%252F%252Fwww.ti.com%252Fproduct%252FUA741.

[76] *Optimizing Precision Photodiode Sensor Circuit Design.* URL: https://www.analog.com/en/technical-articles/optimizing-precision-photodiode-sensor-circuit-design.html#.

[77] F. Zappa. *Electronic Systems.* Società Editrice Esculapio, 2019. ISBN: 9788834175606. URL: https://books.google.de/books?id=vG6rDwAAQBAJ.

[78] *Silicon Photodiode BPW21R.* URL: https://www.vishay.com/docs/81519/bpw21r.pdf.

[79] *FreeCAD Basic modeling tutorial.* URL: https://wiki.freecadweb.org/Basic_modeling_tutorial.